

Microfluidic systems for in-flow bioanalytes collection

Présentée le 8 février 2022

Faculté des sciences et techniques de l'ingénieur
Chaire Swiss-up en ingénierie - Laboratoire d'électronique pour les sciences du vivant
Programme doctoral en microsystèmes et microélectronique

pour l'obtention du grade de Docteur ès Sciences

par

Pierre-Emmanuel Marie THIRIET

Acceptée sur proposition du jury

Prof. M. Gijs, président du jury
Prof. C. Guiducci, directrice de thèse
Prof. L. Flanagan, rapporteuse
Prof. S. Manalis, rapporteur
Prof. A. Radenovic, rapporteuse

Yesterday is history,
Tomorrow is a mystery,
And today is a gift,
That's why they call it present
— Master Oogway

To my family...

Acknowledgements

First I would like to express my deepest gratitude to my supervisor Professor Carlotta Guiducci for guiding me throughout my PhD journey. From the first day she has been extremely supportive and eager to share with me her deep comprehension of the microfluidics domain. She trusted my ideas and helped me explore many aspects of biology I was not familiar with. She is not only an excellent scientist but also an exceptional human being. I feel privileged that I had the chance to work with her and wish to all my fellow PhD student to work in the same environment that I was gifted with.

I would also like to thank all my jury members, Professor Martinus Gijs, Professor Lisa Flanagan, Professor Scott Manalis and Professor Aleksandra Radenovic. Despite their busy agendas they accepted to be part of my committee and to contribute to improving this manuscript with their outstanding expertise.

I would like to thank so much Prof. Polly Fordyce from Stanford University for hosting me in her lab for a really fruitful experience, those three months in California helped me gained a new perspective on biology and surface modifications. I am especially grateful to my collaborator Minsung Cho for taking the time to introduce me to the impressive science done in his lab.

I want to acknowledge the help of the center of microfabrication at EPFL (CMi) for their constant support and their precious advice regarding the development of new protocols.

I am very grateful to all the people who accepted to collaborate with us and share their expertise to carry out multidisciplinary project. I would especially like to thank Joern Pezoldt and Professor Bart Deplancke from the laboratory of Systems Biology and Genetics at EPFL for conducting mRNA sequencing protocols with us. I would like to acknowledge the precious support received by the Service de Pharmacologie Clinique at the Centre Hospitalier Universitaire Vaudois (CHUV) and in particular to Thierry Buclin, Christophe Buttica, Laurent Arthur Decosterd, and Dominique Werner. Their insight helped us understand the needs for point-of-care diagnostics platform for kidney injury detection. Finally I would like to thank Lauréanne Putallaz and Fabien Rebeaud for the valuable discussions and advice about the implementation of immunoassays on beads.

Acknowledgements

I am so thankful to all the CLSE lab members for making this period one of the best of my life. More than colleagues they are like a second family to me. First I want to thank the PhD student crew, Saurabh, my partner in crime since day 1, hiking summits of Jura, almost drowning in Hawaiï..., Gloria, a truly amazing person and scientist, who reconciliated me with Italian folks and taught me beach-volley, and Till, the greatest of all Swiss, whose kindness is only equaled by intelligence. We need to go play soccer once. I also would like to thank the Rea team, led by Erick and Loulia with their indefectible thrive to help pregnant women. They are also very supportive friends always there when you feel down. I would also like the rest of the Rea I was blessed to work with, Tommaso, Adélie and Siria. Finally I would like to thank Enrico, Lilia and Heather for their precious advice and making the lab a safe and comfortable to work..

I would like to thank all the students and interns I have been lucky to supervise during my PhD studies: Leonardo, Danashi, Samuele, Paul, Gabriele, Théa, Danashi, Tsandni, Cécile, Tommaso and Daniele . They all contributed in a way or the others to the results presented in this thesis and mentoring them was a truly fruitful experience.

Finally I would like to my family, especially my parents, Anne and Christian and siblings, Maud and Jean-Gabriel, who have been supporting and encouraging me since the beginning of my studies. They were always there in stressful and doubtful time and gave me the strength to convert the best of my potential. I would like to thank all my friends that helped me free my mind from scientific issues, Syméon, Jean-Baptiste, Baptiste, Hugo, David and Renaud. To conclude I am grateful to all the teachers that taught me everything I know until know, they were the one triggering my love for science and I owe them my successful studies.

Lausanne, December 23, 2021

Pierre-Emmanuel Thiriet

Preface

Diving in the drafting of this preface, I have been giving some thoughts about what it is with micro-technology engineers and biological matter; those scholars who grew in the comfort of the (most of the time) deterministic fate of processing solid state and synthetic chemical materials, like silicon, resins, metals, plastics, and decided to approach the sciences of life: a world of randomness, complexity impossible to size, unattainable efficiency, as terrifying as fascinating. I am one of them, and I have been for exactly 20 years today, when I graduated in microelectronics and started right away a PhD in what at the time was still a rather pioneering field. Since then, I have looked at myself, and dozens of those fools, from very close, and I would allow myself to say that we all oscillate between these two states: the strive for knowledge and understanding, and the obsession with control (or the lack of it), manipulation and definition of that matter and its elementary particles. The challenge to apply to biological matter what you have learned in the books and in the cleanroom and the many failures are upsetting, and you are brought to think that this is just not for you and your *forma mentis*, that it is *altro da te*, but you cannot but ironically realize that, instead, this matter is precisely you, you are made out of it and its domains of research impact in so many aspects your own life, of society, of health, and that it is absolutely worth the ache.

I shall mention that Pierre-Emmanuel is way less dark and conflicted than I am. Luckily for my balance, the essence and habit of my exchanges with him are sparkles of optimism, seamless capability to understand each other mind and the light of his sharp mind. He is one of those students that you will miss for a long time after he got his title for not showing up anymore at your office with the regularity that an advisor-student relationship mandated him. He is one of those fellows you seek to share ideas and solutions and you would try to talk into becoming your peer and your colleague.

Certainly thanks to his constitution, Pierre-Emmanuel did great, both in knowledge and in matters of control of the biological elements in the samples we have been working with.

We have long being fascinated by the idea to manipulate and move particles in a flow chamber by designing electrokinetic fields of force sufficiently strong to act on them singularly, deterministically and specifically. Moreover, we believed in the need to spare the particles and the biological elements from direct contact with the electrodes, to prevent damaging and artifacts.

Preface

Pierre-Emmanuel succeeded in combining a cell arraying device to display single biological cells in a bi-dimensional ordered fashion with a technique that selectively removes single ones of them from the array and deliver them to the outlet of the device. As the impact of manipulation is a primary concern, this study was supported by the analysis of the genetic expression of delivered cells in terms of their stress and overall differences with respect to reference populations, providing an important contribution to the assessment of the advantages and the limits of microfluidics designs.

He also applied his particle manipulation techniques to the field of in vitro molecular diagnostics and, in particular, immunoassays. He leveraged new control and micro-actuation functions in fluids to counteract mass transport phenomena which normally limit sensitivity and increase the binding time. He was able to define a system that could manage multiple markers analysis in a very short time, thanks to the possibility to specifically address particles with different properties. In the future, we hope to bring an evolution of his system to become a fully automated point-of-care that combines sensitivity to low concentrations and speed to response.

I am proud of Pierre for what he did of the opportunity of writing a thesis. We see less and less thesis manuscripts where the candidate takes a step back and provides an actual intellectual work based on his or her efforts and findings, reworking them, asking new questions and putting the research in perspective. I hope you will enjoy it as much as I did.

Lausanne, 25 October 2021

C. Guiducci.

Abstract

Microfluidic is an ensemble of technologies and methods that permits the handling and analysis of minute volumes of samples in short timescales. Since its introduction it revealed a remarkable potential to unveil novel biological mechanisms. The small volumes involved in microchannels shortens reaction time and foster interactions between bioanalytes. Furthermore, the reduced footprint of the microfluidic channels also allows the integration of different modules within the same chip, each performing a dedicated step of a complex procedure, in what was defined as a lab-on-a-chip (LOC) platform. The use of 3D dimensional particles in such devices serve a double purpose: the manipulation of biological sample such as single cells in suspension and the introduction of microbeads that exhibits high surface-to-volume ratios and hence improved analyte collection.

In this thesis, we present the development of new tools for the accurate manipulation of microparticles in microfluidic channels and their efficient exposure to flow. Microbeads or single cells were immobilized on-chip via a combination of hydrodynamic and dielectrophoretic (DEP) effects. Following their trapping, single-cells could be selectively released and recovered off-chip for further expansion and characterization. A transcriptomic analysis of recovered cells revealed marginal alteration of their molecular profile upon exposure to DEP forces and thus validated the potential of our technology for the assessment of single-lymphocytes properties. The efficient analyte collection achieved by microfluidic systems could benefit the field of diagnostics through the introduction of two distinct platforms. The first employs DEP forces to carry out the simultaneous detection of two acute kidney injury markers, NGAL and Cystatin C, in a minimally diluted buffer. High aspect-ratio three-dimensional electrodes were integrated in a microfluidic channel and could generate sufficient forces to retain functionalized beads against the flow of reagents for a 15 minutes-long incubation. The second introduces a novel approach based on DNA barcodes and toe-hold mediated strand displacement to perform the rapid readout of highly multiplexed immunoassays. The signal acquisition takes place in a wide microchamber crowded with mechanical traps stopping the beads at dedicated locations, its duration could be shorten down to 3 minutes per marker, with a throughput approaching 20 markers per hour.

The obtained results demonstrated the potency of microfluidic platform for the manipulation and analysis of microparticles in-flow and paves the way for the development of a novel

Abstract

generation of highly integrated lab-on-a-chip systems.

Keywords: Microfluidics, 3-D electrodes, Dielectrophoresis (DEP), Hydrodynamic trapping, On-chip incubation, Immunoassays, Kidney injury, DNA barcode, Toehold-mediated strand displacement, Single-cell manipulation, mRNA sequencing.

Résumé

L'emploi de canaux microfluidiques permet la manipulation et l'analyse d'échantillons aux volumes réduits dans une échelle de temps très courte. Depuis leur introduction, ces canaux ont démontré un potentiel prometteur pour la mise en évidence de nouveaux mécanismes biologiques. L'utilisation de faibles volumes d'échantillons favorise les interactions entre analytes et en conséquence diminue la durée des réactions biochimiques. De plus, la petite taille des systèmes microfluidiques permet l'intégration de plusieurs modules spécifiquement conçu pour réaliser une tâche dédiée au sein d'une même puce microfluidique. Un tel système est communément appelé un laboratoire sur puce (lab-on-a-chip en anglais). L'introduction de particules tridimensionnelles au sein de ces plateformes se révèle pertinente dans deux contextes différents : la manipulation d'échantillons biologiques comme des cellules en suspension dans un canal ou le diagnostic clinique de pathologies à l'aide de microbilles fonctionnalisées qui garantissent une collection efficace d'espèces à leur surface.

Dans le cadre de cette thèse nous discutons le développement de nouveaux outils conçu pour assurer une manipulation précise de microparticules dans un canal microfluidique ainsi que leur exposition optimale à un écoulement laminaire. L'immobilisation de cellules ou de microbilles est réalisé dans la puce microfluidique à l'aide de restrictions mécaniques ou de forces diélectrophorétiques. A la suite de son immobilisation une seule cellule peut être choisie et récupérée hors de la puce microfluidique pour des analyses plus approfondies. Une analyse transcriptomique des cellules récupérées hors de la puce révèle un impact mineur causé par l'application de forces diélectrophorétiques, ce qui confirme la pertinence de notre approche pour l'analyse des propriétés des cellules immunitaires. L'introduction de deux plateformes basées sur la capacité des systèmes microfluidiques à promouvoir les interactions entre analytes nous a amené à la mise au point de nouvelles méthodes de diagnostic. La première plateforme repose sur l'utilisation de forces diélectrophorétiques pour réaliser la détection simultanée de deux marqueurs, appelés NGAL et Cystatin C, associés à une insuffisance rénale aiguë. L'intégration d'électrodes tridimensionnelles au sein des structures microfluidiques assure la création de champs électriques suffisants pour immobiliser des billes contre l'écoulement laminaire et autorise l'incubation de réactifs pour une durée de 15 minutes. Le second système propose une nouvelle stratégie basée sur l'utilisation de brins d'ADN en tant que code-barre pour effectuer la lecture rapide d'un immunoessai réalisé au préalable. L'acquisition du signal se fait dans un large canal microfluidique qui comporte des

Résumé

structures dédiées à l'immobilisation des microbilles. Chaque mesure est effectuée en moins de trois minutes, ce qui permet l'analyse d'environ 20 marqueurs par heure, une cadence très importante dans le domaine du diagnostique.

Les résultats obtenus dans le cadre de ce travail de doctorat valident le potentiel des systèmes microfluidiques pour la manipulation et l'analyse de microparticules au sein d'écoulements laminaires et ouvrent la voie au développement de nouveaux laboratoires sur puce hautement intégrés.

Mots-clés : Microfluidique, Electrodes tridimensionnelle, Piège hydrodynamique, Incubation sur puce, Immunoessai, Insuffisance rénale, barcoding moléculaire, Manipulation de cellules isolées, Séquençage d'ARN messager.

Contents

Acknowledgements	i
Preface	iii
Abstract (English/Français)	v
List of Figures	xiii
List of Tables	xvii
List of Equations	xix
Introduction and theoretical considerations on mass-transport	1
1 Capturing a molecule	3
2 Collection of molecules on the sensor	6
2.1 Diffusion-based transport	6
2.2 Introduction of convection in the channel	7
3 Uniting mass-transport and binding kinetics	10
4 Objectives and thesis outlook	11
1 Fabrication methods for particle manipulation in microfluidics	13
1.1 Prototyping of microfluidic devices	13
1.1.1 Fabrication of SU-8-based micro-channels	14
1.1.2 Fabrication of PDMS-based micro-channels	15
1.2 Integration of 3-D electrodes in a microfluidic channel	18
1.2.1 Microfabrication process flow for 3-D electrodes integration in a microfluidic channel	19
1.2.2 Characterization of electrodes	21
1.3 Hybrid SU-8/PDMS valves for hard photoresist-based microfluidics	24
1.4 Summary and conclusion	26
2 Microparticle handling and reversible trapping in microfluidic channels	27
2.1 Dielectrophoresis, a powerful tool for particles manipulation	28
2.2 Hydrodynamic trapping of particles and strategies for their selective release	29
2.2.1 Hydrodynamic trapping	29
2.2.2 Single-cell immobilization and selective release	31

Contents

2.2.3	Trapping and release of beads	37
2.3	DEP-based manipulation of beads	39
2.3.1	Holding beads against the flow via DEP forces	39
2.3.2	Device layout	41
2.3.3	Trapping results	41
2.3.4	Surfing results	43
2.4	Summary and conclusion	43
3	Multimarker diagnostic approaches based on microbeads	45
3.1	Point-of-care system or Acute Kidney Injury detection	46
3.1.1	Context	46
3.1.2	System layout and operation principle	50
3.1.3	Real time monitoring of on-chip incubation	52
3.1.4	On-chip incubation vs Off-chip incubation	54
3.1.5	Multiple biomarker detection	58
3.2	Oligo-based platform for fast screening of multiple biomarkers	65
3.2.1	General concepts and state-of-the-art	65
3.2.2	System layout and operating principle	68
3.2.3	On-chip coupling of DNA probes with DNA-decorated beads	69
3.2.4	Study of fluorescent signal bleaching	70
3.2.5	Toe-hold-based approach	72
3.3	Summary and conclusion	76
4	Assessment of the phenotypic impact of microfluidics and DEP effects on single-cells	77
4.1	Single cell sequencing	78
4.2	Experimental design and methodology	80
4.2.1	Experimental design	80
4.2.2	Sequencing methodology	80
4.3	Viability assessment	82
4.4	Transcriptional profiling of cells injected in our microfluidic platform	83
4.5	Summary and conclusion	85
5	Perspectives	87
5.1	DEP-based manipulation of beads	87
5.1.1	Towards a Point-Of-Care platform	87
5.1.2	Low-volume sample detection	89
5.1.3	Generation of microparticles' streams	89
5.2	Oligo-based platform for multiple markers screening	90
5.2.1	Highly multiplexed detection of markers	90
5.2.2	A new approach employing aptamers	91
5.3	Single cell handling platform	91
5.3.1	Reducing the footprint of a trapping unit to increase throughput	91
5.3.2	Exposure to active components for in-situ single-cell analysis	92

Conclusion	93
Bibliography	95
Curriculum Vitae	111

List of Figures

Figure 1	Schemes of the planar and spherical sensors employed for analyte collection analysis	2
Figure 2	Plot of the G ratio as a function of the microparticle radius	5
Figure 3	Scheme of the trajectory of a particle in a microfluidic channel with a height H	8
Figure 1.1	Process flow of the fabrication of SU-8 microfluidic channels	14
Figure 1.2	SEM pictures of SU-8 microfluidic channels	15
Figure 1.3	Process flow of the fabrication of PDMS microfluidic channels with Si molds	16
Figure 1.4	SEM images of PDMS structures fabricated with Si molds	16
Figure 1.5	Process flow of the fabrication of PDMS microfluidic channels with SU-8 molds	17
Figure 1.6	SEM images of PDMS structure fabricated with SU-8 molds	18
Figure 1.7	Process flow of the fabrication of standing electrodes embedded in a microfluidic channel	20
Figure 1.8	Images of 3D electrodes embedded inside a microfluidic channel	21
Figure 1.9	Experimental plot of the impedance module of a liquid/electrode interface	22
Figure 1.10	Layout of the impedance test structures	23
Figure 1.11	Plot of the characterization of the impedance test structures	23
Figure 1.12	Fabrication of PDMS valves on top of SU-8 channels	25
Figure 1.13	Operation of the hybrid SU-8/PDMS valves	26
Figure 2.1	Theoretical principle of dielectrophoresis	29
Figure 2.2	Hydrodynamic trapping basic principle	30
Figure 2.3	Cell trapping and release device layout	32
Figure 2.4	SEM image of a trapping and release unit	32
Figure 2.5	Simulation of the fluid velocity and electric field in a trapping region . .	33
Figure 2.6	Trapping of a lymphocyte in a microfluidic trap	34
Figure 2.7	Release of a lymphocyte from a microfluidic trap	35
Figure 2.8	Selective release of a lymphocyte from a microfluidic trap	35
Figure 2.9	Operation of hybrid PDMS/SU-8 valves for cell handling and off-chip recovery	36
Figure 2.10	PDMS trap to capture and maintain large beads in a fluidic channel . .	38
Figure 2.11	Hydrodynamic trapping and release of beads in a PDMS chamber . . .	38

List of Figures

Figure 2.12	Effects of drag and DEP forces on a bead placed in a microfluidic channel	39
Figure 2.13	DEP as a tool for on-chip incubation and accumulation of beads	40
Figure 2.14	DEP discrimination of different-sized beads	41
Figure 2.15	Layout of the platform for beads incubation and clustering	42
Figure 2.16	Results of the DEP-based on-chip capture of beads	42
Figure 2.17	DEP surfing of beads and accumulation against the channel sidewall .	43
Figure 3.1	Typical calibration curve of a biosensor	46
Figure 3.2	Illustration of two different formats of immunoassays	47
Figure 3.3	Presentation of the successive steps performed on-chip to operate the platform	51
Figure 3.4	On-chip incubation of Neutrophil Gelatinase-Associated Lipocalin (NGAL) biomarker	53
Figure 3.5	Assessment of the on-chip incubation and beads clustering performance	55
Figure 3.6	Images of beads clustered in the accumulation area	55
Figure 3.7	Calibration curves for on-chip incubation and clustering performance assessment	56
Figure 3.8	NGAL detection performance comparison between our immunoassay on chip and a commercial ELISA kit	57
Figure 3.9	Spectral overlap of CY3 and CY5 signals from 6 μm NGAL and 2 μm Cystatin C-decorated beads	58
Figure 3.10	Cystatin C dose response curve	59
Figure 3.11	Simultaneous detection of NGAL and Cystatin C for acute kidney injury (AKI) diagnosis	60
Figure 3.12	Cross-contamination analysis in the multianalyte experiment	61
Figure 3.13	Layout of the platform for beads injection and incubation in two separate channels	62
Figure 3.14	Simultaneous detection of NGAL and Cystatin C with a two channels device	63
Figure 3.15	Cross-contamination analysis in a multianalyte assay with two channels.	64
Figure 3.16	On-beads analyte detection thanks to DNA barcoding	65
Figure 3.17	Use of heat as a possible solution for DNA double strands denaturation in the microfluidic channel	67
Figure 3.18	Use of photo-bleaching as a possible solution for fluorescence reduction in the microfluidic channel	67
Figure 3.19	Toehold-mediated isothermal strand displacement as a possible solution for fluorescence reduction in the microfluidic channel.	68
Figure 3.20	Layout of the platform for on-chip incubation of beads	69
Figure 3.21	Study of the on-chip hybridization of two complementary DNA strands	70
Figure 3.22	Monitoring of the photo-bleaching of Alexa Fluor 546 and Alexa Fluor 647 fluorophores.	71
Figure 3.23	Experimental validation procedure of the toehold approach	72
Figure 3.24	Off-chip performance of the toehold signal reduction.	73

Figure 3.25	On-chip sequential injection of detection and cleaning DNA sequences.	74
Figure 3.26	On-chip and off-chip characterization of the full assay using single stranded DNA conjugated to antibodies for the detection of Cystatin C	75
Figure 4.1	Schematic description of the Drop-seq methodology	79
Figure 4.2	Experimental plan implemented to assess the impact of our microfluidic system on cell phenotype	81
Figure 4.3	Viability study of the lymphocytes exposed to the DEP-based microfluidic system	83
Figure 4.4	Transcriptional profiling of cells injected in the microfluidic device . .	84
Figure 4.5	Investigation of gene expression upon application of DEP forces	84
Figure 5.1	New layout for capillary pumping in our AKI detection platform	88
Figure 5.2	Microbeads dried in a trehalose solution	88
Figure 5.3	Dose response curve for the off-chip detection of Galectin-3	90
Figure 5.4	New layout for simultaneous trapping and selective release of multiple cells	92

List of Tables

3.1	DNA sequences designed for the experiment described in Figure 3.21.	69
3.2	DNA sequences designed for the off-chip photo-bleaching study	71
3.3	DNA sequences designed for the investigation of the toehold approach	72
3.4	DNA sequences designed for the conjugation of antibodies	75
4.1	Primers used for reverse transcription and library preparation	82

List of Equations

1	Langmuir equation	3
2	Solution of the Langmuir equation	3
3	Probe density at equilibrium	3
4	Time constant for a Langmuir kinetic	4
5	Number of binding sites planar surface	4
6	Number of binding sites spherical surface	4
7	Number of beads in solution	4
8	G figure of merit spherical vs planar sensor	4
9	First Fick's law	6
10	Depletion region extend for a purely diffusive scenario	6
11	Surface collection rate in a pure diffusive scenario	6
12	Concentration of analyte at a distance r from the center of a sphere	7
13	Surfacic collection rate at a distance r from the center of a sphere	7
14	Collection rate at the surface of the microbead	7
15	Definition of the Peclet number of the channel	8
16	Fluid velocity at a distance z from the channel's bottom	8
17	Balancing convective and diffusive flux of the sensor	9
18	Depletion region size in the presence of convective and diffusive flux	9
19	Definition of the Peclet number associated with the sensor	9
20	Surfacic flux in the presence of convective and diffusive flux	9
21	General expression for the surfacic flow for high P_{eH}	10
22	Initial reactive flux	10
23	Balancing reactive and mass-transport flux	10
24	Definition of the Damkohler number	10
1.1	Impedance of a RC circuit	22
1.2	Equation of the double layer capacitance	22
2.1	Clausius-Mossotti factor equation	28
2.2	DEP force on a spherical particle placed in a electrical field gradient	28
2.3	Fluidic resistance ratio for efficient hydrodynamic trapping	31
2.4	Flow rate ratio for efficient hydrodynamic trapping	31
2.5	Drag force on a spherical particle	39

Introduction and theoretical considerations on mass-transport

Specific molecular interactions are without a doubt a cornerstone of biology. They are observed in all living organisms and involved in almost every biological pathway. Among many others, one could mention the immune system that relies on antibodies to specifically targets pathogens molecules [1], or neural networks that involve binding of receptors such as dopamine to regulate their activity [2]. In-vitro technologies also heavily rely on such interactions for various applications. For instance, some DNA sequencing approaches employ labelled oligonucleotides to bind their complementary strand and emit a fluorescent signal [3]. The diagnostics field largely benefited from the specific interaction between antibodies and antigens in immunoassays. The introduction of labels attached to antibodies grants a simple and efficient detection of proteins in physiological buffers. The most successful example of the tremendous potential of immunoassays is the development of Enzyme-Linked Immunosorbent Assay (ELISA), introduced by Engvall and Perlmann in 1971 [4], that revolutionized the biomarker detection with unprecedented sensitivity and reliability. Nonetheless, it necessitates significant fluid volumes and long waiting times for the binding to occur [5], hindering the analysis of rare samples. Furthermore, in-vitro techniques are often based on steady incubation and fail to mimic the complex and dynamic environment encountered within biological tissues.

The injection of low sample volumes in microfluidic channels can counteract both aforementioned limitations, as it requires low volumes of analyte and can reproduce capillary conditions frequently encountered in living organisms. Additionally, the reduction of the reaction volume leads to a decrease in the reaction time and allows for the implementation of high throughput parallel analysis. The miniaturization of the sensing sites also reduces the sensor footprint and permits its integration in compact devices such as Point-of-Care platforms (PoC). Microfluidic-based PoC devices aim at providing user-friendly and sensitive diagnostics within a short duration and at low cost, a valuable asset in the context of personalized medicine that will certainly play a significant role in the near future.

The collection of analytes at a sensor's surface is governed by complex equations that can not be easily solved in a general configuration. The solution of Navier-Stokes' equation in microfluidic channels has been implemented in the case of simplified microfluidic channels [6]. However, such resolution comes at a very computing-intensive price that is not compatible with the development of complex microfluidic structures.

In this introduction, we will discuss the theoretical background that describes the collection of analytes on different kinds of surfaces: a planar sensor or a population of spherical microbeads suspended in a microfluidic channel. The wide variety in the shapes and dimensions of microfluidic channel hinders a simple comparison of different devices. However, a good understanding of the dominant behaviors could be achieved with the introduction of dimensionless numbers, powerful tools frequently employed in the field of fluid mechanics [7]. They can effectively compare the relative influence of various physical phenomena [8] and help us understand which parameters will play a significant in the analyte collection.

Figure 1 presents the simplified models we use throughout the entire introduction to characterize the analyte collection on a planar or spherical sensor placed in a microfluidic channel. A planar sensor of length L_s and width W_s or spherical sensors with a radius R are placed in a microfluidic channel with a cross-section HW_C in which a flow Q is injected. It is the simplest model that still includes all the elements pertinent in our study, namely binding-reaction, diffusion and convection.

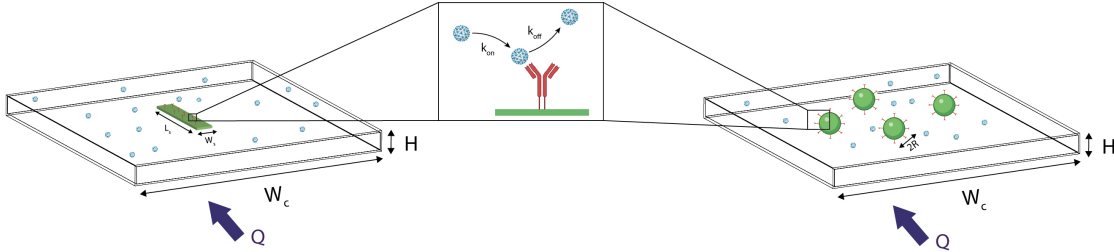


Figure 1: Schemes of the planar and spherical sensors employed for analyte collection analysis A planar sensor with a width W_s and a length L_s is placed at the bottom of a microfluidic channel with a cross-section HW_C in which a flow Q is injected (right part). Spherical sensors with a radius R are maintained in suspension in a similar micro-channel. In both cases, the binding interaction between the probe and the analyte is characterized by the association and dissociation constants k_{on} and k_{off} , respectively. Adapted from [7]

1 Capturing a molecule

The binding of the molecules to the sensing surface ultimately generates an output signal. Assuming first-order Langmuir kinetics, the surface density of probes occupied at the sensor surface $\Gamma(t)$ follows the equation:

$$\frac{\partial \Gamma}{\partial t} = k_{on}c_s(\Gamma_0 - \Gamma) - k_{off}\Gamma \quad (1)$$

Where Γ_0 is the surface density of probes at the sensor's surface, c_s the concentration of target analyte near the sensor and k_{on} and k_{off} the association and dissociation rates of the target on the probe, respectively. The probability that a binding event occurs depends on the number of binding sites available ($\Gamma_0 - \Gamma$). If the analyte is always provided in large amounts close to the sensor, then $c_s = c_0$ where c_0 is the bulk concentration of analyte, and one can solve the equation 1 to derive the association transient regime.

$$\Gamma(t) = \Gamma_0 \frac{c_0}{K_D + c_0} (1 - e^{-(k_{on}c_0 + k_{off})t}) \quad (2)$$

Where $K_D = k_{on}/k_{off}$ is the equilibrium dissociation constant that measures the propensity of the analyte to detach reversibly from the probe. This system will tend towards equilibrium for which the occupied probe density can be expressed as:

$$\Gamma_{eq} = \Gamma_0 \frac{c_R}{1 + c_R} \quad (3)$$

Where $c_R = c_0/K_D$ compares the concentration of the target analyte with the dissociation constant of the binding reaction. $c_R \gg 1$ will result in $\Gamma_{eq} = \Gamma_0$, i.e. a saturation coverage of the sensor's surface with target molecules, while $c_R \ll 1$ will lead to $\Gamma_{eq} = 0$, i.e. almost no analyte attached to the sensor. Indeed, a binding event will be more likely followed by a dissociation event rather than another binding event. It is interesting to notice that for low concentrations, the number of molecules bound at the surface of the sensor does not depend on the flow of analytes above the sensor but only on the dissociation constant of the probe. The intuitive idea to increase the flow rate in the channel will thus prove itself irrelevant.

Another interesting quantity that can be derived from equation 2 is the time needed to achieve steady-state, that can be written as:

$$\tau = \frac{1}{k_{off} + k_{on}c_0} = \frac{1}{k_{off}(1 + c_R)} \quad (4)$$

Concentrated solutions ($c_R \gg 1$) require all the binding sites to be occupied with reaching equilibrium. The equilibration time thus depends on how long it will take to bind all those molecules. On the other hand, diluted solutions ($c_R \ll 1$) do not need many binding events, so that time to reach equilibrium is determined by the time it takes for the on- and off- fluxes to compensate.

The number of probes at the surface of the sensor is an important figure of merit for analyte detection. It contributes to the dynamic range of the sensor and its performance at low concentrations. In the case of a planar surface, the number of binding site is given by:

$$N_{bindingsites,planar} = \Gamma_0 L_S W_S \quad (5)$$

With L_S and W_S the length and the width of the sensor, respectively.

Assuming that the surface density Γ_0 is constant, a group of N_{beads} with a radius R will provide instead:

$$N_{bindingsites,beads} = \Gamma_0 4\pi R^2 N_{beads} \quad (6)$$

binding sites. The number of beads in a volume V of solution can be expressed as in the following, where c_m is the massic concentration of beads in solution, defined as the mass of beads per unit of volume of solution and ρ_{bead} the density of the bead's material:

$$N_{beads} = \frac{m_{beads}}{m_{1bead}} = \frac{c_m V}{\frac{4}{3}\pi R^3 \rho_{bead}} \quad (7)$$

In order to compare the relative amount of available binding sites in a planar or spherical sensor, we introduce the figure of merit G . It is defined as the number of sites available on spherical particles in suspension above a planar sensor divided by the number of binding sites available on this planar sensor. It can therefore be expressed as:

$$G = \frac{\Gamma_0 4\pi R^2 N_{beads}}{\Gamma_0 L_S W_S} = \frac{3c_m H}{R\rho_{bead}} \quad (8)$$

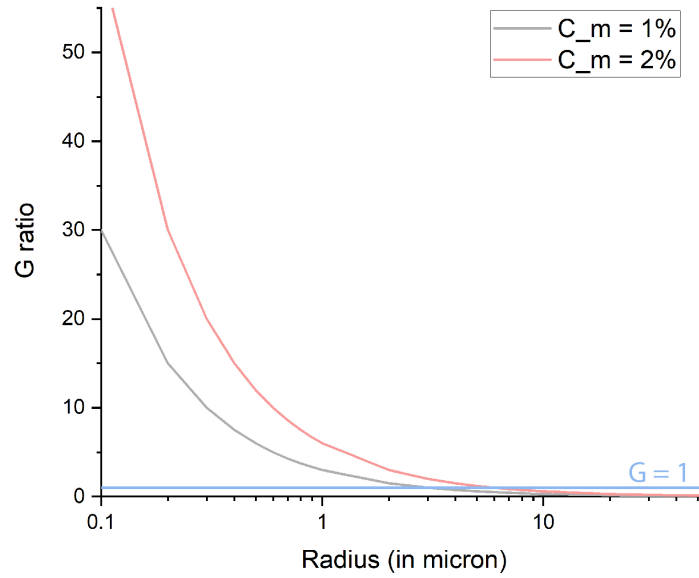


Figure 2: **Plot of the G ratio as function of the microparticle radius** The evolution of the G ratio is plotted for 2 values of c_m , 1% and 2%. The threshold to determine whether spherical or planar sensors provide more binding sites, i.e. $G=1$, is plotted in blue.

Interestingly, this ratio is independent of the size of the planar sensor and only depends on the spherical particles radius and their massic concentration. $G \gg 1$ results in more binding sites with spherical particles rather than with the planar sensor. Figure 2 depicts the evolution of G as a function of R with a channel height fixed at $100 \mu\text{m}$ and two representative values of c_m , 1% and 2%.

Beads of large diameters will provide less binding site per unit of volume compared to smaller beads. Indeed, beads with a radius below $1 \mu\text{m}$ can provide as much as 50 times more binding sites than a planar sensor of the same surface area. Furthermore, an increase in massic concentration c_m will naturally lead to an increase in the amount of beads and, therefore, their binding sites. It will also result in an augmentation of the radius R_{eq} corresponding to an equivalent binding sites number for both planar and spherical sensor (i.e. $G=1$), from 3 to $6 \mu\text{m}$ in the figure. Interestingly, the G ratio will also grow linearly with the height of the channel, demonstrating the importance of high channels when working with spherical particles in suspension. We can then conclude that microbeads can provide more binding sites and grant a better dynamic range to associated sensors due to their high surface to- to-volume ratio. They also offer better performance in terms of mass transport, a phenomenon that will be explored in detail in the next section.

2 Collection of molecules on the sensor

2.1 Diffusion-based transport

As analytes are captured by probes placed at the surface of a sensor, the concentration of these analytes at the vicinity of the sensor decreases locally and causes the appearance of a concentration gradient in the solution. According to the second law of thermodynamics, the system will naturally tend to minimize its entropy and a net flux of molecules from high concentration regions towards low concentration regions will appear. This phenomenon is called diffusion, and the flux of molecules per unit surface j_D is given by the first Fick's law:

$$j_D = -D\nabla c \quad (9)$$

where D is the diffusion coefficient and ∇c the concentration gradient in solution. As molecules located close to the sensor's surface are being consumed, a so-called depletion region develops above and around the sensor surface. The path of molecules is directed by random motion so that the time required by a molecule to travel a certain distance does not scale linearly with distance. Consequently, the size of the depletion region δ increases with the square root of time:

$$\delta \sim \sqrt{Dt} \quad (10)$$

Considering a planar sensor placed at the bottom of the channel, the depletion region will first grow radially for a time scale $\tau_{diff,H} = H^2/D$ until it reaches the top of the channel, then grows indefinitely inside the channel. It is interesting to note that, in such a system, the steady-state is never achieved. The surfacic collection rate in the pure diffusive case can be expressed as:

$$j_D = \frac{-D(c_0 - c_S)}{\delta} = -(c_0 - c_S)\sqrt{\frac{D}{t}} \quad (11)$$

The flux will endlessly decrease, and so will the analyte collection in the absence of flow. A spherical collection surface, however, exhibits different properties as they can reach a steady-state regime in similar conditions [9]. In a spherical geometry, the concentration of analyte at a distance r from the center of the sphere can be written as: [9]

$$c(r) = c_0\left(1 - \frac{R}{r}\right) \quad (12)$$

Where R is the radius of the bead. The diffusion flux per surface unit can be derived from equation 9:

$$j_D(r) = \frac{\partial c}{\partial r} = -Dc_0 \frac{R}{r^2} \quad (13)$$

Integrating this surfacic flux at the surface of the bead, one can obtain the flux of molecules on the bead surface:

$$J_D(R) = j_D(R)4\pi R^2 = -4\pi DRc_0 \quad (14)$$

While we would intuitively expect this flux to scale with the area of the bead, it only scales with its radius R . Indeed, as the radius R increases, the area increases as R^2 , but the concentration gradient decreases as $1/R$. This result can be generalized in the case of adsorbing objects of any shape placed in a channel with infinite height and width [9]. For a channel with a limited height such as the one previously described, the depletion region will grow spherically until it reaches the top of the channel and then horizontally. However, during this last step, the cross-section of the channel is fixed and can not increase, preventing the establishment of a steady-state regime as observed with spherical particles, where the size of the depletion region increases until the flux of molecules crossing the boundary of the depletion region compensates for the molecules captured at the bead's surface.

2.2 Introduction of convection in the channel

The introduction of convective transport can stop the infinite growth of the depletion region observed for a planar sensor placed in a channel with finite height. An equilibrium will be achieved for a depletion region δ_s for which the flux delivered by convection will compensate the diffusive flux through the upstream depletion zone. If at a given instant the depletion region in the channel is $\delta(t) < \delta_s$ the diffusive flux is too high and can not be balanced by convective flux resulting in a spreading of the depletion region. If $\delta(t) > \delta_s$, the diffusive flux can not consume all the molecules brought by convection, and the depletion region will shrink. In order to understand the relative importance of diffusion vs. convection in a microfluidic channel, one can compare the time a molecule needs to travel the height H of the channel by diffusion and the time it will take to travel the same distance due to convection, as illustrated in figure 3.

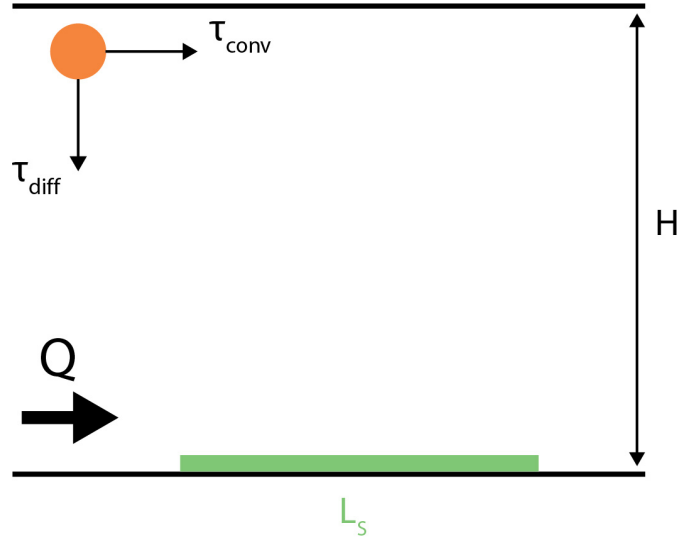


Figure 3: **Scheme of the trajectory of a particle in a microfluidic channel with a height H** A particle placed in a microfluidic channel will need a time τ_{diff} to diffuse over the distance H . The time it will need to travel the same distance H through convection is given by τ_{conv} .

The ratio of the aforementioned duration defines a dimensionless figure of merit referred to as the Peclet number of the channel (P_{eH}) [7, 10] :

$$P_{eH} = \frac{\tau_{diffusion}}{\tau_{convection}} = \frac{\frac{H^2}{D}}{\frac{H^2 W_c}{Q}} = \frac{Q}{D W_c} \quad (15)$$

Where Q is the volumetric flow rate of particles injected in the microfluidic channel and W_c the width of the channel. P_{eH} is also called the first Peclet number; it brings insights about the sensor's range of influence. If $P_{eH} \ll 1$ diffusion wins over convection, consequently, the depletion region extends over the entire height of the channel and all target molecules are collected by the sensor. If $P_{eH} \gg 1$ convection dominates in the channel, molecules are swept downstream before they can hit the sensor. This results in the loss of most of the analyte. The molecules that will effectively reach the sensor are located very close to the sensor, a region where the fluid velocity $v(z)$ can be derived from the Poiseuille flow and simplified to the following formula:

$$v(z) = \frac{6Q}{W_c H^2} z \quad (16)$$

Where z is the height above the sensor at which the fluid velocity is calculated. The thickness of the depletion region δ_s in the case of high P_{eH} can be derived in a similar way as equation

15. The time τ_{conv} it takes for a molecule to travel past the sensor can be equaled to the time τ_{diff} needed for a molecule to diffuse across the distance δ_s . we can thus deduce[7]:

$$\tau_{conv} \sim \tau_{diff} \Rightarrow \frac{\delta_s^2}{D} \sim \frac{L_s W_c H^2}{6Q\delta_s} \quad (17)$$

Isolating δ_s we find:

$$\frac{\delta_s}{l_s} \sim \left(\frac{DH^2 W_c}{QL_s^2} \right)^{\frac{1}{3}} \sim \left(\frac{1}{P_{eS}} \right)^{\frac{1}{3}} \quad (18)$$

Where

$$P_{eS} = 6 \left(\frac{L_s}{H} \right)^2 P_{eH} \quad (19)$$

expresses the Peclet number associated with the sensor. P_{eS} describes whether the depletion region is large or small with respect to the sensor dimensions. $P_{eS} \ll 1$ is typically experienced by nanosensors such as nanowires, where the depletion region can be smaller the height of the channel but larger than the sensor. On the other hand, common sensors with micron-range size and operated at rather high flow rates exhibit both high P_{eH} and P_{eS} . In this latter case, the surfacic flux at the sensor's surface can be expressed as:

$$j_D \sim \frac{Dc_0}{\delta_s} \sim (P_{eS})^{\frac{1}{3}} \quad (20)$$

Interestingly, the flux at the sensor surface only weakly depends on the flow rate in the channel. A 1000-fold increase of the flow rate Q will only result in a 10-fold increase of the flux of molecules at the sensor surface.

The introduction of microbeads as capturing objects instead of a planar sensor at the bottom of the channel will tremendously complexify the resolution of mass transport equations. Hence, we propose to derive an intuitive description of the mass transport behavior in the case of high P_{eH} and P_{eS} . In that specific case, micron-sized beads are small enough to be assimilated to planar sensors stacked upon the entire height of the channel [11]. Their respective depletion regions will not overlap and therefore the collection rate in the presence of beads will scale linearly with beads number. Consequently, they can collect significantly more molecules than a simple planar sensor, ultimately increasing the output signal of the sensor and significantly reducing the sample loss.

3 Uniting mass-transport and binding kinetics

In the previous sections, we extensively describe the two main phenomena directing target collection, namely mass-transport and binding kinetics. Both compete to assess whether the reaction will be limited by the transport of molecules to the sensor or the binding event occurring at its surface. Assuming that $P_{eH} \gg 1$ the flow of analyte at the sensor surface brought by mass-transport is given by:

$$j_D \sim \frac{D(c_0 - c_s)}{\delta_s} \quad (21)$$

Where c_s is the concentration of probes at the sensor surface. The initial reactive flux can be derived from equation 1 as:

$$j_R \sim k_{on}\Gamma_0 c_s \quad (22)$$

Assuming a quasi-steady binding we can balance the reactive and mass-transport flux to find the concentration at the surface of the sensor[7]:

$$j_R = j_D \Rightarrow \frac{c_s}{c_0} \sim \frac{1}{1 + \frac{k_{on}\Gamma_0\delta_s}{D}} \sim \frac{1}{1 + D_a} \quad (23)$$

Where

$$D_a = \frac{k_{on}\Gamma_0\delta_s}{D} \quad (24)$$

is the ratio of diffusive over reactive flux, also named Damkohler number. If $D_a \gg 1$ then $c_s \sim 0$ and the reaction is limited by mass-transport. Each molecule brought by diffusion will instantly be collected by the sensor. On the other hand, if $D_a \ll 1$ then $c_s \sim c_0$ and the binding events are not frequent enough to bind the analyte if brought in the vicinity of the sensor.

It is noteworthy that the introduction of a spherical surface will have no influence on binding kinetics in the channel but will enhance mass transport behavior, as shown above, resulting in a decrease of the Damkohler number.

4 Objectives and thesis outlook

The previous section discusses the behaviors directing the collection of analytes at a sensor surface. The capture of target molecules mainly relies on the binding affinity of the probe with the analyte, a parameter that cannot be easily modified without designing new probes. The mass-transport aspect nonetheless can be largely impacted by the use of microfluidic channels, thanks to modification in the channel geometry and applied flow rates. We also demonstrated with simple calculations the benefits of using microparticles instead of planar surfaces to collect analytes, both in diffusive- and convective-dominated configurations. In this thesis, we introduce novel methods to handle and maintain microparticles, namely decorated beads and single cells, against the flow in order to improve analyte collection and, ultimately, the assay's performance. Our systems present a wide variety of applications, ranging from immunotherapy to point-of-care diagnostics.

Chapter 1 focuses on the development and optimization of microfabrication processes carried out in the scope of the thesis. We present fast prototyping protocols that were implemented to simplify the validation of new microfluidic layouts. We also extensively discuss the integration of standing SU-8 electrodes within microfluidic channels. Finally, we introduce new hybrid SU-8/PDMS valves granting an active valving option to our systems.

Chapter 2 covers the retention of microparticles against the flow. The immobilization is performed thanks to hydrodynamic or dielectrophoretic (DEP) forces depending on the types of microparticles, cells or beads, and on the flow level in the microfluidic channel. Importantly, each layout offers the possibility to release microparticles after trapping with numerous advantages, such as the opportunity to further study cells after on-chip incubation or to clean the device from beads for further use.

Chapter 3 presents possible applications of our retention technology in the diagnostics field. Two distinct platforms are introduced: a DEP-based device for the simultaneous detection of acute kidney injury marker (AKI) in point-of-care settings and a hydrodynamic-based system for sequential detection of multiple markers thanks to DNA barcoding. Both approaches are extensively described and characterized. The first system performs the concomitant assessment of clinical levels of two AKI markers, NGAL and Cystatin C, in a minimally diluted buffer. The second technology demonstrates the successive hybridization and detachment of DNA barcodes labelled with fluorophores at the surface of microbeads.

Chapter 4 focuses on the consequences of exposing single cells to flows in a microfluidic platform. In order to precisely understand such aftereffects, we independently assess the phenotypical impact of DEP actuation and injection in a microfluidic device on lymphocytes. The conclusions of the RNA-sequencing protocol performed are illustrated and discussed.

Chapter 5 provides suggestions on how to further develop the projects presented in the scope of the thesis and proposes a comprehensive list of research fields that could benefit from the novel technologies introduced in this manuscript.

1 Fabrication methods for particle manipulation in microfluidics

Disclaimer: The work presented in this chapter is partially adapted from the following article:

Thiriet, P.-E.; Pezoldt, J.; Gambardella, G.; Keim, K.; Deplancke, B.; Guiducci, C. Selective Retrieval of Individual Cells from Microfluidic Arrays Combining Dielectrophoretic Force and Directed Hydrodynamic Flow., *Micromachines*, 2020

My contribution: Conceptualization, methodology, validation, investigation, writing and editing.

This chapter presents the microfabrication processes developed in the scope of this thesis. Our work was based on established protocols that were tailored to our specific needs, namely the efficient exposure of microparticles to flow. This chapter is divided in three main sections: section 1.1 discusses the introduction of fast prototyping methods to validate the performance of our microfluidic systems, section 1.2 presents the integration of 3D electrodes in microfluidic channels to embed actuators close to microparticles and finally section 1.3 describes the development of hybrid PDMS/SU-8 valves for accurate handling of fluid.

1.1 Prototyping of microfluidic devices

The design of a complex microfluidic chip requires a careful optimization of the device layout. Such optimization have been partially carried out through simulations [12], as discussed later in this thesis. Another approach, explored in the scope of this thesis, consists in the iterative fabrication of microfluidic prototype that can be experimentally validated. In this this section we present two prototyping approaches that have been implemented.

1.1.1 Fabrication of SU-8-based micro-channels

SU-8 is a negative epoxy-based resist allowing the patterning of high aspect ratio structure [13], making it an ideal material for the design of 3D topologies. Good transparency properties, bio-compatibility and chemical resistance favored its integration in numerous microfluidic devices with biological applications [14, 15], and its critical dimension of $1\text{ }\mu\text{m}$ allows for an accurate manipulation of cells [16].

We developed processes for the fabrication of SU-8 channels with a height ranging from $15\text{ }\mu\text{m}$ to $50\text{ }\mu\text{m}$, allowing the optimization of microfluidic channels dimensions prior to integration of more complex features such as standing electrodes.

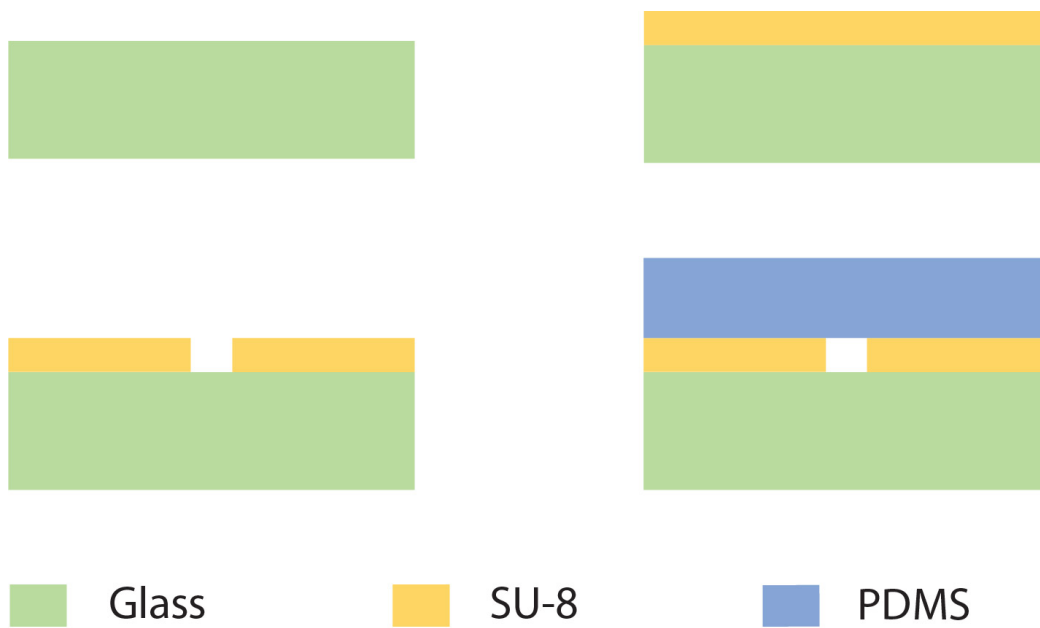


Figure 1.1: **Process flow of the fabrication of SU-8 microfluidic channel** The resist is spin-coated on the surface of a glass wafer, then exposed to UV light, baked and developed in PGMEA.

Figure 1.1 describes the corresponding process flow. The photoresist (SU-8 25, Kayaku) was spin-coated at a desired speed on a glass substrate. Glass was chosen as substrate material due to its excellent transparency and chemical resistance. Following a softbake at 95°C , the wafer was exposed to UV light. Then we carried out two post-exposure bake at 65°C and 95°C in order to catalyze the cross-linking of the polymer. The un-crosslinked photoresist was removed in a development step performed in Propylene Glycol Monomethyl Ether Acetate (PGMEA). Finally the microfluidic channel was closed with PDMS cover.

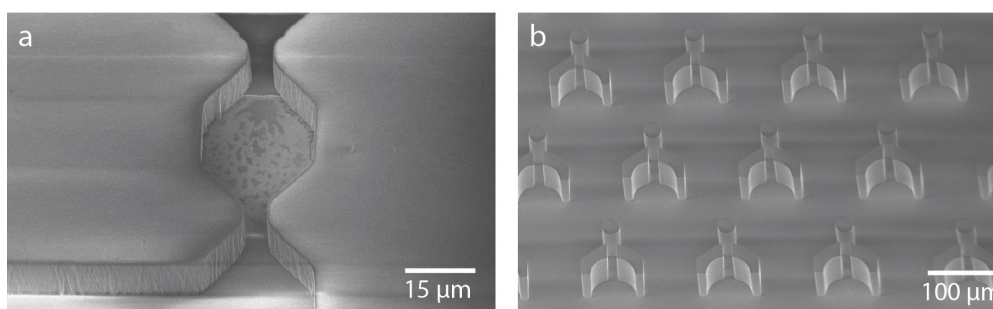


Figure 1.2: **SEM pictures of SU-8 microfluidic channels** Microfluidic channels having $15\mu\text{m}$ (a) and $50\mu\text{m}$ (b) height microfluidic channels were produced in SU-8 to assess the performance of the microfluidic layout

Figure 1.2 shows Scanning Electron Microscopy (SEM) pictures of SU-8 microfluidic channels with a height of $15\mu\text{m}$ (Figure 1.2a) or $50\mu\text{m}$ (Figure 1.2b). Exposure dose and development time were finely tuned to achieve an aspect ratio of 1:5 and the fabrication of trapping restriction as small as $5\mu\text{m}$, matching the state-of-the-art records [17] and demonstrating the versatility of the SU-8-based prototyping to design novel microfluidic platform. This process has been implemented for the validation of hydrodynamic traps performance, presented chapter 2 section 2.2. Besides this SU-8 microfabrication protocol, we employed as well PDMS-based microfluidic channels.

1.1.2 Fabrication of PDMS-based micro-channels

Following its introduction by the group of Prof. Whitesides in 1998, Poly Di Methyl Siloxane (PDMS) has quickly become the standard material for microfluidic prototyping [18]. Its unique properties opened new avenues in the bio-engineering field, revealing to the scientific community the potential of microfluidic systems. One could, among others, mention the introduction of Quake valves [19] or droplet microfluidics [20] that had a tremendous impact in the field of diagnostics[21], single-cell analysis [22] or drug discovery [23]. PDMS exhibits indeed good optical properties, biocompatibility [24] and chemical resistance, and can be very easily produced without the need of cleanroom equipment through soft lithography. Molds are commonly made of silicon or photoresist and fabricated by standard photolithography. In this section we explore both approaches for molds production and detail the obtained results in the scope of microfluidic channels prototyping.

Silicon-based molds

As silicon was historically the gold standard material for microelectronics, it was naturally one of the reference material for the first microfluidic platforms. Its surface functionalization has been extensively studied, allowing easy biochemical modifications [25]. The fabrication of PDMS stamps with silicon molds is presented in figure 1.3.

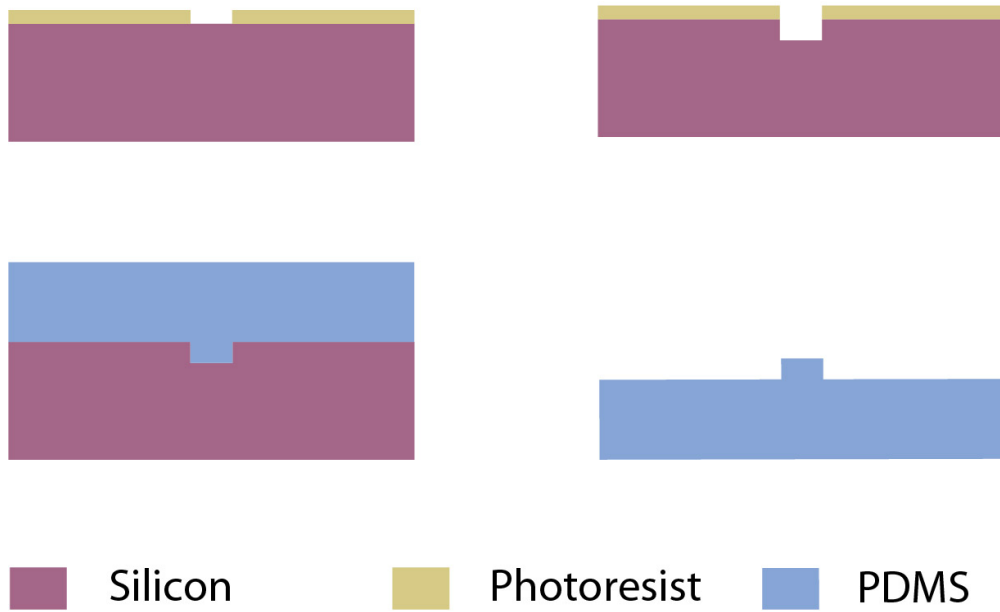


Figure 1.3: **Process flow of the fabrication of PDMS microfluidic channels with Si molds** The silicon molds are etched through Bosch process, then liquid PDMS is poured on the mold, cured at 80°C and stripped from the wafer.

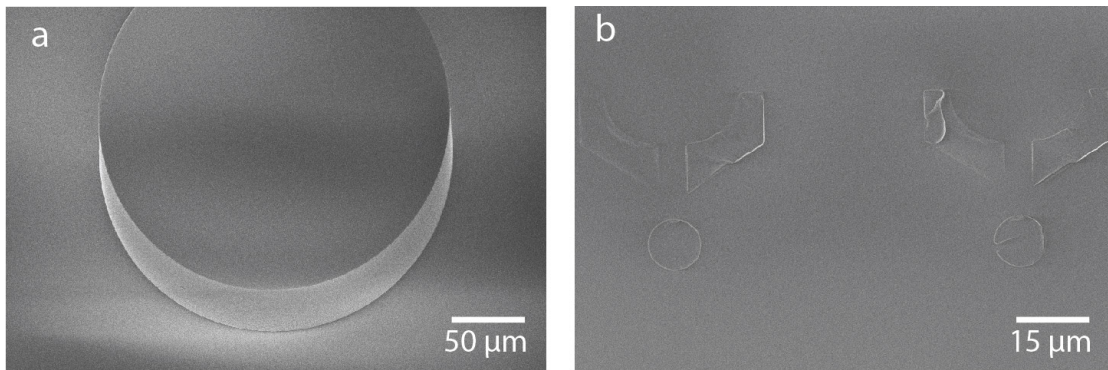


Figure 1.4: **SEM images of PDMS structures fabricated with Si molds** While the large structure could be efficiently transferred to the PDMS stamp (a) the transfer failed for smaller structure due to excessive adhesion (b).

The silicon molds were fabricated as followed: a first photolithography step was performed to pattern a positive resist on the silicon wafer. The un-protected area was then opened through Bosch process (AMS 200, Alcatel) and the remaining resist was stripped in an oxygen plasma. Prior to pouring the PDMS on the surface of the molds, the wafers were treated with oxygen plasma and Trimethylchlorosilane (TMCS) in order to reduce adhesion of the silicon with PDMS. After curing for 2 hours at 80°C, the PDMS stamps were carefully detached from the molds, activated in an oxygen plasma and bonded to a glass slide by gentle pressing. Such approach was successful for the fabrication of large structures such as integration of inlets or

outlets on a PDMS coverslip or control channels in a valve design (see section 1.3) as shown in Figure 1.4a. However, we could not achieve a reliable fabrication of fine and high aspect ratio PDMS structure, as shown in Figure 1.4b. This was caused by a strong adhesion of the PDMS to silicon, despite the TMCS pre-treatment. To tackle this issue we produced SU-8 molds which should feature a milder adhesion.

SU-8-based molds

SU-8 can serve the double purpose of constituting the core material of 3D microfluidic structures and being suitable as molds for PDMS modules. Its high resolution, durability and aspect ratio permits the fabrication of very reliable molds for a cost significantly lower than silicon-based molds [26]. In this section we pursued our efforts to develop fast prototyping methods and, to this end, we designed and fabricated high resolution PDMS microfluidic structures with SU-8 molds.

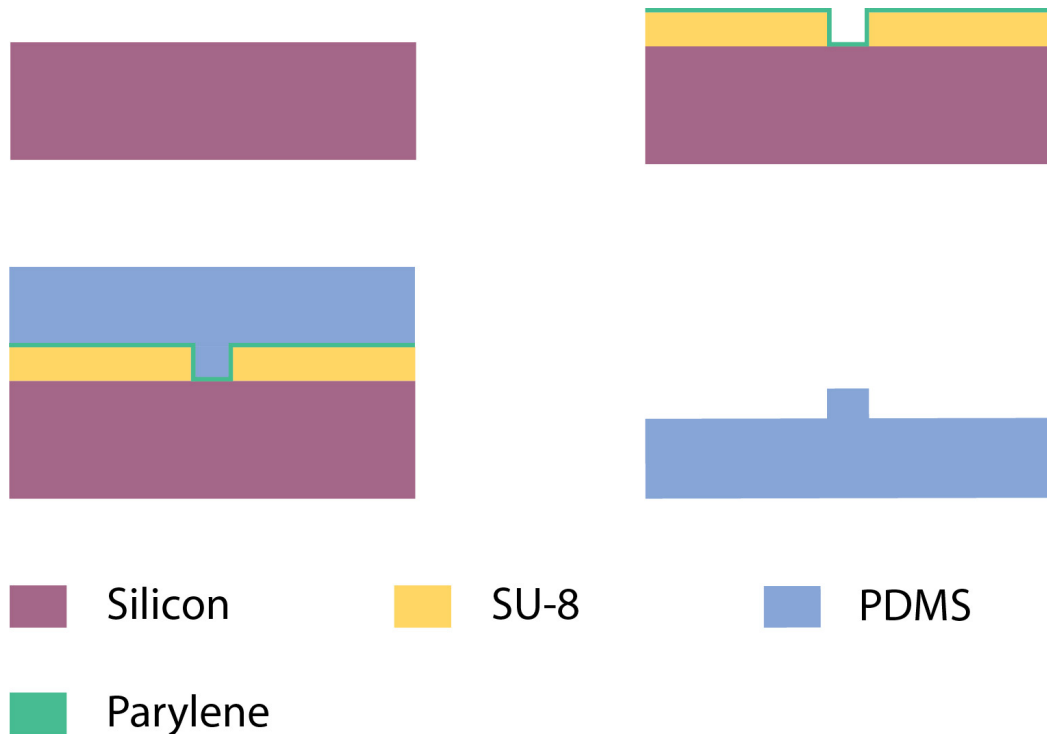


Figure 1.5: Process flow of the fabrication of PDMS microfluidic channels with SU-8 molds
The SU-8 resist is spin-coated on a silicon wafer, patterned with photolithography and covered with parylene for a reduced adhesion with PDMS.

Figure 1.5 details the fabrication process carried out to produce the SU-8 molds and PDMS stamps. The molds fabrication is very similar to the SU-8 microfluidic fabrication already presented. The desired thickness of SU-8 is first spin-coated and patterned through pho-

tolithography before development in PGMEA. Before pouring the PDMS we introduced a step of molds coating with a 500 nm layer of Parylene C in order to reduce adhesion of PDMS to the molds [27]. The very conformal deposition of parylene ensures a proper covering of high aspect ratio structures [28] and avoid the pre-treatment of the molds with TMCS, resulting a consequent reduction of the total fabrication duration. Microfluidic structures fabricated following this approach can be seen in Figure 1.6.

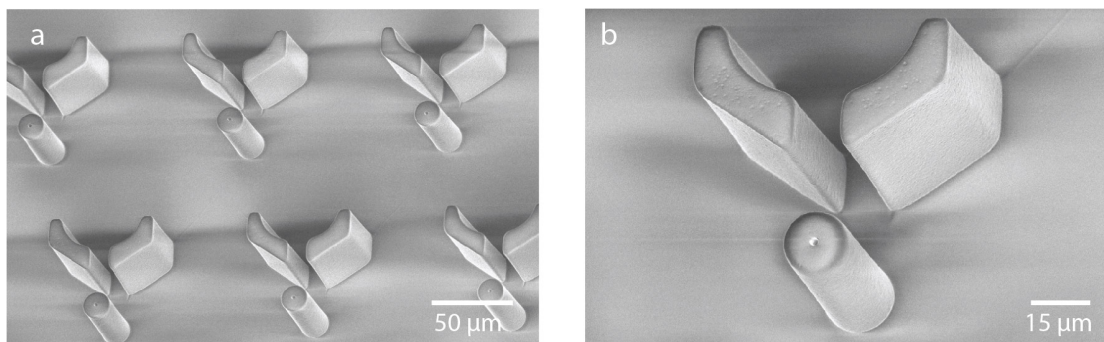


Figure 1.6: **SEM images of PDMS structure fabricated with SU-8 molds** High aspect ratio structures can be reliably transferred to PDMS stamps with the SU-8 molds coated with Parylene C.

The structures could be efficiently transferred from the molds to the PDMS. Despite an aspect ratio of 1:4, more than 99% of the structures were still standing at the end of the fabrication. The impact of Parylene C on the yield of standing structures has been assessed through the production of SU-8 molds deprived of Parylene coating but undergoing TMCS pretreatment prior to PDMS pouring. This resulted in a lower yield for the standing structures, around 95%, which is still considerably higher than the yield obtained with silicon molds for high resolution structures. The devices presented in section 2.2.3 for immobilization of single beads against the flow were fabricated according to this method.

We investigated in this section three protocols for fast prototyping of microfluidic channels, each presenting specific advantages and limitations. While allowing the best resolution in the microfluidic designs, the SU-8-based microchannels suffer from its inherent complexity and cost. SU-8 molds coated with Parylene consequently appear as the most suitable solution for rapid prototyping of PDMS devices.

1.2 Integration of 3-D electrodes in a microfluidic channel

In order to exploit even further the new doors opened by the microfluidic area, researchers have early on attempted to integrate electrodes within microfluidic channels, thus combining the performance of microfluidic systems with electrical sensing and actuation technologies. The results matched their expectations and numerous systems were designed, allowing for the analysis of single-cells through impedance spectroscopy [14], electro-rotation [29]

or dielectrophoresis. Cells could also be sorted in-flow depending on their dielectric properties [30] or deflected by dielectrophoretic forces [31]. Adapting electrophoresis to microchannels significantly enhanced the separation of chemical species [32]. The most intuitive solution to integrate electrodes in a microfluidic channel was to pattern planar electrodes at the surface of the substrate, typically with a lift-off process [33]. The use of planar electrodes faces however several limitations including a non-uniform electric field over the channel height [34]. Such non-uniformity hinders the possibility to increase the height of the channel and consequently limit the throughput of the system.

Three-dimensional electrodes overcome this issue as they can generate homogeneous electric fields. Such structures have been successfully designed by Martinez-Duarte et al. [35] through pyrolysis of photoresist structures and employed to study bacterial reaction to antibiotic treatment. Metal ion implantation in PDMS channels is also a promising path for 3-D structures [36], but both solutions suffers from an intrinsic lack of accuracy hindering a high resolution integration of electrodes inside the microfluidic channel. In this section we present a method for a versatile but yet very accurate integration of three-dimensional electrodes within a microfluidic channel.

1.2.1 Microfabrication process flow for 3-D electrodes integration in a microfluidic channel

The process flow discussed in this part was originally published in our lab by Kilchenmann and Rollo [37], it has been adapted in the scope of this thesis to embed electrodes within microfluidic channels as shown in Figure 1.7.

First a 20/200/20 nm layer of Ti/Pt/Ti was sputtered on top of a glass substrate. Titanium is used here as a intermediate layer to improve the adhesion between glass and platinum [38]. Planar metal lines were then patterned in a standard photolithography and ion beam etching (IBE, Veeco Nexus IBE 350, Veeco) step. In order to minimize exposure of the planar metal lines to the liquid in the channel the lines were passivated with silicon oxide. A 300 nm layer of silicon oxide was sputtered over the entire wafer surface and etched in the 3-D electrodes standing regions. Cylindrical pillars of SU-8 with a height ranging from 15 μm to 50 μm were fabricated on top of the metal lines. Then the entire surface of the wafer was covered with a 20/200 nm layer of Ti/Pt. This metal layer is subsequently etched everywhere but on the pillars sidewalls with a vertical ion beam etching. Finally a SU-8 photolithography is performed to define the microfluidic channel.

The last SU-8 development appeared as the most critical step in the process, as a too short development time will result in a clogging of narrow structures and a too long development will lead to delamination of the microfluidic channels.

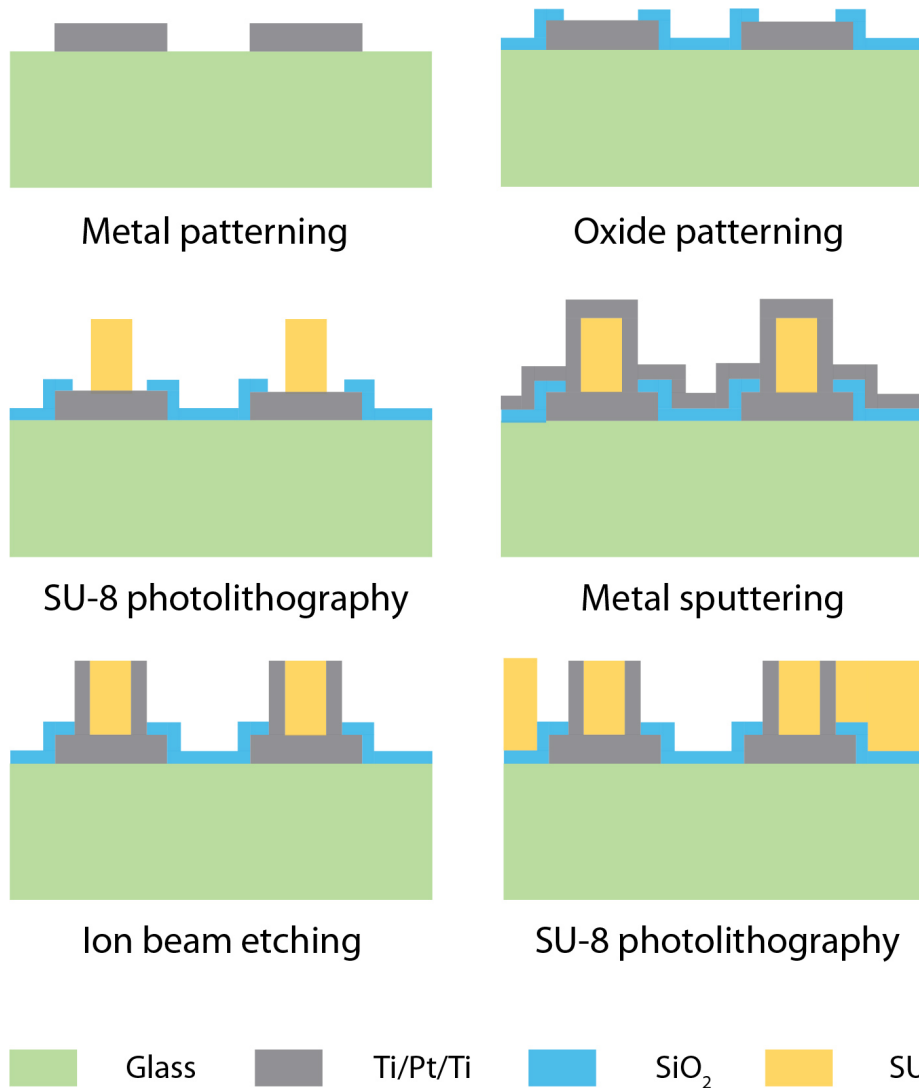


Figure 1.7: **Process flow of the fabrication of standing electrodes embedded in a microfluidic channel** Planar electrodes are partially insulated with silicon oxide, then a first SU-8 lithography patterns the scaffold of the electrodes on the top of the open metal regions. The pillars are covered with a metal layer that is etched everywhere but on the pillars sidewalls with ion beam etching. Finally a SU-8 photolithography is performed to define the microfluidic channels

Figure 1.8 presents a set of layouts combining microfluidic channels and three-dimensional electrodes. It clearly shows that we could consistently achieve a very accurate integration of electrodes in a channel, with in some case less than $3\text{ }\mu\text{m}$ extrusion of the electrodes out of the microfluidic. As discussed further in the thesis, this permits a close proximity between the area of interest in the microfluidic channel and the electrokinetic actuator. The adaptability in the design of the electrodes and microfluidic channels, only limited by the photolithography

step, calls for the exploration of new layouts that could reveal novel behaviors. Such investigations were performed in the scope of this thesis and will be presented in the next chapters, more specifically, section 2.2.2 discusses the introduction of this technology for selective single-cell trapping and release and section 2.3 investigate the use of such electrodes for microparticles manipulation within a microfluidic channel. Nonetheless, we are convinced this technology can still provide a significant contribution to the bioengineering field.

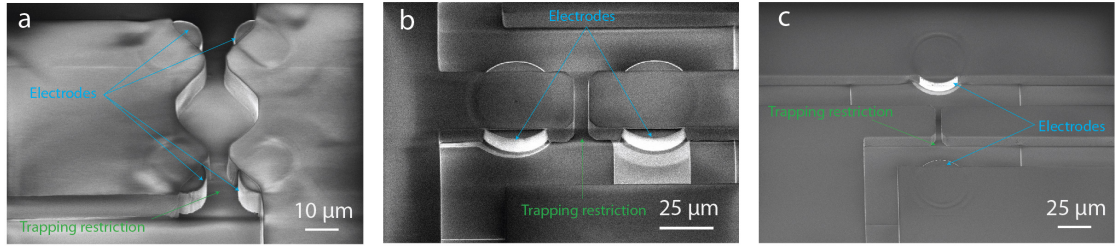


Figure 1.8: **Images of 3D electrodes embedded inside a microfluidic channel** In each of the three presented layouts the electrodes could be integrated in the microfluidic channel with a micron-range accuracy

1.2.2 Characterization of electrodes

The characterization of the electrodes is a critical aspect in the implementation of standing electrodes, as we need a quality control tool to verify that the current can access the metal side-walls. Such investigation was carried out through the combination of impedance spectroscopy and dedicated test structures on each wafer.

Impedance spectroscopy, a powerful tool for electrical properties assessment

Impedance spectroscopy is a label-free technique for non-invasive system characterization. Originally developed for material science applications [39], it was successfully adapted to probe electrical properties of biological systems such as cells [40] or bacteria. For instance Rollo et al.[16] used it to sort activated T-lymphocytes from non-activated ones and Zhou et al. [15] to monitor the differentiation of mesenchymal stem cells on chip. Impedance is obtained from the response of the current to the varying frequencies of a low amplitude sinusoidal voltage [41].

In the absence of faradaic process, a liquid/electrode interface can be simply modeled as a resistance (R) placed in series with a capacitance (C), where the resistance accounts for the ionic current within the liquid and the capacitance takes into account the charges accumulation at the interfaces between the liquid and the electrodes, also known as the double layer capacitance C_{DL} . Such description is inherently incomplete, nevertheless it can predict accurately the behavior of the liquid electrode. The impedance of such system can be expressed as:

$$Z(j\omega) = R + \frac{1}{j * C_{DL}(j\omega)} \quad (1.1)$$

From this equation we expect a main contribution of the capacitance at low frequencies (before 100kHz) and a strong contribution of the resistance at high frequencies (above 100 kHz) as we can see on figure 1.9. The decrease of the impedance above 10 MHz is due to the presence of parasitic capacitance effects [42] not included in our simple model.

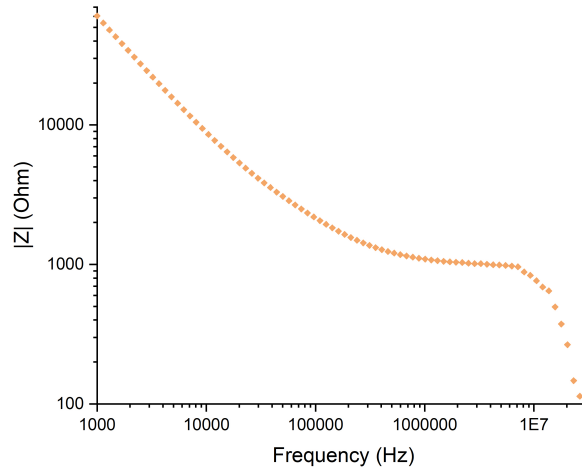


Figure 1.9: **Experimental plot of the impedance module of a liquid/electrode interface** At low frequencies the capacitance has the highest influence on the impedance module while at high frequencies the resistance shows a stronger contribution.

Test structures layout and characterization

In order to validate the presence of a good electrical contact between the planar metal lines and the metal sidewalls of the pillars we need to design a system that would behave steadily in the absence of the aforementioned contact but shows some changes once this contact is made. The double layer capacitance can be expressed as:

$$C_{DL} = c_{DL} A \quad (1.2)$$

Where c_{DL} is the capacitance per unit surface, typically $20 \mu F/cm^2$, and A the area of liquid metal interface. In Figure 1.10 we present our test structure: we designed 3 sets of 3D electrodes with various lengths and consequently different capacitance according to 1.2. When we measure the impedance of such structures we expect to observe a different behavior at low

1.2 Integration of 3-D electrodes in a microfluidic channel

frequencies in the capacitive region if the electrodes are actually connected, otherwise we will monitor a constant impedance signal.

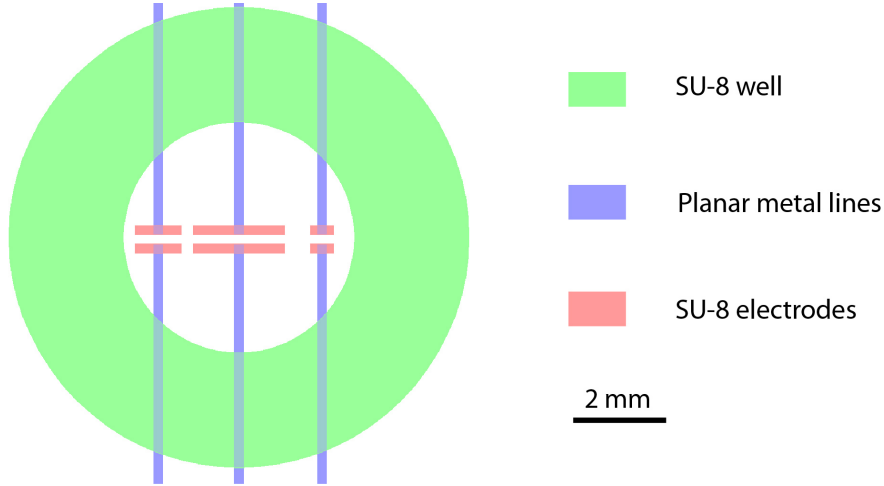


Figure 1.10: **Layout of the impedance test structures** Three sets of 3D electrodes are placed in front of each other, the distance between the 3D electrodes is of $200\ \mu\text{m}$, the lengths of the structures are of 1 mm, 2 mm and 0.5 mm, respectively. The electrodes are placed in a SU-8 well that is filled with PBS for the measurements. The height of the 3D electrodes is $15\ \mu\text{m}$.

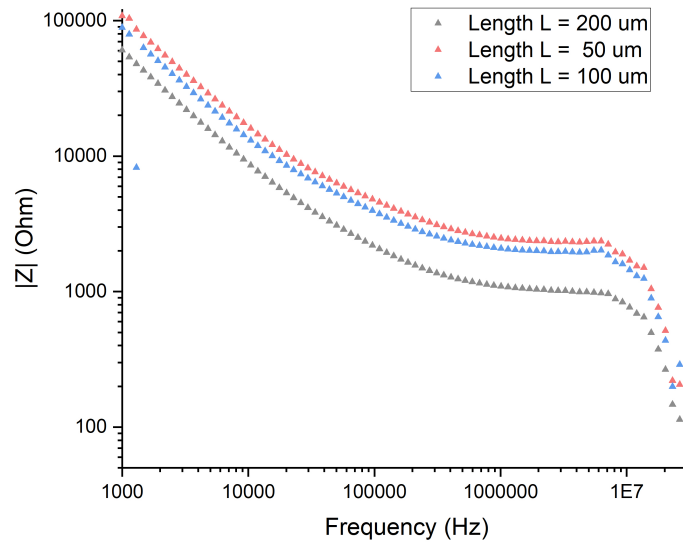


Figure 1.11: **Plot of the characterization of the impedance test structures** The three plots correspond to the different lengths of the "capacitors-like" structures. The measurements were performed in PBS with a Agilent 4294A impedance spectrometer.

Figure 1.11 presents the results of the characterization, the SU-8 well was filled with Phosphate Buffer Saline (PBS) and the impedance was measured through the application of a 300 mV voltage with a Agilent 4294A. We notice a clear difference in low frequencies signals, indicating a change of capacitance. As the length of the structures increases, its area increases, resulting in an increase of the double layer capacitance (Equation 1.2) and consequently a decrease of the impedance (Equation 1.1). Such reduction is evident from Figure 1.11, validating our approach to investigate the electrical contact between the planar lines and the 3D electrodes.

This section presents and discusses a method to validate our 3D electrodes performance, a critical asset in the design of new microfluidic platform. It helps us troubleshooting whether an unexpected behavior of the chip is caused by a defective contact between planar lines and 3D electrodes. Consequently such structures have been routinely tested throughout all the thesis to discard chips exhibiting contact issues.

1.3 Hybrid SU-8/PDMS valves for hard photoresist-based microfluidics

Since their first introduction in the early 2000 [19], microfluidic valves such as Quake valves have been successfully integrated in many lab-on-a-chip devices. They indeed allow to parcelize nanoliters volume of liquid or to simply and selectively exchange buffers in a microchamber. Potential applications include highly multiplexed immunoassays for immunogen detection [21], screening of drug candidate for hepatitis C [23] or investigation of single-cells properties [43]. Those platforms benefit from minimal reagent consumption, low sample processing and a high throughput in the analysis. However most of the aforementioned devices relies on all-PDMS microfluidics, which implies that both the control and fluidic channels are made of an elastic material. Our aim in this section is to present the design and implementation of valves that can operate on top of hard microfluidic channels. The fabrication protocol we developed is presented in figure 1.12.

The PDMS valving system placed on the top of the microfluidic channel is composed of two layers: a control layer made of a thick PDMS layer and a thin membrane that will be deflected in order to close or open the microfluidic channel. The fabrication of the molds for the control layer is carried out with standard photolithography and dry etching (AMS 200 Alcatel) on a silicon wafer. As presented in section 1.1.2 earlier in this chapter PDMS prepared at a ratio of 5:1 is poured over the silicon mold which has previously been treated with trimethylchlorosilane (TMCS). The membrane is fabricated by spin-coating PDMS at a ratio of 20:1 on a TMCS-treated silicon wafer, the speed of rotation is 2500 rpm and results in a thickness of 15 μm . Both this PDMS membrane layer and the lid PDMS layer are partially cured at 80 °C for 30 min and then aligned and bonded at 80 °C for 1.5 h. Finally, the PDMS coverslip is treated with 3-aminopropyl triethoxysilane (APTES) and irreversibly bonded by incubating the system at 150 °C for 2 h. This step presents some experimental challenges, since the alignment of both the fluidic and control channels is carried out manually. Additionally, pressing the

1.3 Hybrid SU-8/PDMS valves for hard photoresist-based microfluidics

chip with the PDMS coverslip with too much pressure might lead to the adhesion of the membrane with the bottom of the channel before the baking step, resulting in irreversible bonding between the membrane and the microfluidic channel after curing, preventing the valve from operating properly.

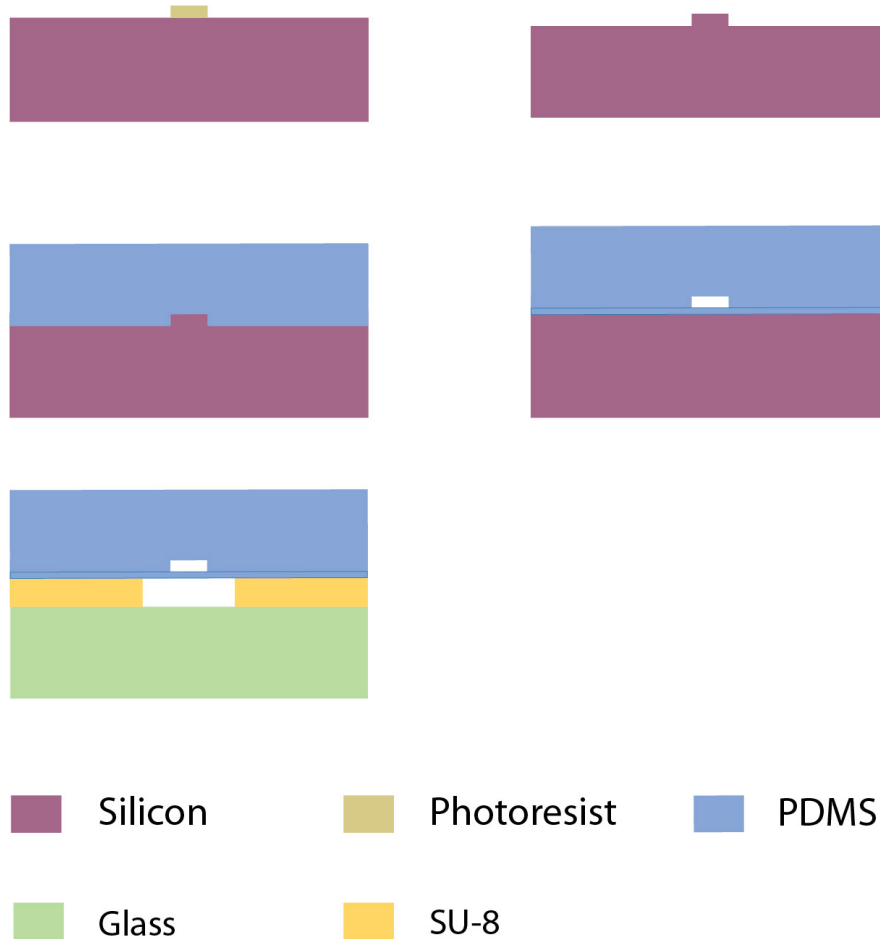


Figure 1.12: **Fabrication of PDMS valves on top of SU-8 channels** Molds are fabricated in Silicon as presented in section 1.1.2. They are used for the molding of the PDMS control channels, while the PDMS membrane is spin-coated on a blank wafer, transferred on the control channel PDMS stamp and finally bonded to SU-8 microfluidic device trough APTES bonding.

Figure 1.13 shows an efficient handling of the valves, the main difference with a standard PMDS Quake valve configuration is the pressure that has to be applied to seal the valves. From 800 mbar for a standard valves it went up to 3500 mbar in our case. The application of a pressure exceeding 4000 mbar would result in the destruction of the PDMS to SU-8 bonding. Despite the increase in pressure we could not achieve a perfect sealing, yet the performance of our valves was sufficient to ensure that no cells would flow through a closed valve (See section 2.2.2). Previous studies have proposed solutions to integrate valves within microfluidics

that were fabricated with hard material, as in our case. Huang et al. [44] designed valves by means of a PDMS layer sandwiched between two poly(methyl methacrylate (PMMA) channels. Similarly, Lee et al. [45] integrated a PDMS membrane between two polycarbonate (PC) layers.

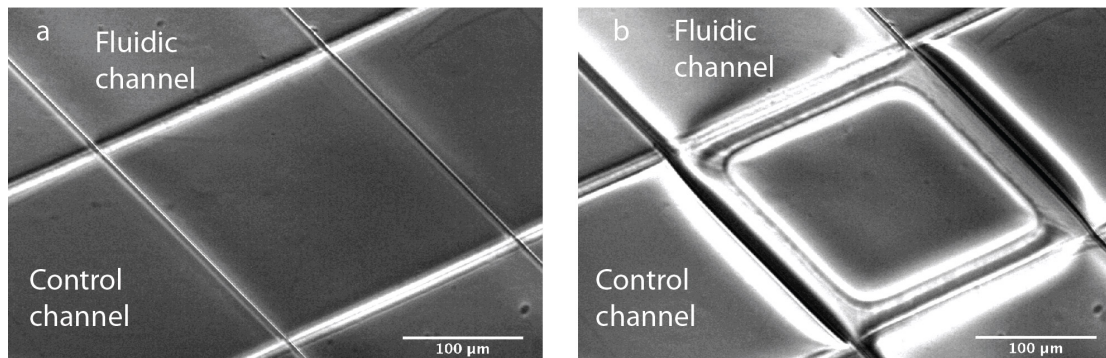


Figure 1.13: **Operation of the hybrid SU-8/PDMS valves** Pictures of the valves before (a) and after (b) application of pressure to close the valve.

1.4 Summary and conclusion

In this chapter we presented a set of tools for fast microfluidic prototyping as well as complex devices combining microfluidics with electrokinetics fabrication. Such solutions were developed with the aim to investigate interactions between particles and analytes in the context of convective flow. The first step in such study is to perform immobilization of particles in a microfluidic channels and this aspect will be discussed in the following chapter.

2 Microparticle handling and reversible trapping in microfluidic channels

Disclaimer: The work presented in this chapter is partially adapted from the following articles:

Thiriet, P.-E.; Pezoldt, J.; Gambardella, G.; Keim, K.; Deplancke, B.; Guiducci, C. Selective Retrieval of Individual Cells from Microfluidic Arrays Combining Dielectrophoretic Force and Directed Hydrodynamic Flow., *Micromachines*, 2020.

My contribution: Conceptualization, Methodology, Validation, Investigation, Writing and Editing.

Thiriet, P.-E.; Medagoda, D.; Porro, G.; Guiducci, C. Rapid Multianalyte Microfluidic Homogeneous Immunoassay on Electrokinetically Driven Beads., *Biosensors*, 2020.

My contribution: Conceptualization, Methodology, Validation, Formal Analysis, Investigation, Data Curation Writing and Editing.

The study of the in-flow interaction between particle and analyte underlies some methods to hold a particle against the flow. The immobilization of particles in a microfluidic channel for continuous monitoring of their properties has been an important challenge in the microfluidic field in the past two decades that fueled the introduction of many successful technologies [46]. Mechanical trapping is probably the most straightforward strategy, its easiest form being the use of microwells in which the particles will sediment due to gravity [47]. Another approach, referred to as hydrodynamic trapping, relies on the use of mechanical restrictions that can create a preferential path for the particle to stop [48]. More original methods were proposed to meet specific biological requirements such as acoustic trapping [49] or optical tweezers [50]. The retrieval of a target particle after the immobilization and study appears as very promising yet still largely not achieved feature in microfluidic systems. In cells-based

systems this translates into the possibility to recover cells from the chip for further expansion and analysis, while in beads-based devices for diagnosis it grants a efficient cleaning of the chip for later reuse. In this chapter we present and discuss the trapping and release of cells and beads within a microfluidic channel thanks to a combination of mechanical and dielectrophoretic mechanisms. More specifically, section 2.1 will present and discuss the theoretical background of DEP forces operation for microparticles handling, section 2.2 will describe the implementation of two different layouts for the mechanical trapping of cells and beads, respectively. Finally, section 2.3 will focus on the use of DEP forces to manipulate microbeads in a microfluidic channel.

2.1 Dielectrophoresis, a powerful tool for particles manipulation

Dielectrophoresis (DEP) is observed upon placing a polarizable particle in a non-homogeneous electrical field. The electrical field gradient induces a polarization of the particle, thus creating a dipole. This dipole, placed in a electrical field, experiences a net force called dielectrophoretic (DEP) forces. The direction of this force depends on the relative permittivity of the particle and its surrounding medium, quantified by the Clausius-Mossotti factor given in equation 2.1:

$$f_{CM}(\omega) = \frac{\epsilon_p^*(\omega) - \epsilon_m^*(\omega)}{\epsilon_p^*(\omega) + 2\epsilon_m^*(\omega)} \quad (2.1)$$

Where ϵ_m is the permittivity of the medium and ϵ_p the permittivity of the particle. If the particle is more polarizable than its surrounding medium, i.e. the real part of the Clausius-Mosotti factor is positive, then the negative charges will travel to the positive pole and the positive charges will travel to the negative pole. This results in a orientation of the dipole along the electrical field. The particle will then move towards the stronger field region upon effect of the so-called positive DEP (pDEP). In case the polarizability of the surrounding medium is higher the one of the particle, i.e. the real part of the Clausius-Mossotti factor is negative, the particle will move towards the weaker field region due to negative DEP (nDEP). Both phenomena are depicted in Figure 2.1.

The relationship between the force applied on a spherical particle, the Clausius-Mossotti factor and the gradient of electrical field and the radius of the particle can be written as [51]:

$$F_{DEP} = 2\pi \cdot \epsilon_m \cdot R^3 \cdot \Re[f_{CM}(\omega)] \cdot \nabla E_{RMS}^2 \quad (2.2)$$

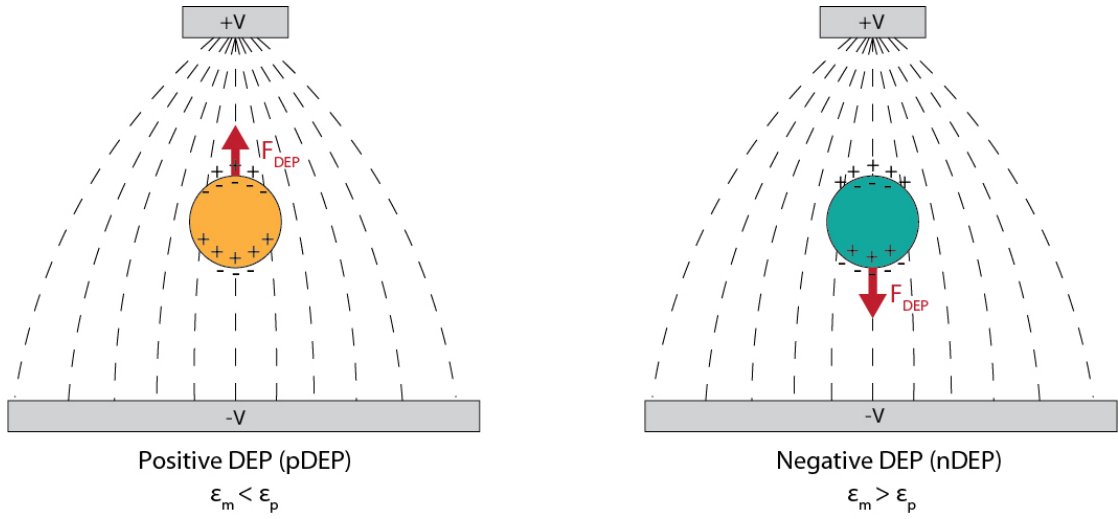


Figure 2.1: **Theoretical principle of dielectrophoresis** Depending on the value of its permittivity compared with the permittivity of the medium, the particle will either be attracted by the stronger field regions (pDEP) or the weaker field regions (nDEP).

Where F_{DEP} is the DEP force, R the radius of the particle and E_{RMS} the root-mean-squared value of the electric field. It is interesting to point out the strong dependence of the DEP force with the radius of the particle, greatly limiting the performances of DEP-based systems for manipulation of particles below 500 nm [52]. Equation 2.1 reveals that the sign of the Clausius-Mossotti depends on the frequency of the electrical field, one can then obtain, for the same particle placed in the same medium, either a positive or a negative DEP effect depending on the chosen frequency. The frequency at which the shift between pDEP and nDEP occurs is called the crossover frequency, and its determination can contribute to the sorting of cells of different kind, such as for instance stem cells [53].

The simplicity and versatility of DEP led to its adoption in the frame of numerous applications. Its main contributions stand in the field of particles sorting, as it could be used for efficient sorting of biological particles according to their size [54], shape, or dielectric properties [55]. Nevertheless, it was also successfully employed for protein enrichment [56], stream focusing for in flow analysis [57] or spatial containment of functionalized beads [58].

2.2 Hydrodynamic trapping of particles and strategies for their selective release

2.2.1 Hydrodynamic trapping

Hydrodynamic trapping is a method that permits the spatial arrangement of particles of a specific size range in different regions of a microfluidic channel. Trapping sites are defined by tight side-wall openings of low fluidic resistance where single particles are led to by the

laminar flow. Particles captured with this method are continuously exposed to a flow of analytes, allowing in the specific case of cells for delivery of nutrients and disposal of waste. Previous works characterizing hydrodynamic cell-trapping systems have reported a trapping efficiency—defined as the percentage of traps filled after injection of cells—between 75% and 99%. These methods have been used to capture multiple cell types [59] and, in some cases, to localize rare cells [60]. They also proved to be valuable tools for investigation of single-cell behaviors. For instance, Dura et al. [61] could conjointly place single dendritic cells and T-cells and measure heterogeneity in the activation of T-cells.

In this section we will present two different layouts implemented for the trapping of cells (section 2.2.2) and beads (section 2.2.3), respectively. The theoretical aspects of hydrodynamic trapping are discussed based on the design implemented for single cell trapping presented in figure 2.2.

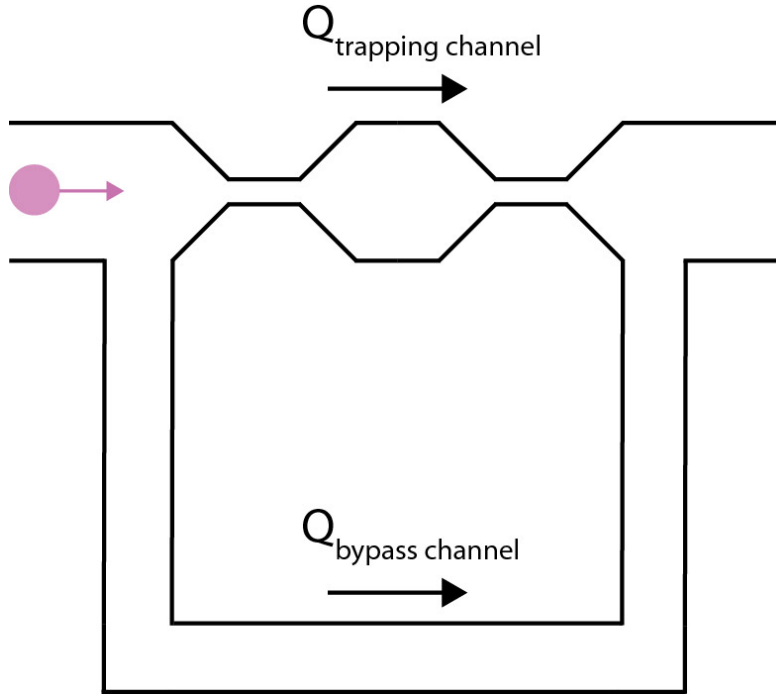


Figure 2.2: **Hydrodynamic trapping basic principle** Depending on the ratio between $Q_{\text{trapping channel}}$ and $Q_{\text{bypass channel}}$ the probability of the cell to be trapped will vary.

The main figure of merit describing the system illustrated above is the ratio between the fluidic resistance of the trapping channel and the fluidic resistance of the bypass channel. In order to achieve an efficient trapping this ratio should be comprised between 1.2 and 1.4 [12, 62] (equation 2.4).

$$1.2 < \frac{R_{\text{bypass channel}}}{R_{\text{trapping channel}}} < 1.4 \quad (2.3)$$

Adopting the common analogy adapting the Ohm's law of electrokinetic to microfluidic channel [63] the above condition can be also expressed as:

$$1.2 < \frac{Q_{trappingchannel}}{Q_{bypasschannel}} < 1.4 \quad (2.4)$$

Such ratio can be calculated for each specific design with a finite element simulation (see next section). The flow in the restriction has to be slightly higher than in the bypass channel. Once a particle is immobilized, the fluidic resistance of the trapping channel significantly increases and prevents any further trapping event. It is important to mention that an excessive flow in the restriction path will result in the trapping of multiple particles, while a too low flow will fail in trapping most of the particles entering the channel.

2.2.2 Single-cell immobilization and selective release

The association of hydrodynamic trapping with single cells study appears as a suitable strategy to achieve efficient exposure of cells to flow of analytes and therefore gain a better understanding of cellular behaviors [15], yet the possibility to retrieve a cell after its on-chip analysis for further characterization or expansion can unveil novel biological mechanisms. For instance, Kimmerling et al. [64] compared intra- and inter-lineage transcriptomes within a cell population by capturing multiple generations of a single starting cell in subsequent traps. In that study, the analysis of the transcriptome was performed upon the retrieval of the entire lineage from the chip. The release of cells from their hydrodynamic traps was carried through application of a backflow pushing the cell out of the trap. Yeo et al. [60] combined centrifugal and hydrodynamic forces to isolate circulating tumor cells from a mixed cell population; to enable release, each trap was connected to an independent backflow channel. This method is suitable for collection of extremely rare cells such as circulating tumor cells, but it suffers from very low throughput and poor scalability, as the number of cells that can be retrieved is limited by the number of backflow channels that can be placed on the chip. Tan et al. [65] could retrieve cells encapsulated in hydrogel beads, creating an air expansion on the trap site generated with laser heating. This platform is limited by the complexity of the setup and the damage to the cells that may be induced by heat. In this section we propose a technology associating hydrodynamic trapping and DEP-based release in order to selectively trap and retrieve single cells from a microfluidic device. The use of DEP actuation permits a selective release of single cells while limiting the footprint of the platform.

Layout description

The trapping units presented in figure 2.2 are arranged in a tree-like structure as shown in figure 2.3a,b. This parallel layout avoids the clogging of the entire chip in case large debris would enter the chip. The two valves located upstream allow control of liquid injection in the chip while the two valves located downstream enable the recovery of single cells. (Figure 2.3c).

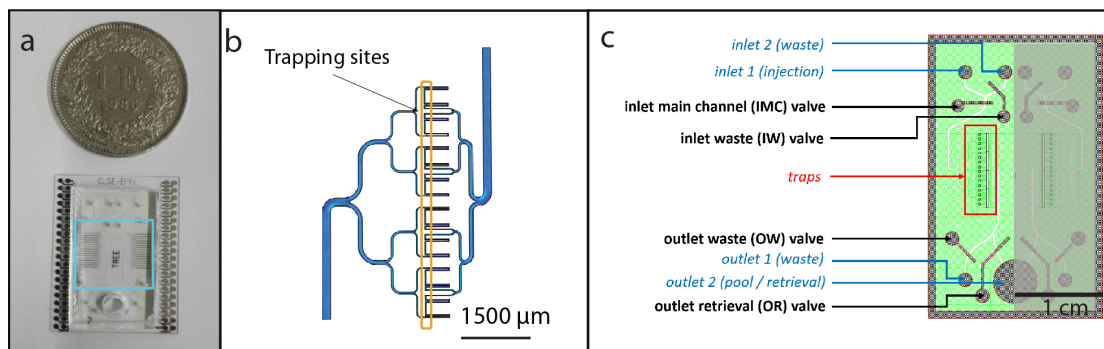


Figure 2.3: Cell trapping and release device layout (a) Picture of the microfluidic platform. The chip features two symmetrical channels sharing the recovery well. (b) Scheme of the tree-like structure implemented to reduce clogging concerns. (c) Microfluidic layout of the chip: The SU-8 based microfluidic channels are shown in green, while PDMS control channels are depicted in gray. When a cell enters the chip through inlet 1, it can be directed either towards the traps for immobilization and observation or to the inlet 2 if it needs to be discarded. After release for a trap, a cell can be recovered from the pool at outlet 2 or disposed through the outlet waste

The selective release is permitted by the integration of 3D electrodes in the close vicinity of each trap as shown in figure 2.4. Metal-coated SU-8 pillars will generate an electrical field

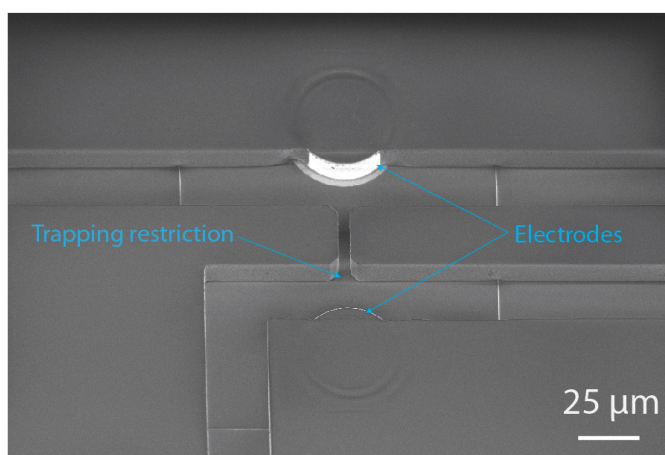


Figure 2.4: SEM image of a trapping and release unit The electrodes are integrated in close proximity of the trapping site to allow for application of minimal voltage during release.

gradient that will push the cells from their trapping location thanks to negative DEP. The height of the structure is $15\ \mu\text{m}$, significantly more than the average diameter of the targeted cell type, here T-lymphocytes with an average diameter of $10\ \mu\text{m}$. Such height was limited to $15\ \mu\text{m}$ to avoid stacking of cells in the traps. The trapping unit dimensions were determined thanks to finite element simulations of the fluidic and electric behaviors of the chip discussed in the next section.

Simulations

In order to ensure that the fluidic resistance ratio introduced in section 2.2.1 will stay in between 1.2 and 1.4, Comsol simulations were performed varying the dimensions of the bypass channel (cf Figure 2.2). The size of the aperture in the restriction was indeed set at $5\ \mu\text{m}$ to guarantee the trapping of the $10\ \mu\text{m}$ diameter lymphocytes. The simulation results reported in Figure 2.5 were conducted on a 3D model. The flow velocity in the channels was simulated using the Laminar Flow module and a normal mesh size, the pressure difference between inlet and outlet was set at 0.1 mbar and a no slip condition was applied on the fluidic walls (Figure 2.5 a).

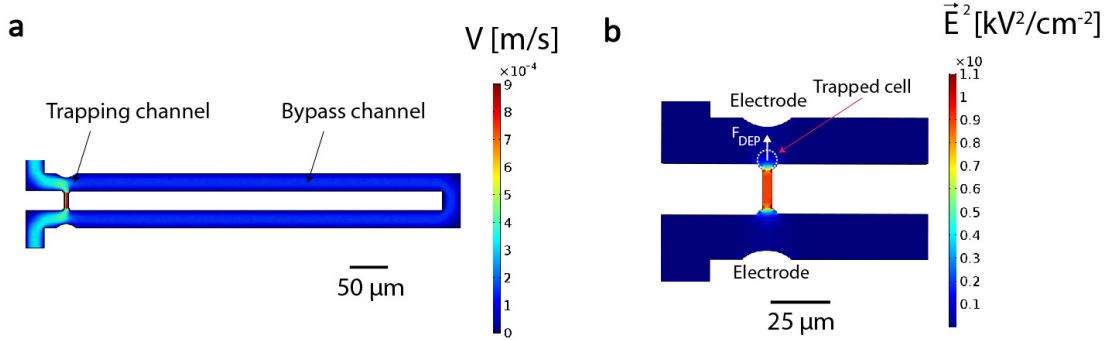


Figure 2.5: **Simulation of the fluid velocity and electric field in a trapping region** (a) Finite element simulation of the fluid velocity in the microfluidic channel used to determine the ideal length of the channel ensuring the trapping of a single cell (Inlet pressure: 0.1 mbar). (b) Finite element simulation of the electric field in the channel. The field gradient is higher in the trapping region of the cell, generating a negative dielectrophoretic (DEP) force sufficient for the release of the cell from the trap (voltage difference between electrodes: 10 Vpp).

The electrical field was also simulated to observe the distribution of the electric field gradient and then predict the direction and strength of the generated DEP forces. Figure 2.5 b shows that the electrical field lines are distorted by the insulating walls of the trapping restriction, resulting in the appearance of an electrical field gradient and subsequent DEP forces at this location, which serves our goal to push the cell out of the trap.

Results and discussion

In order to investigate the performance of our system for single-cell trapping and release, T-lymphocytes obtained from the Centre Hospitalier Universitaire Vaudois (CHUV) suspended in Roswell Park Memorial Institute (RPMI) supplemented with 10% fetal bovine serum (FBS) and antibiotics were injected in the device. Prior to injection cells were washed two times in PBS to discard dead cells and resuspended in RPMI at a concentration of 300'000 cells/mL.

Figure 2.6 presents the results for the trapping of lymphocytes. A lymphocyte is shown entering the microfluidic channel and being gently trapped in the fluidic restriction, validating the prediction of the Comsol simulation discussed above. The distance between the extruding electrode and the immobilized cell was set to 15 μm in order to allow other cells to travel throughout the channel without clogging risk. The percentage of traps filled a single-cell upon injection was typically found to be around 90%, which is in agreement with the values found in literature [66].

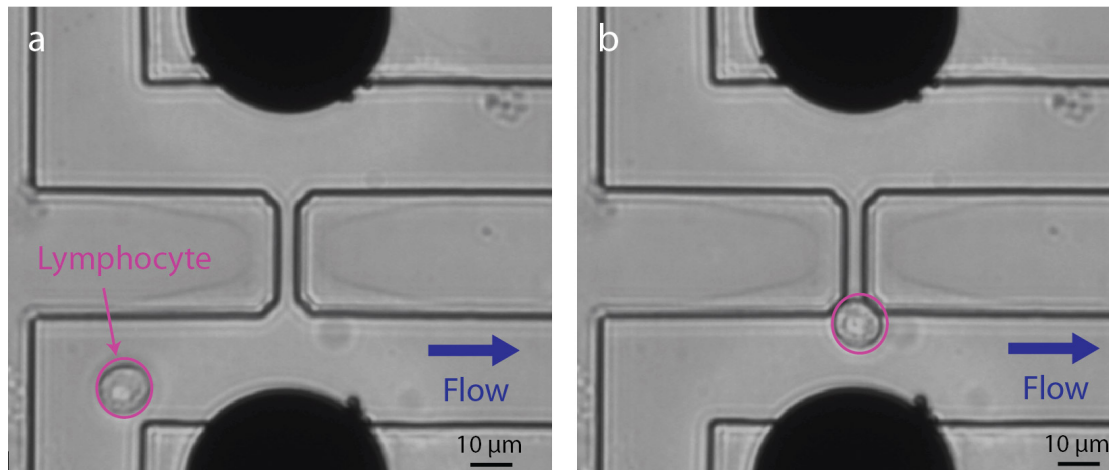


Figure 2.6: **Trapping of a lymphocyte in a microfluidic trap** The lymphocyte enters the microfluidic channel (a) and is immobilized in the microfluidic restriction (b).

Upon trapping of the cell the DEP-actuated release was tested by turning on the electrical field in the 3D electrodes. As discussed in the simulation section, the field gradient is higher in the trapping region. As the cell polarizability is lower than the polarizability of the surrounding medium the cell should be pushed towards the weaker field region i.e. out of the trap, by negative DEP. Figure 2.7 illustrate such release employing a voltage of 10 Vpp at 10 MHz. The optimization of the operation parameters was carried out both experimentally and theoretically. The frequency was maintained above 1 MHz to avoid electrolysis that could be observed below that threshold and could lead to gaseous species formation. The minimal voltage value experimentally-identified to trigger efficient release in our configuration is 8 Vpp. Hence, in order to minimize the impact of application of electrical fields on cells, we maintained the voltage applied to cells between 8 and 10 Vpp throughout this study.

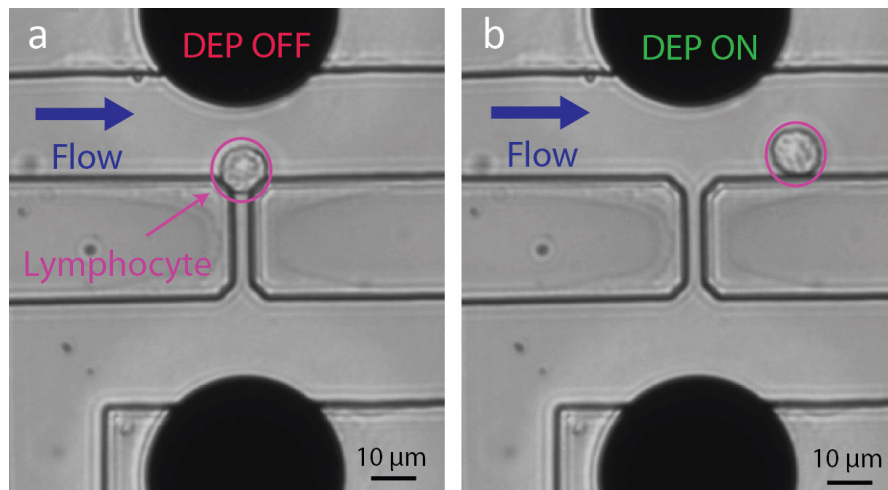


Figure 2.7: **Release of a lymphocyte from a microfluidic trap** The lymphocyte immobilized in the trap is gently released upon application of a 10 Vpp voltage at a frequency of 10 MHz.

A really useful add-on to our platform would be to have singularly addressable electrodes that would allow a selective trapping and release of cells. This was achieved through the development of a printed circuit board (PCB) that directs the signal to the desired set of electrodes. Figure 2.8 depicts the selective release of one lymphocyte. Such approach could have some future application in context of screening and selection of cells responding to a specific stimuli. [43].

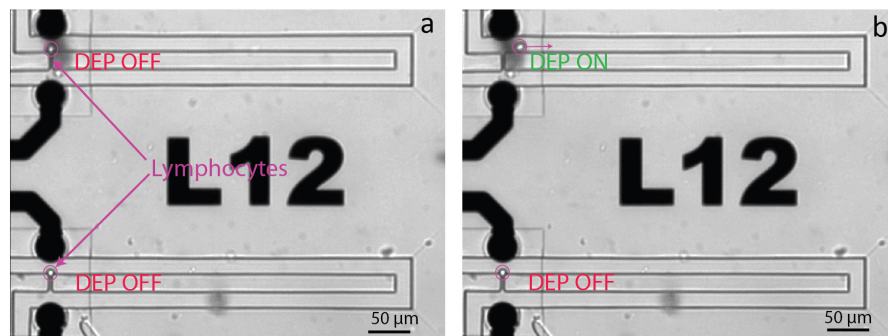


Figure 2.8: **Selective release of a lymphocyte from a microfluidic trap** The cell at the top is released, while the cell at the bottom is kept in the trap. The release is carried out with a 10 Vpp voltage at 10 MHz. A custom-made printed circuit board (PCB) enables the selective release of a single T lymphocyte.

The most immediate approach to generate an electric field in a microfluidic system is to place two electrodes at the inlet and exit reservoirs, respectively [67]. However, the large distance between the electrodes and the active regions where the electrical gradient is needed calls for high voltages [67], which comes with many drawbacks. For instance, (i) the need to generate high-amplitude AC signals, (ii) the generation of heat and (iii) the induction of

water electrolysis phenomena at the electrodes and consequent bubble generation, affecting cell viability. The integration of electrodes very close to the trapping regions hinders these limitations, as the signal amplitude can be greatly reduced. The 3D electrodes generate homogeneous DEP forces across the height of the channel, which decreases the amplitude of signal that we need to apply. In fact, we could set the amplitude of the DEP signals to lower values with respect to previous works that employ planar electrodes (10 Vpp of this work versus 20 Vpp [68]). Furthermore, we could afford to maintain the cells in their native medium (RPMI, conductivity 1300 mS/m) for all our experiments without observing electrolysis, a substantial advantage considering the constraints of cell biology. Since DEP forces are weakened by high ionic strengths, most designs employing DEP to apply electrokinetic forces substitute the native medium with a synthetic one with lower conductivity, also reducing electrolysis problematic [53, 68]. Hence, by being able to retain cells in their native culture medium, cellular stress is reduced, washing and centrifugation steps limited and general compatibility with conventional cell-based assays achieved.

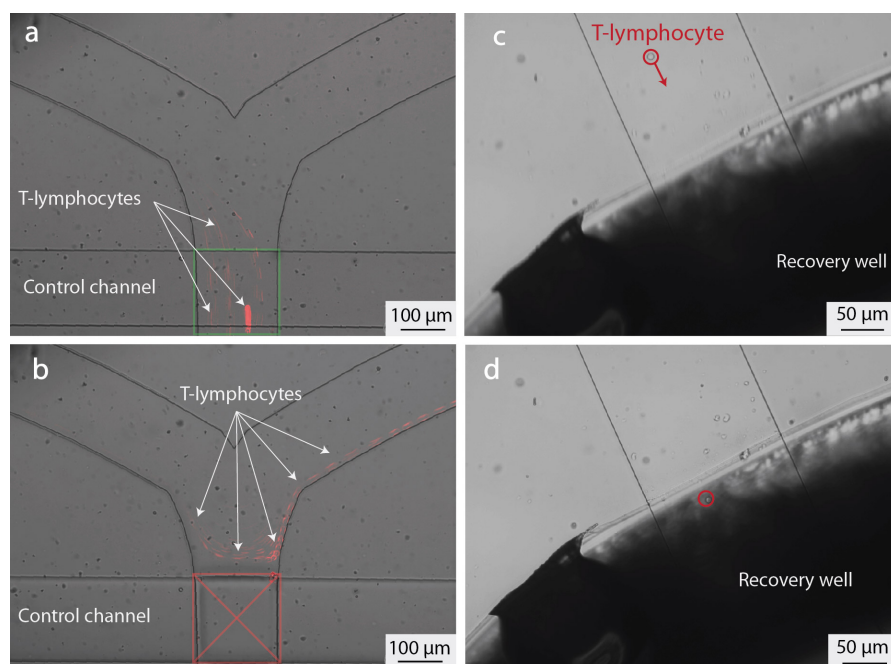


Figure 2.9: Operation of hybrid PDMS/SU-8 valves for cell handling and off-chip recovery (a,b) Operation of a hybrid SU-8/PDMS valve used to control the flow in the microfluidic channel. Trajectories of the lymphocytes in the channel is depicted in red. As SU-8 is stiff, high pressure (3500 mbar) must be exerted on the above PDMS layer in order to close the valve. When the valve is open, all cells are directed towards the main microfluidic channel (a), while closing the valve will prevent them from entering the channel (b). Combining four of those valves enables control of the injection and recovery of cells from the chip. (c,d) A single lymphocyte exiting the chip and entering the recovery channel, where it can be pipetted and further analyzed. This direct recovery in a well prevents the cells from sticking and being lost in outlet pipes.

Following release of a cell our interest stood in the off-chip recovery of this cell for further analysis. To this end our device incorporated the valving system discussed in section 1.3. Our hybrid SU-8/PDMS valves succeeded in guiding the cells throughout the microfluidic channels as shown in figure 2.9a,b. Indeed, the application of a high pressure on the control channel closed the valve sufficiently to stop the passage of cells. However, as the SU-8 fluidic could not deform, the valve was only partially sealed, and a subcellular-sized aperture remained between the SU-8 walls and the PDMS membrane. The residual flow through the valve was used to drive the cells to the recovery well. Figure 2.9c,d show the recovery of a single cell leaving the chip and entering the recovery well from which it can be simply pipetted out.

2.2.3 Trapping and release of beads

The scope of this section is to describe and discuss the layout and performance of a bead-based trapping and release system. We aim at designing a platform that could efficiently trap and maintain against the flow beads of large diameter in order to allow efficient analyte collection. The cleaning of the device upon inversion of the flow in the microfluidic chamber was also investigated.

Description of a single trapping unit

The bead-trapping layout is adapted from a publication of Di Carlo et al. [22], who was among the first to introduce hydrodynamic traps for single particle immobilization. In this publication the trapping site is composed of a 2 μm high opening within a 40 μm high U-shaped PDMS structure located in a microfluidic channel. The integration of a small opening in a wall to create a trap comes with many advantages, namely a low risk of cell damage caused by shear stress and the possibility to pattern very fine restrictions as the molds defining the opening is only 2 μm high [69]. However this comes at the cost of a higher complexity in the microfabrication with the use of 2 molds for the PDMS production. This complexity can be mitigated in our case via the integration of an opening in the middle of the U-shape PDMS structure. As our target particles' size is large the critical size of the molds is not a critical concern. Furthermore, beads can not be harmed by the shear stress, impairing the damaging risk. Figure 2.10 presents SEM pictures of the 50 μm high traps. Traps are arranged in asymmetric rows to ensure an efficient trapping of beads, as a bead avoiding one trap will have a high probability to be captured by the next one encountered downstream. The PDMS pillar placed after the trapping site serves the purpose to clean the device from the beads after use. Indeed, upon inversion of the flow in the chip, the beads will leave their traps but will not be captured by the restriction that are "protected" by the pillar. This novel strategy circumvents a common belief that totally passive trapping devices can not be cleaned and reused. It is of significant importance as reusing the device for several experiment saves some time- and cost-intensive steps.

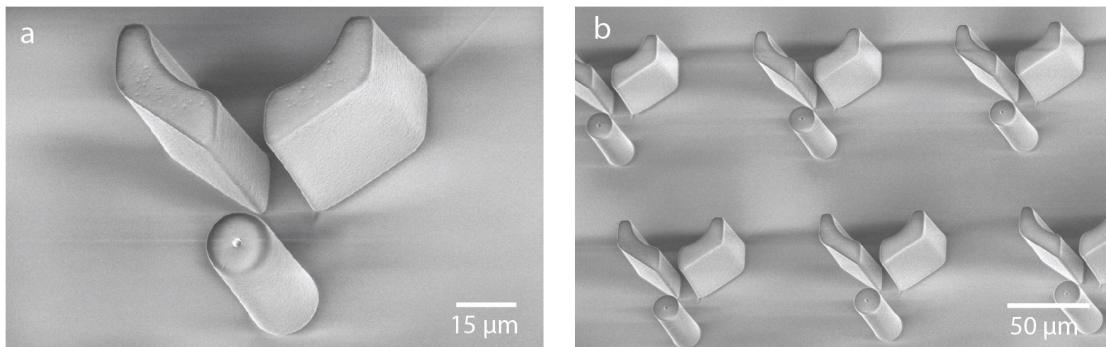


Figure 2.10: **PDMS trap to capture and maintain large beads in a fluidic channel** A single trap (a) is composed of a 50 μm high U-shaped PDMS structure opened in its center and of a "protective" pillar allowing the cleaning of the chip. Traps are arranged in asymmetric rows to achieve a better trapping efficiency.

Results and discussion

20 μm polystyrene beads were resuspended in a solution of Phosphate Buffer Saline (PBS) supplemented with 1% Bovine Serum Albumin (BSA) and injected in the microfluidic channel. The BSA will passivate the surface of the device and prevent unwanted sticking of particles in the system. The trapping efficiency, defined here as the percentage of injected beads immobilized in a trap, was determined to be nearly 100%. Indeed, the high number of traps we implemented on-chip, more than 50 rows of 15 traps, allowed to trap all the beads entering in the chip (Figure 2.11a). Following bead capture, the flow was reversed and all trapping sites could be emptied reliably as illustrated in Figure 2.11b. To the best of our knowledge, this is one of the first device based purely on fluidodynamic effects allowing the release of previously trapped beads. Such release is not as selective as the DEP-actuated release introduced in section 2.2.2, yet the selectivity is not a critical asset in the context of cleaning a chip for resusability.

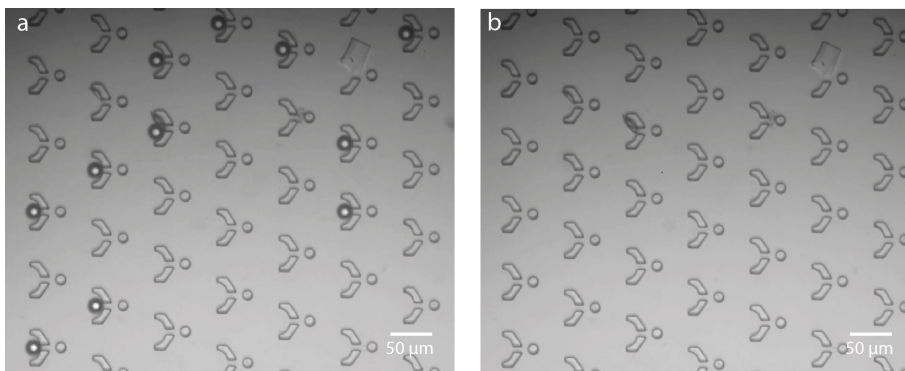


Figure 2.11: **Hydrodynamic trapping and release of beads in a PDMS chamber** Beads can be trapped with a high efficiency in the microfluidic restriction (a) and released upon application of a reverse flow rate (b).

2.3 DEP-based manipulation of beads

The capture of particles via hydrodynamic trapping offers many advantages such as its simplicity, high efficiency and accurate spatial distribution explicated in the previous section. However, it suffers from a poor flexibility in the trapping size of particles. Indeed, the microfluidic restriction will trap all particles above a certain size, without any possibility to tune the trapping properties after fabrication. It is also limited by a non-optimal exposure of particles to analytes in flow. When a particle is captured in the restriction, the flow passing in that area is greatly reduced and consequently the exposure to analyte in the solution. To circumvent such limitations we introduce in this section a method for in-flow trapping and handling based on DEP forces. Such approach allows to maintain a high flow around the particle and to adapt to the size of the particle of interest we want to study by tailoring the applied voltage. The main impact of this method stands in the field of diagnostics, which can benefit from the enhanced exposure to flow for a rapid detection of the target analyte.

2.3.1 Holding beads against the flow via DEP forces

In order to immobilize and then manipulate a particle held against the flow our aim is to counteract the drag force created by the flow on the particle and given in equation 2.5 for a spherical particle such as our polystyrene bead:

$$f_{drag} = 6\pi\eta RV_0 \quad (2.5)$$

Where η is the fluid viscosity, R the particle radius and V_0 the fluid constant velocity.

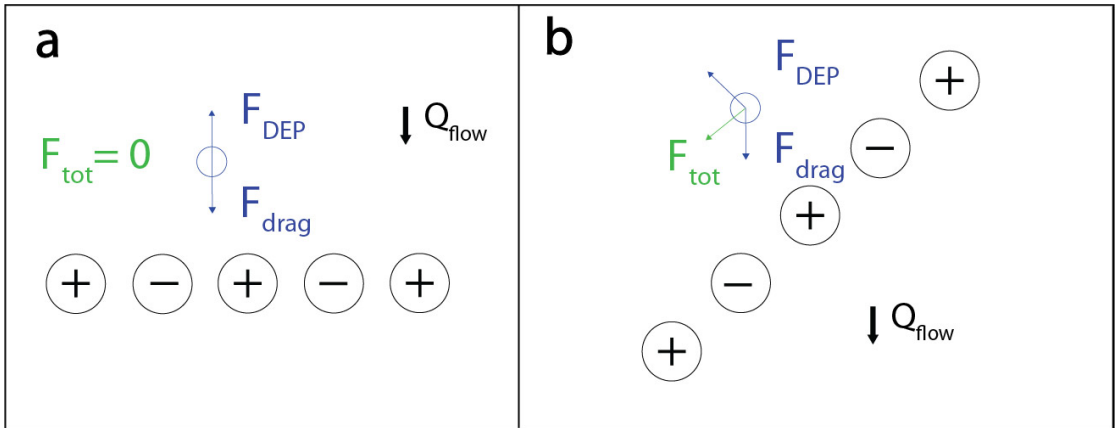


Figure 2.12: **Effects of drag and DEP forces on a bead placed in a microfluidic channel** Illustration of the net force experienced when a bead approaches a horizontal or a diagonal electrodes' line, respectively resulting in the bead immobilization (a) or directed "surfing" along the electric field.

The force provided by the liquid has to be compensated by the DEP force given in equation 2.2. To do so we incorporated an horizontal line of 3D electrodes shown in figure 2.12a. Since this line is normal to the flow, the negative DEP force experienced by the particle is directed against the drag force f_{drag} . Provided that the DEP force is sufficient to compensate for the drag force, the beads are immobilized upstream in the vicinity of the electrodes' line. Furthermore, if the row of electrodes is placed at a specific angle with respect to the flow, the DEP force will not be directed against the drag force and we will observe a net force heading the bead in a specific direction in a phenomenon we refer to as "DEP surfing" (figure 2.12b).

The horizontal lines maintain small cluster of beads against the flow and ensure a continuous flow of analyte and reagents, thus allowing their binding to the beads' surface. (figure 2.13a). Beads following the surfing approach, however, are displaced along the diagonal lines and end up accumulating in a specific region (figure 2.13b). Such aggregation is suitable in the diagnosis context as the signal of a single bead is not sufficient for a reliable quantification and the beads need to be clustered prior to signal acquisition [58].

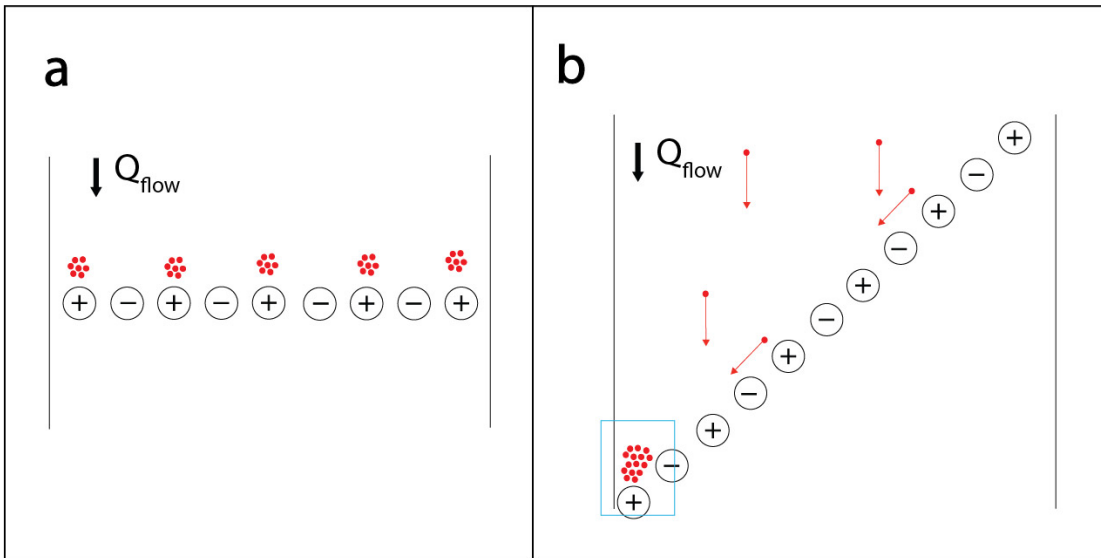


Figure 2.13: DEP as a tool for on-chip incubation and accumulation of beads Extending the single bead approach presented above to multiple beads, one can obtain either small clusters for on-chip incubation close to horizontal lines (a) or large clusters in the regions where all the surfing beads are immobilized against the microfluidic channel wall (b), indicated by a blue rectangle. Beads are depicted in red.

Equation 2.2 establishes the dependence between the size of the beads and the DEP force they will experience. Each line of electrodes can generate a different DEP force and can consequently trap and displace specific beads depending on their size. In this way, beads of different sizes can be driven to distinct regions on the chip (Figure 2.14). If beads of different sizes are functionalized with different antibodies, our approach allows to perform a multianalyte analysis with a single fluorescent channel.

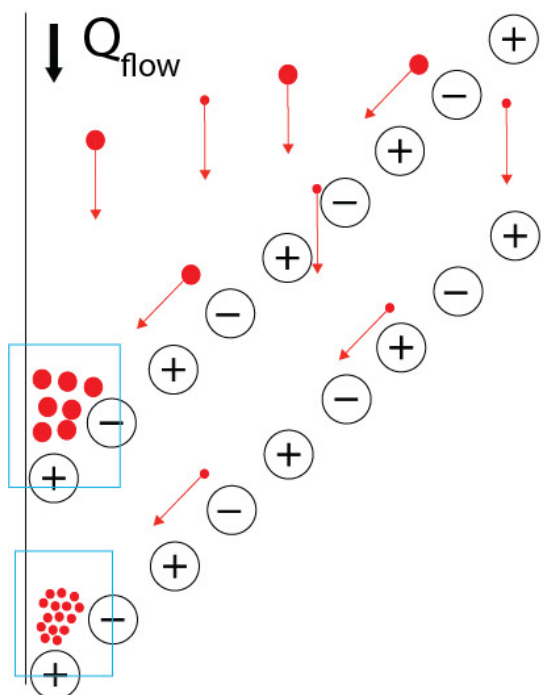


Figure 2.14: **DEP discrimination of different-sized beads** Illustration of the multianalyte detection capabilities of our platform. Through the application of different electrical potentials on diagonal lines, we can achieve the clustering of beads of different sizes in separate locations.

2.3.2 Device layout

The methods presented above were implemented in a microfluidic channel in order to carry out both on-chip incubation and clustering of microbeads. The device layout is described in figure 2.15. It consists of a single channel with two inlets and a single outlet featuring linear arrangements of three-dimensional electrodes, patterned to obtain three incubation lines (horizontal) and three accumulation lines (diagonal). We chose to integrate three of each type of lines to have the opportunity to test the size-based separation but also to have at our disposal extra lines in case one of them appeared to be defective. Both inlets and outlets feature filters preventing the introduction of excessive dust.

2.3.3 Trapping results

The investigation of the trapping performance was carried through the injection of $6\ \mu\text{m}$ polystyrene beads in the device. The chip was primed with buffer solution (fetal bovine serum, FBS, diluted five times in deionized water) in order to prevent unspecific bindings to the channel walls. The beads were efficiently captured against a flow rate up to $3\ \mu\text{L}/\text{min}$ as shown in figure 2.16. The random arrival of beads on the horizontal incubation lines ensures the creation of small clusters in which the beads can move around and capture the analyte of interest. The optimal frequency for DEP actuation was determined experimentally and found

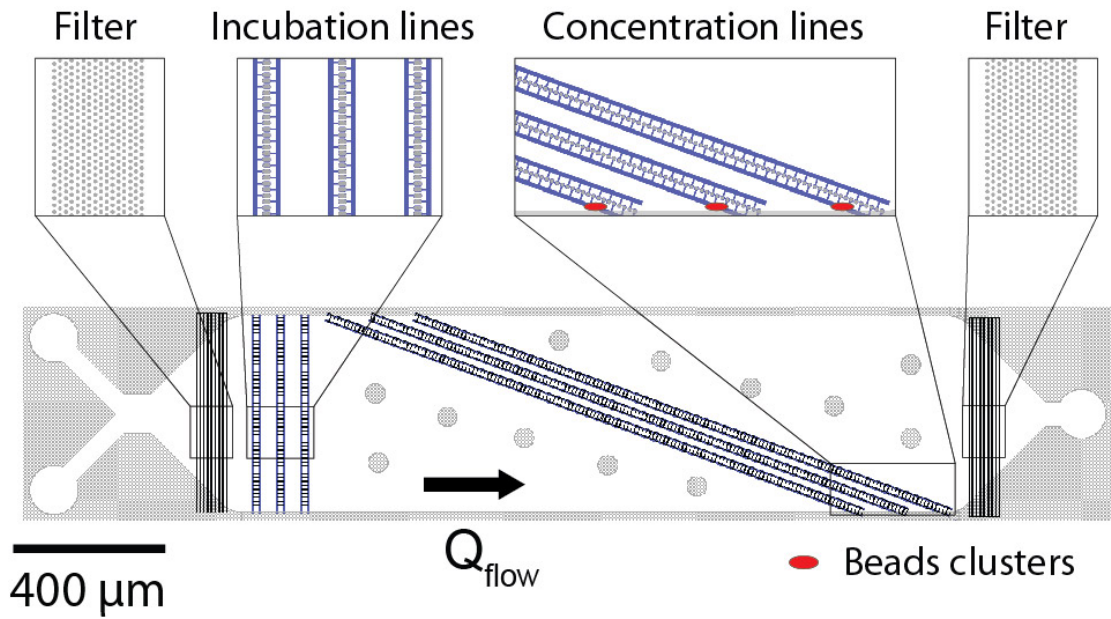


Figure 2.15: **Layout of the platform for beads incubation and clustering** Presentation of the chip layout. Beads and reagents can be successively injected through the two inlets visible on the left. The device consists of three incubation lines upstream and three concentration lines downstream, at the end of which the beads are accumulated in clusters (shown here in red).

to be 1 MHz. Voltages ranging from 5 Vpp to 20 Vpp achieved a good trapping of beads, with as expected a better capture at higher voltages.

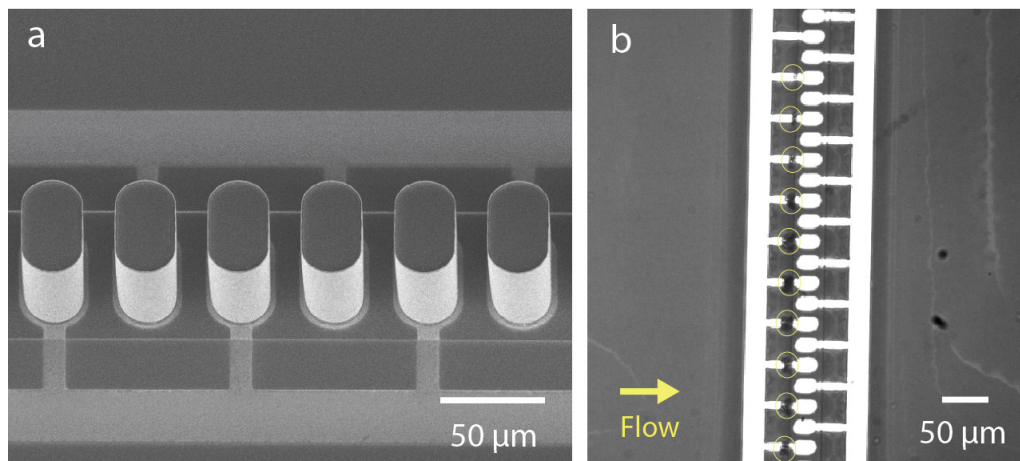


Figure 2.16: **Results of the DEP-based on-chip capture of beads** The incubation lines consisting in 3D electrodes standing in a microfluidic channel (a) can successfully stop the beads in flow in order to form small clusters circled in yellow (b).

2.3.4 Surfing results

The study of the "surfing" phenomenon was carried out using the same protocol as for the incubation lines testing. We observed a deflection of the beads as they came close to the diagonal lines. They "surfed" in-flow along the diagonal concentration lines until they reached a region where they were trapped against the microfluidic wall as shown in figure 2.17. Interestingly, provided the same voltage, the beads could be deflected at higher flow-rates than the maximal ones determined for immobilization on the incubation lines. Indeed, the force required to counterbalance the drag flow and immobilize the beads is greater than the one needed to only deflect the beads. The surfing phenomena occurs over the entire length of the lines, consequently a single defect in one of the pillars can result in drastically reduced performance of the system. This underlines the critical importance of achieving high yield in the fabrication process described in the first chapter of the thesis section 1.2.1. The aforementioned clusters can be nicely disassembled by turning off the voltage on the surfing lines, resulting in a efficient cleaning of the chip and the possibility to reuse it. The application of different voltages on the surfing lines permitted to carry out a size-based separation of beads as predicted in the previous section, beads of $2\ \mu\text{m}$ and $6\ \mu\text{m}$ were successfully separated and clustered in different regions of the microfluidic channel in order to carry out a multianalyte detection thoroughly discussed in the chapter 3 section 3.1.5.

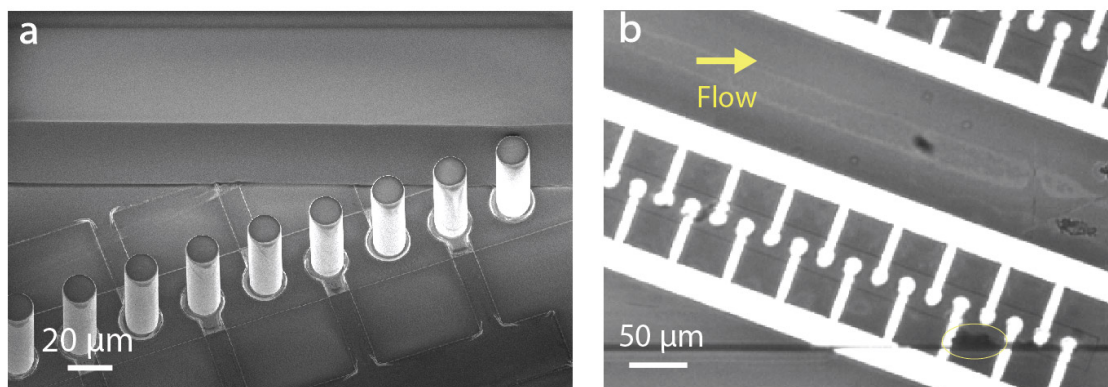


Figure 2.17: **DEP surfing of beads and accumulation against the channel sidewall** The surfing lines are crossing the entire width of the channel and ending up very close the SU-8 microchannels walls (a). Beads can travel along those lines and finally arrive in the wall region where they form large clusters such as the one circled in yellow (b).

2.4 Summary and conclusion

In this chapter we present and discuss several techniques for immobilization and exposure to a flow of analytes of particles within a microfluidic channel, either based on the use on mechanical restrictions or DEP manipulation. Both methods exhibit some limitations, for instance hydrodynamic trapping can not easily cluster particles and DEP actuation with 3D electrodes requires the use of advanced microfabrication methods. However, each approach

Chapter 2. Microparticle handling and reversible trapping in microfluidic channels

matches a specific target application that will be discussed over the course of the next chapters, namely the diagnostics of acute conditions with DEP-manipulated beads, the fast screening of biomarkers with beads trapped in mechanical restriction and the study of the impact of DEP forces on cells in our single-cell capture and recovery platform.

3 Multimarker diagnostic approaches based on microbeads

Disclaimer: The work presented in this chapter is partially adapted from the following articles:

Thiriet, P.-E.; Medagoda, D.; Porro, G.; Guiducci, C. Rapid Multianalyte Microfluidic Homogeneous Immunoassay on Electrokinetically Driven Beads., *Biosensors*, 2020.

My contribution: Conceptualization, Methodology, Validation, Formal Analysis, Investigation, Data Curation Writing and Editing.

The current Covid-19 outbreak highlighted in a dramatic manner the need of sensitive, yet affordable, diagnostic tools. In such a pandemic scenario massive testing appeared to be an incredibly valuable solution to prevent the spread of the disease and to identify even asymptomatic patients [70]. The two main approaches implemented for the detection of the virus were gene amplification via Polymerase Chain Reaction (PCR) and lateral flow assays (LFA), suitable for rapid testing. While PCR test are very robust and sensitive, they rely on bulky equipment and expensive reagents [71]. On the other hand, LFA are very low-cost and user-friendly, however they suffer from a limited sensitivity and accuracy [71]. Microfluidics could help solve this paradoxical situation by providing a rapid, sensitive and affordable detection of species with a compact device [72]. The small dimensions of microfluidic channels lead to high surface-to-volume ratio, which fastens analyte collection and limit the amount of reagents required to carry out assays. Furthermore, diagnostics tests are not always performed in the urge of a pandemic scenario and most of the tests are actually carried out in the context of health status monitoring or chronic conditions investigation, such as in the framework of cancer detection and treatment. When a diagnostic is conducted without a precise idea of its outcome, testing a large panel of biomarkers increases the chance of accurate diagnosis [73]. However, testing a wide range of species comes at the price of a higher complexity and cost. The aim of this chapter is to present two devices targeting the detection of acute conditions and

a highly multiplexed biomarkers detection, respectively. Section 3.1 presents and discusses a novel microfluidic point-of-care platform for the rapid detection of acute kidney injury. Section 3.2 introduces a new approach for fast and versatile detection of multiple biomarkers combining immunoassays with DNA barcodes.

3.1 Point-of-care system or Acute Kidney Injury detection

3.1.1 Context

Biosensors

The quantification of biological species is of tremendous importance for every branch of biology, from diagnostics [74] to new drugs development [75], and from single-cell analysis [43] to metabolic pathways understanding [76]. Biosensors convert molecular recognition of an analyte into a quantifiable signal via a transducer. They are often characterized by a standard curve that presents the measured signal as function of the concentration of analyte in the sample [77] (figure 3.1). Such curve appears usually as sigmoidal, due to saturation phenomena at high concentrations and unspecific binding at low concentrations. Biosensors are commonly classified in two general categories: label-free assays and label-based assays. Label-free assays, among which surface plasmon resonance [78] is an eminent example, directly sense a change of signal due to the interaction of the analyte and the sensing surface while label-based assays employ biomolecules as mediators to capture the analyte in the sample [79], resulting in a more specific and robust detection of analyte. The most well-known example of biosensors are immunoassays, that had a tremendous impact on the field of diagnosis, with the introduction of the first pregnancy test in the seventies [80] and the recent use of antigenic test in the context of the coronavirus outbreak [81].

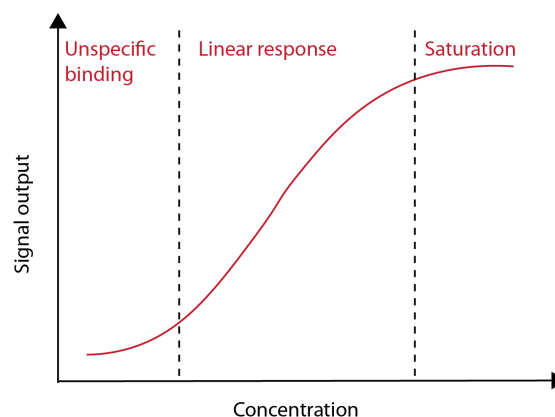


Figure 3.1: **Typical calibration curve of a biosensor** The calibration curve plots the measured signal as function of the target analyte concentration. It commonly presents a sigmoidal shape exhibiting three different domains: unspecific binding regime for low concentration, linear regime in what the dynamic range domain and saturation at high concentration since all the binding sites are occupied.

Immunoassays are biological techniques relying on the interaction of an antigen (analyte) and an antibody for the quantification of the analyte of interest. A wide variety of formats have been proposed and implemented to adapt to reagents available and to the desired dynamic range [82]. The two most popular formats are sandwich assays and competitive assays. The sandwich configuration relies on two antibodies that will bind to different epitopes of the analyte. The capture antibody is first immobilized on a surface before exposure to the antigen and subsequent exposure to a second antibody, the detection antibody. The antigen is thus "sandwiched" between the two antibodies as shown in figure 3.2 left. The functionalization of the detection antibody determines the output readout signal of the assay, it can be either fluorophores in case of fluorescence-based assays [58], gold nanoparticles for optical assays [83], or nothing for enzyme-linked immunosorbent assays (ELISA) [84]. Such tests are among the most sensitive and reliable, nonetheless they are not suitable for the detection of small antigens, as they require binding sites for both capture and detection antibodies. Competitive binding assays, which are based on the competition of labeled and unlabeled ligands for the access of a limited number of binding sites, can overcome this limitation as they require only one antibody. They can thus perform the detection of small analytes or species that do not have an couple of antibodies validated in a sandwich configuration. In such assay, a determined amount of labeled ligand and a variable amount of unlabeled ligand (the analyte) are incubated together with the antibodies (figure 3.2). The quantity of bound labeled analytes is a function of the total concentration of labeled and unlabeled analytes following the mass transport laws.

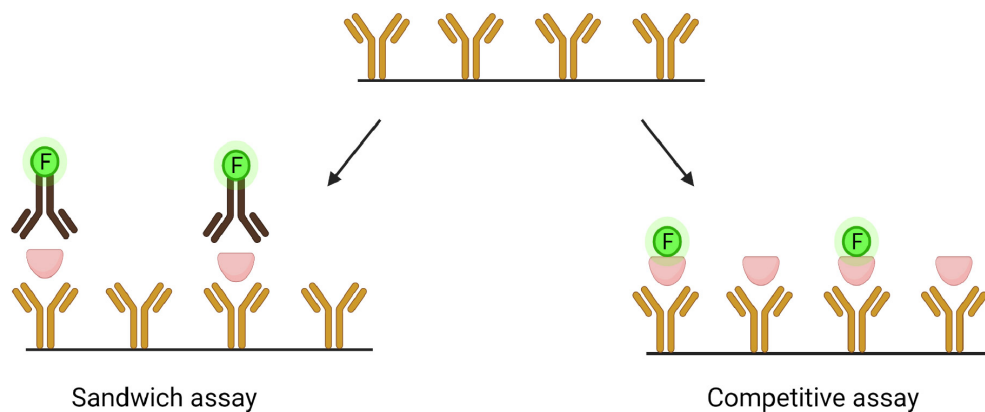


Figure 3.2: **Illustration of two different formats of immunoassays** Starting from the same antibody immobilized on the surface of a biosensor the analyte detection can be performed via a sandwich (left) or competitive (right) assay.

Immunoassays on beads

Bead-based immunoassays play a central role in the microfluidic diagnosis field as a consequence of the benefits they offer [85]. While planar assays takes place at the bottom of channels, bead-based assays use the third dimension to offer large surface to volume ratios

and enhanced collection of analytes in-flow as thoroughly discussed in the introduction of this thesis. Thus, 1 g of 100 nm diameter beads provide a total surface area of 60 m^2 [86]. This results in an efficient binding of targets and ultimately in a high sensitivity of the sensing system. Another asset of microbeads resides in their ease of manipulation within a microfluidic channel. Upon injection they can be guided throughout the chip thanks to pressure-driven flow [87], magnetic forces [11] or electrokinetics forces [88]. If the beads are functionalized prior to their introduction in the microfluidic device there is no need to modify the surface of microfluidic channels with capture ligands. This greatly simplify the packaging process of the device, as microfluidic channels functionalized with proteins are very sensitive to increase in temperature or exposure to chemical compounds, making the sealing of the device challenging. Finally, a large variety of surface modifications are available for beads, involving for instance biotin, amine-groups or thiol-chemistry [89], granting a high variety in the platform applications. Indeed, one system developed for the detection of a specific marker could easily be adapted for the detection of another molecule via a modification of the capture antibodies carried on the bead's surface.

Numerous platforms have successfully combined the use of microfluidic and bead-based assays for medical diagnosis applications. For instance, Cui et al. [90] carried out an immunoassay on beads immobilized in small PDMS chambers in order to detect low concentration of cytokines in patient serum. Yu et al. [91] developed a bead-based platform for the simultaneous detection of several breast cancer markers. The two examples above are relying on a bulky set-up to perform the detection, nonetheless beads also appear very suitable for the diagnosis of acute conditions in the context of compact point-of-care systems.

Point-of-care systems

Point-of-care diagnostics (PoC) are essential to provide rapid diagnostic tools in remote configurations [92, 93]. Three main applications stand for such platforms: Home testing for minor conditions, testing for diseases in low income countries [58] and acute conditions in intensive care units or ambulances [94]. The success of point-of-care systems in such contexts relies on various requirements such as a low sample volume, little to none sample preparation and short total analysis time. As they permit a rapid and reliable detection of acute conditions, PoC systems have the potential to outperform the current detection techniques implemented for numerous conditions, from cardiac strokes [95] to sepsis [96]. Despite a complex implementation in the actual coronavirus crisis [97], point-of-care systems have a bright future in the era of connected medicine and big data.

The benefits associated with the use of bead-based immunoassays make them ideal candidates for the development of PoC devices. However, as single bead does not produce high output signals, the gathering of beads into large clusters is required to obtain a sufficient readout signal. The spatial handling of beads is commonly performed either through magnetic forces [11] or by means of mechanical restrictions [87]. These approaches suffer from limitations hindering their use in a PoC devices, namely, a difficult integration into a portable platform for

magnetic devices and clogging issues for mechanical systems. The DEP-based manipulation of beads via the generation of electrical fields gradient presented in chapter 2 section 2.3 appears as a promising solution for beads' manipulation in a compact and highly integrated system.

Acute kidney injury

The selection of the condition to target in this section has been carried out after careful analysis of the need for rapid diagnosis and the availability of antibodies against potential biomarkers. We found a very convincing case in acute kidney injury (AKI). AKI refers to a rapid loss of kidney functions, due to nephrotic or ischemic causes [98]. It is a symptom that can be caused by a large range of disorders and consequently is frequently encountered in intensive care units. In developed countries, AKI occurs in 20% of hospitalized adult patients and 25% of pediatric patients receiving intensive care [99], including patients infected with the recent coronavirus [100]. One of the consequences of AKI is the disruption of homeostasis, inducing an accumulation of waste products normally removed by the kidneys, which can lead to severe damages throughout the body. If treated quickly, the effects of AKI are reversible, notably through fluid resuscitation and medication [101] but they can lead to death of the patient without proper intervention.

Currently, AKI is diagnosed through monitoring of the patient's urine output volume and measurement of the level of serum creatinine in blood [101]. Creatinine quantification suffers from diverse limitations, for instance interference with drugs such as antiretroviral drugs [102], variations in basal creatinine levels between patients, and, most importantly, a long delay (36 to 48 h) between the occurrence of AKI and a detectable increase in serum creatinine concentration [103]. This large window between AKI occurrence and detection leaves a long period in which the patient's kidney might suffer irreversible damage. Consequently, there is an urge to implement novel assays with markers of AKI that spikes earlier in the blood. Numerous potential alternative AKI biomarkers are currently investigated by research groups worldwide [104]. Here we focused on two of the most promising ones, namely Cystatin C and Neutrophil Gelatinase-Associated Lipocalin (NGAL). Cystatin C has been so far the most investigated of the two. It is a molecule that can be found in all tissues and is produced by the kidneys. This marker's levels also appear less dependent on gender, age, muscular mass and liver functions than serum creatinine [105]. It was proven to be an accurate for AKI detection in very diverse situations and it spikes in the serum noticeably before serum creatinine [106]. While there is not a clear consensus on the precise threshold for diagnosis, a Cystatin C concentration above 1 $\mu\text{g/mL}$ seems to spike 24 hours after kidney injury [107]. NGAL is a protein that can be found in neutrophils and some epithelia including renal tubules. As AKI damages the kidneys' epithelium, such disorder induces an increase of NGAL concentration in serum within four hours [107, 108]. The threshold for AKI detection based on NGAL monitoring varies from 25 $\mu\text{g/mL}$ [98] to 200 $\mu\text{g/mL}$ [107] depending on the patient. The absence of temporal overlap for the markers makes them very suitable for a combined diagnosis over a large timespan, thus

reducing the risk of false negatives.

The critical requirements of timeliness in the diagnosis of AKI call for fast analytical devices to perform the analysis of the relevant biomarkers such as NGAL and Cystatin C directly within intensive care units or emergency facilities. The detection of such markers in clinical settings relies on immunoassays carried out by means of bulky analyzers, such as Abbot Architect i1000SR and c4000, used, respectively, for the quantification of NGAL and Cystatin C. Commercial point-of-care (PoC) systems for the individual detection of these targets are also available on the market, namely, the Triage® system of Alere Inc. for the detection of NGAL through a lateral flow assay [109] and the Cube® of Eurolyser for Cystatin C levels' quantification. None of the available platforms allows the simultaneous quantification of Cystatin C and NGAL in a point-of-care settings. The aim of the next section is then to distinguish patients presenting a early AKI or late AKI via a concomitant detection of their Cystatin C/NGAL levels. To this end we rely on an immunoassay approach that could be engineered into a point-of-care device.

3.1.2 System layout and operation principle

The aim of this section is to present how we could employ the DEP-actuated platform presented in section 2.3 for the rapid diagnosis of AKI. We will first describe the design of the immunoassays and then focus on the detailed operation of the microfluidic system.

Antibodies' conjugation to beads and to detection fluorophores

Polystyrene beads covalently coated in Streptavidin (Spherotec Inc.) were purchased at sizes of 2- μ m diameter (binding capacity = 0.42 nmol/mg) and 6 μ m diameter (binding capacity = 0.14 nmol/mg). The 2- μ m beads were incubated with biotinylated Cystatin C monoclonal capture antibodies (Cyst13-biotinylated, Novus Biologicals) and the 6 μ m-beads were incubated with biotinylated NGAL polyclonal capture antibodies (Human Lipocalin-2/NGAL-biotinylated antibody BAF1757, R and D Systems, UK) for at least four hours. They were then resuspended and incubated for 1–2 h in 1% bovine serum albumin (BSA, Sigma Aldrich, St. Louis, MO, USA) in 0.1 M phosphate buffer (PB, Sigma Aldrich, St. Louis, MO, USA) for blocking. After blocking, beads were washed four times through a procedure of centrifugation, supernatant removal, and resuspension in a solution of 0.05% Tween-20 (Millipore, Burlington, MA, USA) in 0.1 M PB. After the final washing steps, beads were stored in 0.1 M PB at 4 °C. Both antigens for Cystatin C (Human Recombinant Cystatin C, Novus Biologicals, UK) and NGAL (Human Lipocalin-2/NGAL, CE, R and D Systems, UK) were acquired and used as is. Monoclonal detection antibodies for Cystatin C (Cyst24-Dylight 550, Novus Biologicals, UK) were purchased with a Dylight 550 fluorophore, while monoclonal detection antibodies for NGAL (Human Lipocalin-2/NGAL Antibody MAB17571R, R and D Systems, UK) were labeled with a fluorophore using a Lightning-Link Rapid Alexa Fluor 647 antibody labeling kit (Expedeon, San Diego, CA, USA). Prior to experiments, antigen and detection antibodies were incubated together for 15 min in

fetal bovine serum (FBS, Sigma Aldrich, St. Louis, MO, USA) diluted five times in MilliQ water.

Operation of the microfluidic chip

Bead-based sandwich immunoassays were performed on our platform as illustrated in Figure 3.3. The fluorescently labeled detection antibodies (dAbs) were spiked in the sample prior to injection in the chip. Before undergoing injections of reagents solutions, the chip was primed with buffer solution (fetal bovine serum, FBS, diluted five times in deionized water) in order to prevent unspecific bindings to the channel walls. (1) After priming, beads functionalized with capture antibodies (cAbs) were injected in the device and held in suspended small clusters (few tens of beads) upstream of the incubation lines, as illustrated in step 1 in Figure 3.3. The number of captured beads was controlled through visual inspection. During this phase, the microbeads–cAbs solution, 10 μL 0.5% (w/v) in 1 mL of diluted FBS, was delivered from one inlet at 2 $\mu\text{L}/\text{min}$, the maximal flow that could be applied without beads escaping the incubation region, while the incubation line exerted a holding force (20 Vpp, 1 MHz). The obtained small beads' aggregates were spatially confined by the DEP force, while kept in slight agitation by the flow: This turbulent motion favors the convective transport of target molecules. (2) After a sufficient number of beads was collected, the beads–cAbs solution flow was stopped and the solution of antigen–dAbs complexes was immediately dispensed from the other inlet at 2 $\mu\text{L}/\text{min}$. The antigen–dAbs solution was flushed in the chip for 15 min. During this incubation step on-chip, the binding between the analyte–dAbs and the cAbs led to the formation of the complete sandwich assay on the beads' surface.

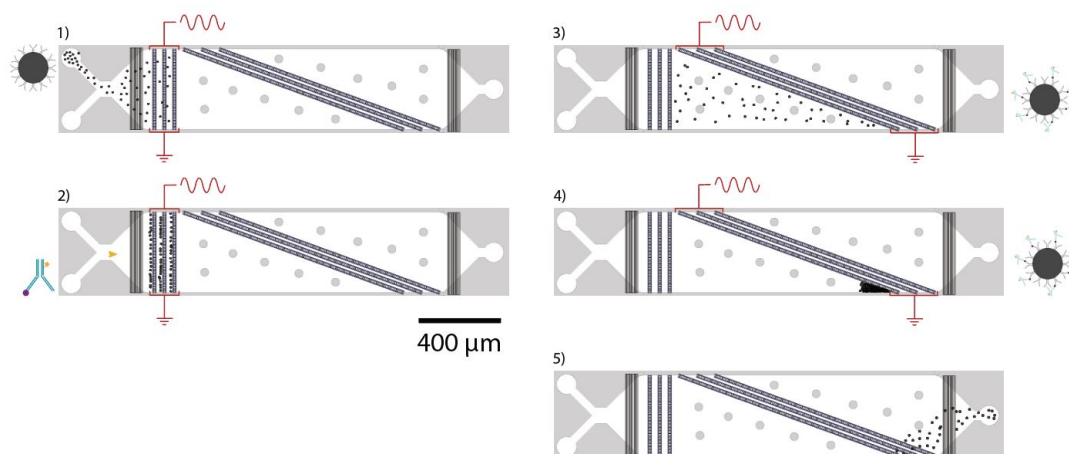


Figure 3.3: Presentation of the successive steps performed on-chip to operate the platform
The following steps are sequentially carried out: (1) beads' loading, (2) incubation with detection antibodies and (3) release from the incubation line, (4) clustering in the concentration region, and (5) discarding through the outlet. For the sake of clarity, the species bound to the beads and the electrically activated arrays of electrodes are indicated for each step.

(3) After incubation, the beads were released by turning off the electrical signal. Concomitantly, the concentration line was activated (20 Vpp, 1 MHz) and the beads were led to “surf” in-flow along the diagonal accumulation lines until they reached a region where they were trapped against the microfluidic wall. (4) The beads carrying the sandwich assays were, hence, accumulated to enhance the total fluorescence signal. We noticed that the so-obtained clusters, imaged in CY5 fluorescence channel at 5000 ms exposure, presented a uniform intensity profile per μm^2 provided that their size was equal or larger than $50 \mu\text{m}^2$, that would translate in about 100 beads. (5) Finally, the beads were released from this accumulation region by deactivation of the electrodes’ line.

3.1.3 Real time monitoring of on-chip incubation

The first results obtained with the microfluidic system upon performing an immunoassay was the real-time observation of the fluorescent signal on the incubation lines. While not used for a quantification of the fluorescence levels, a step that was performed after beads accumulation, it provided interesting insights regarding the binding between NGAL and the capture Abs.

The on-chip incubation of antibody-functionalized beads with antigens and detection antibodies took place on dedicated horizontal incubation lines. We maintained beads decorated with cAbs against the flow and concentrated them in small clusters of about 10 to 20 beads. Significant variability was observed in the size of the growing clusters, reflecting inhomogeneities in the flow lines within the microfluidic channel. Such inhomogeneities were mainly caused by microfabrication defects or debris accumulation at the entrance of the chip. Then, a solution containing the dAb–NGAL complexes was injected at a flow rate of $2 \mu\text{L}/\text{min}$ for 15 min. The binding of the dAb–NGAL complexes to the cAb-decorated beads was observed and quantified in real time by fluorescence measurements of the CY5 channel (Figure 3.4).

Figure 3.4a illustrates the dependence of measured fluorescence intensity of the small clusters on the concentration of NGAL in the injected solution. Such behavior could be quantified with a minute-range resolution, as shown in Figure 3.4b. A steady increase of fluorescence signal could be recorded after 15 min upon injection of NGAL–dAbs complexes at concentrations in the range of 0.5–100 ng/mL. Interestingly, none of the plots were reaching a plateau, suggesting the persistence of a transient binding regime. Different concentrations corresponded to similar fluorescent intensities, e.g., 5 ng/mL and 10 ng/mL. Thus, they might have appeared perilous to resolve due to a significant standard deviation. This variability in the clusters’ fluorescent signal was caused by the varying size of the small clusters formed near the incubation lines. Nonetheless, the purpose of the horizontal incubation lines was to allow for incubation to happen in the most favorable conditions and not to enhance the readout of the fluorescence intensity. This step took place in the accumulation regions.

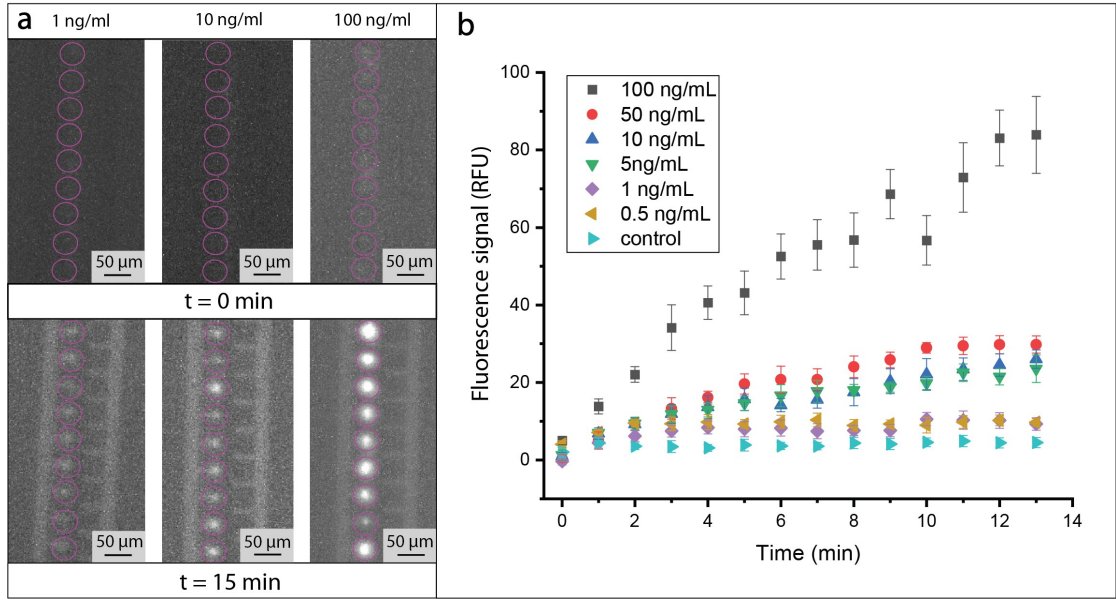


Figure 3.4: On-chip incubation of Neutrophil Gelatinase-Associated Lipocalin (NGAL) biomarker. (a) Observation of the small beads' clusters (circled in pink) before and after 15 min of incubation. The fluorescence signal arose from the binding of dAb-NGAL complex to cAb-decorated beads dielectrically trapped in the regions upstream to the electrode line. Three NGAL concentrations were injected in separate experiments, namely, 1 ng/mL, 10 ng/mL, and 100 ng/mL. (b) Fluorescence signal as a function of the incubation time for different NGAL concentrations. After 15 min all concentrations provided a signal greater than the control experiment, consisting of an injection of a solution in absence of NGAL molecules. The error bars were obtained by measuring the fluorescent signal from 10 clusters.

We designed the DEP holding action at the horizontal incubation lines in a way that the size of the clusters would be maintained sufficiently small (less than 20 beads) to keep the accumulated beads in slight agitation. This approach allows for uniform binding of analytes in-flow and access to the whole surface offered by the beads. In fact, in the case of large clusters, the reagents would be depleted at the downstream portion of the aggregate, an issue that was observed in previous works [58]. This limitation justifies the creation of two separate lines for incubation and accumulation of beads.

Moreover, previous approaches employing DEP force to immobilize beads and expose them to reagents relied on the use of planar electrodes to generate electric fields [110]. This approach relies on a simple fabrication process but leads to the creation of high electrokinetic forces only in close proximity to the chip's surface that features the electrodes. Consequently, as we moved toward the opposite side of the channel, the DEP force experienced by a bead decreased. Vertical electrodes employed in our device, instead, generates a homogeneous electrical field over the entire channel height, ensuring that all the beads entering the incubation region experiences the same DEP force. The height of the channel was then no longer limited and could be substantially increased, to 50 μ m in this device and possibly larger, as only the

microfabrication process dictates the extension of the microchannel height. Extending the height of the channel helped us increase the reagent flow rate in the microfluidic chamber by a factor of 10 or more compared to similar detection platforms [58, 110], improving the collection of analytes by a factor 2 in the case of high Peclet number Pe_H and Pe_S (see introduction).

Another benefit deriving from the three-dimensional electrodes employed to generate DEP forces is the use of minimally diluted solutions. Currently, as DEP forces are weakened in high ionic strength solutions [53], most DEP-based microfluidic platforms are forced to operate in extremely diluted (low ionic force) solutions, thus drastically limiting the actual detection capabilities of their systems due to the consequent dilution of the analytes' concentration [110]. Indeed, diluting the sample of interest by a large factor will consequently reduce the output signal. In comparison, our device successfully performed beads' collection and analyte binding in an only 5× diluted serum, a dilution factor commonly found in commercial biomarker assays [96]. A slight dilution has proven to be even suitable for biomarker analysis, as it reduces matrix effect while maintaining favorable binding conditions [111].

Furthermore, the integration of the incubation step on-chip appears as a key milestone in the process of embedding our technology in a point-of-care device. In fact, it would limit the variance and errors in the concentration readout that might derive from additional external manipulations [112].

3.1.4 On-chip incubation vs Off-chip incubation

The step directly following on-chip incubation is the accumulation of beads in dedicated areas, in order to obtain a larger signal and, thus, increase the system sensitivity. This section aims to assess the impact of carrying out beads' incubation and aggregation in our microfluidic system. To this end we compare our approach both to an off-chip reagent incubation and to the detection of the signal from single beads as illustrated in Figure 3.5.

Beads decorated with NGAL cAbs were incubated either on-chip on the horizontal incubation lines with the antigen-dAbs complex, as described in section 3.1.2, or off-chip, by placing the Eppendorf containing the beads and the complexes in a rotating mixer. The obtained beads were then either clustered on-chip, as shown in Figure 3.6, or observed sparsely on a microscope slide, and the corresponding fluorescent signal was acquired and plotted, as in Figure 3.7.

The comparison between plots 1 and 2 of Figure 3.7 reveals the impact of measuring the fluorescence signal of the microbeads in the accumulation regions on-chip vs. measuring the fluorescence of single beads on plates. In fact, in both cases, the prior incubation of beads with the analyte and dAb was performed identically off-chip in vials. We observed a signal increase of 3.5-fold in the case of beads concentrated in specific locations on the chip, demonstrating the validity of our approach to enhance the signal by locally increasing beads' density to get




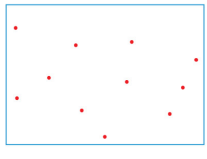
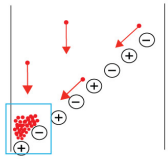
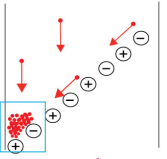
	Experiment name		
Step	1	2	3
Incubation	 Off-chip	 Off-chip	 On-chip
Readout	 Off-chip	 On-chip	 On-chip

Figure 3.5: **Experimental protocol implemented to separately assess the impact on the output signal of our platform of both on-chip incubation and accumulation of beads** Experimental protocol implemented to separately assess the impact on the output signal of our platform of both on-chip incubation and accumulation of beads.

a larger signal. Such amplification allows the detection of 1 ng/mL NGAL concentration in 5-fold diluted FBS, while this concentration could not be resolved by observing the fluorescent intensity of single beads. Common approaches for beads’ accumulation involve the application of magnetic forces [113, 114] or DEP forces [58]. The increase in signal that we found to be a consequence of the beads’ accumulation is in line with what has been previously reported in literature [113].

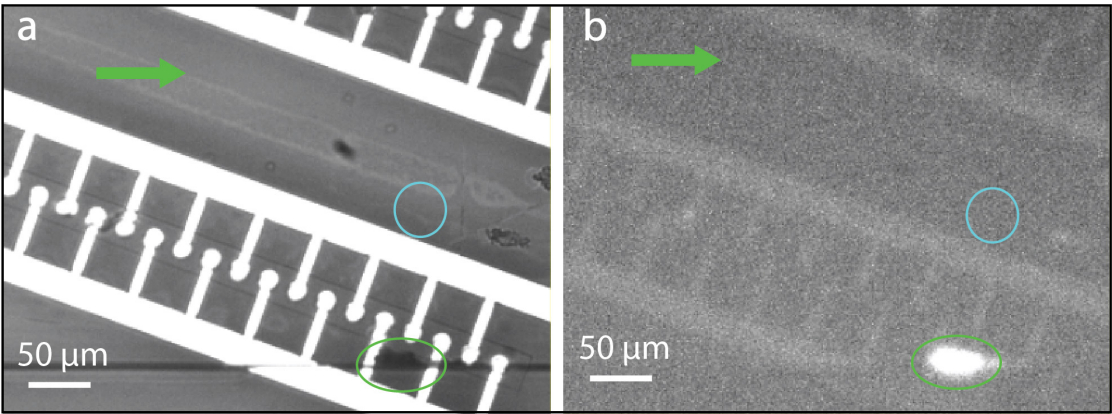


Figure 3.6: **Images of beads clustered in the accumulation area** (a,b) Brightfield (a) and fluorescence (b) images of beads clustered after 15 min of incubation (NGAL concentration of 100 ng/mL) and concentration steps. A bright fluorescent signal is clearly visible in the accumulation region circled in green. The blue circle indicates the region chosen as neighboring background for the normalization of the cluster signal.

On the other hand, the influence of incubation conditions on the attained signal could be analyzed comparing plots 2 and 3 of Figure 3.7. In this case, the clustering of beads was carried out in the microfluidic platform in both experiments, while the incubation was performed either on-chip or off-chip. On-chip incubated beads reached the same level of antigen binding as the off-chip incubated beads. This demonstrates that the on-chip process matches the performance of a standard incubation in turbulent regime.

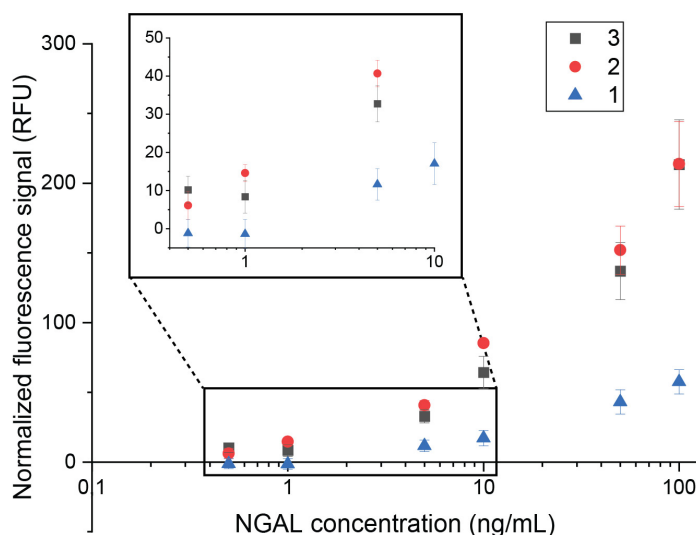


Figure 3.7: Calibration curves for on-chip incubation and clustering performance assessment Calibration curves obtained for the aforementioned experiments. The measured relative fluorescence signal is plotted as a function of the NGAL concentration employed for incubation. Plot 3 presents the dose-response of our system with both incubation and accumulation steps performed on-chip and taken as the reference curve in the following discussion section. Error bars were calculated over three acquisitions.

The integration of the incubation step within the microfluidic system is a key step in the design of autonomous lab-on-chip platforms. Recent approaches emphasize the need to maintain a certain level of agitation for beads during incubation, in order to maximize the interaction between beads and target analytes in the solution [11, 115, 116]. Indeed, a local increase of the convection phenomenon in close vicinity of the beads would reduce mass transport issues and speed up the supply of analyte. The incubation step we implemented on the horizontal lines appears to be as efficient as a standard turbulent off-chip incubation, even though it was previously reported that turbulent incubation performs better than exposure to continuous flows [117, 118]. Our solution thus succeeded in providing an incubation as efficient as the gold standard off-chip methodology.

The NGAL concentrations that could be detected with our device ranged from 1 to 100 ng/mL,

3.1 Point-of-care system or Acute Kidney Injury detection

with a limit of detection of 1 ng/mL, calculated using a three-times standard deviation approach. However, as the concentrations expressed in the calibration curve refer to the five times diluted serum, this interval can be translated into a 5–500-ng/mL detection range in non-diluted serum. This interval covers the clinical NGAL concentration values observed in healthy patients (around 80 ng/mL) and patients suffering AKI (above 300 ng/mL) [108, 119]. Furthermore, the standard deviation calculated with our platform appears to be small enough to distinguish healthy patients from ill patients. Indeed, the clinical procedure for AKI diagnosis, defined as an increase of more than 100% of the NGAL basal concentration [108, 120], is resolvable with our platform, which makes our device suitable for the rapid diagnostics of kidney injury. In order to compare the performance of our platform with a state-of-the-art method, the same samples were tested by ELISA (Figure 3.8) , exhibiting similar performances, with comparable sensitivity over a 1–100-ng/mL concentration range. Notably, the assay time could be shortened down to 15 min with our platform, versus 4 h required to run the ELISA test.

All experiments carried out within this section of the thesis were run in 5 times diluted serum sample (FBS: fetal bovine serum). As none of the previous studies employing DEP to perform immunoassay on beads relies on serum [58, 110], we are the first to implement the detection of analytes with DEP in a representative medium.

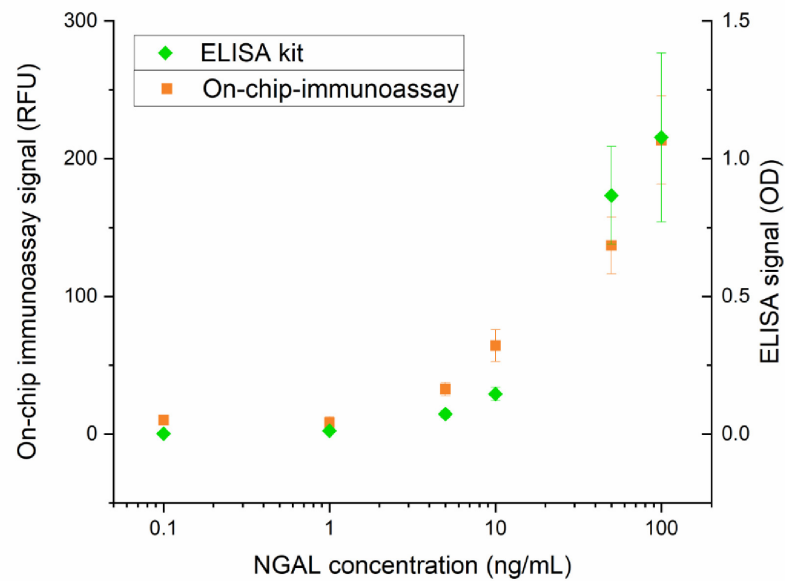


Figure 3.8: NGAL detection performance comparison between our immunoassay on chip and a commercial ELISA kit The total assay time is about 4 hours for the ELISA kit (R&D biosystems, UK) versus 15 min with our on chip integrated protocol. In terms of performance both assays can detect concentration ranging from 1 to 100 ng/mL (for 1 ng/mL the signal to noise ratio is 4 for ELISA and 3 for the chip), and comparable sensitivity over that entire range. Error bars were calculated over three acquisitions.

3.1.5 Multiple biomarker detection

This section aimed to investigate the possibility to concomitantly quantify the concentration of two biomarkers on a single chip. The two chosen analytes, NGAL and Cystatin C, spike into serum at different stages of the kidney injury [107]. Three hypothetical scenarios were defined based on clinical data: a “healthy” patient who presents basal levels for both NGAL (75 ng/mL) and Cystatin C (250 ng/mL), an “early-stage” patient presenting a spike in NGAL (300 ng/mL) and basal Cystatin C levels (250 ng/mL), and finally a “late-stage” patient presenting a spike in Cystatin C (1000 ng/mL) and basal NGAL levels (75 ng/mL). In order to decipher the efficiency of beads’ separation, NGAL and Cystatin C detection antibodies were labeled with fluorophores emitting in different spectral regions, respectively in CY5 and CY3 regions. The spectral overlap between fluorophores was also investigated to ensure negligible spectral overlap due to the fluorophore emission ranges as seen in figure 3.9.

The first step to carry out this experiment is to validate the detection of Cystatin C in an independent configuration such as the one presented for NGAL in the previous section. Such study was performed with 2 μm -diameter beads decorated with anti-Cystatin Ab maintained against a flow of 0.4 $\mu\text{L}/\text{min}$ and provided the dose response curve presented in figure 3.10. We observed a limit of detection of 0.5 ng/mL and a detection range covering concentrations from 0.5 to 200 ng/mL, which translates into a 2.5 to 1000 ng/mL range upon taking into consideration the five times dilution factor and suits the clinical requirement for detection of AKI in patients [106]. Furthermore, the resolution at 50 ng/mL was calculated and estimated to be of 11 ng/mL.

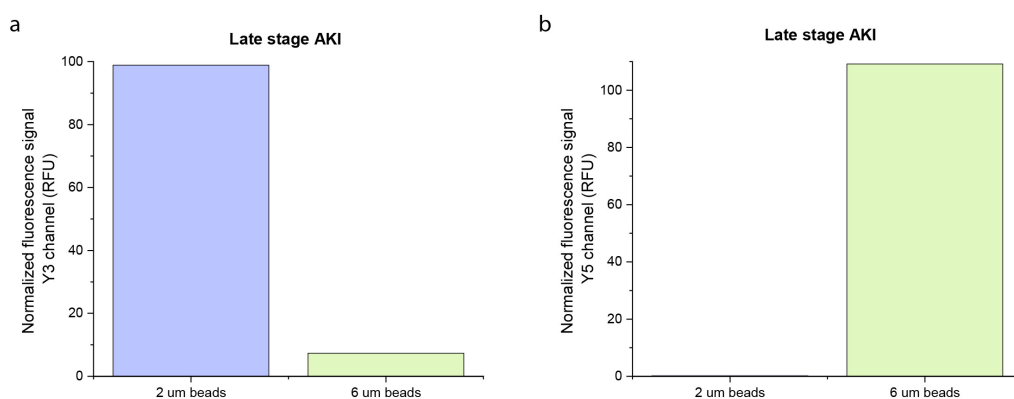


Figure 3.9: Spectral overlap of CY3 and CY5 signals from 6 μm NGAL and 2 μm Cystatin C-decorated beads Beads were incubated for 15 minutes in vials in the late stage conditions (NGAL concentration: 50 ng/ml, Cystatin C concentration: 1000 ng/ml) and the corresponding signals of single beads were acquired in both CY3 (a) and CY5 (b) fluorescent channels.

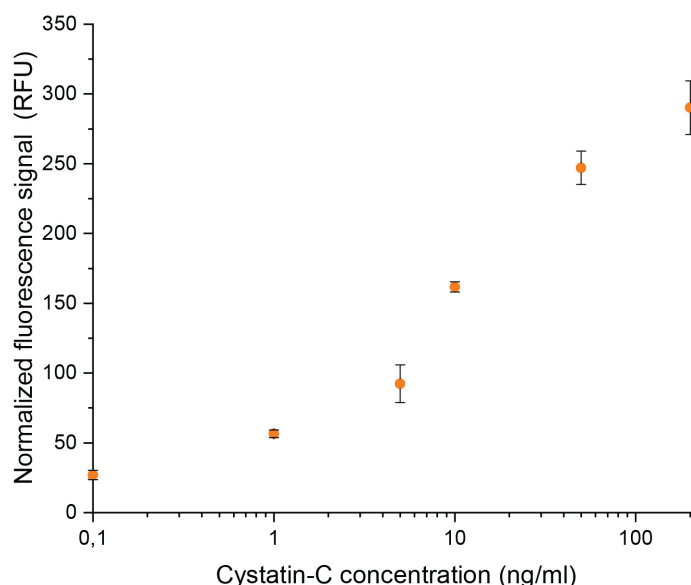


Figure 3.10: **Cystatin C dose response curve** Results of sandwich immunoassay performed on the microdevice on Cystatin C samples. The flow rate during the incubation is set at $0.4 \mu\text{L}/\text{min}$ and the beads used for this experiment have a diameter of $2 \mu\text{m}$. The same molecule was measured also in a multi-analyte configuration (Figure 6). In the present plot, the measured intensities are lower, which could be explained by a decrease of the fluorophore performance due to aging. Error bars were calculated over three measurements.

The simultaneous detection of NGAL and Cystatin C was carried out using two different layouts, one using the DEP actuation to discriminate beads of different sizes and another employing two channels for a spatially differentiated detection.

Size-based sorting of beads

A similar protocol as the one for single immunoassays can be applied to run two distinct immunoassays in parallel on the same channel. No change in the device layout was necessary from the original system. Two different beads' populations ($2\text{-}\mu\text{m}$ and $6\text{-}\mu\text{m}$ diameter) were functionalized with cAbs for Cystatin C and NGAL, respectively. The beads-cAbs solution was obtained by adding $10 \mu\text{L}$ 0.5% (w/v) $2\text{-}\mu\text{m}$ beads and $10 \mu\text{L}$ 0.5% (w/v) $6\text{-}\mu\text{m}$ beads in 1 mL 5-fold diluted FBS. The incubation step was performed on two different lines (the line upstream was activated by applying a 14-Vpp, 1-MHz signal and the line downstream by applying a 20-Vpp, 1-MHz signal) in presence of a $0.4 \mu\text{L}/\text{min}$ flow, maximal flow that was applied while holding the small $2\text{-}\mu\text{m}$ beads against the flow. The line upstream was set to exert a weaker electric field so that beads of larger size were trapped by the first line, while the smaller ones could pass through, to be successively trapped by the second line, with a

trapping efficiency of 90% and 70% for the 6- μm and the 2- μm beads, respectively. After beads' clustering, incubation was performed flushing a solution containing the analyte–dAbs complexes of both Cystatin C and NGAL, with the dAbs labeled with CY3 and CY5 fluorophores, respectively. Following incubation, the two beads' populations carrying the two distinct sandwich assays were released and concentrated at different locations on-chip. To do so, the two accumulation lines were activated (line upstream electrical stimulus: 14 Vpp, 1 MHz; line downstream electrical stimulus: 20 Vpp, 1 MHz), and the flow was set to 0.8 $\mu\text{L}/\text{min}$, maximal flow allowing accumulation of 2- μm beads. The two distinct clusters were imaged in CY3 and CY5 fluorescent channels with 5000-ms exposure times. An average of 20 experiments (incubation, accumulation, and beads' release) could be performed before the appearance of clogging issues preventing the chip from further use.

Figure 3.11a shows the achieved spatial separation of beads based on their size, with the 6- μm and the 2- μm beads, respectively, appearing as in red or green. The performance of this multianalyte approach is quantified in Figure 3.11b for the three patients described above. As the fluorophores emitting in CY3 and CY5 regions were different in brightness, the comparison between the absolute fluorescent signals was not relevant.

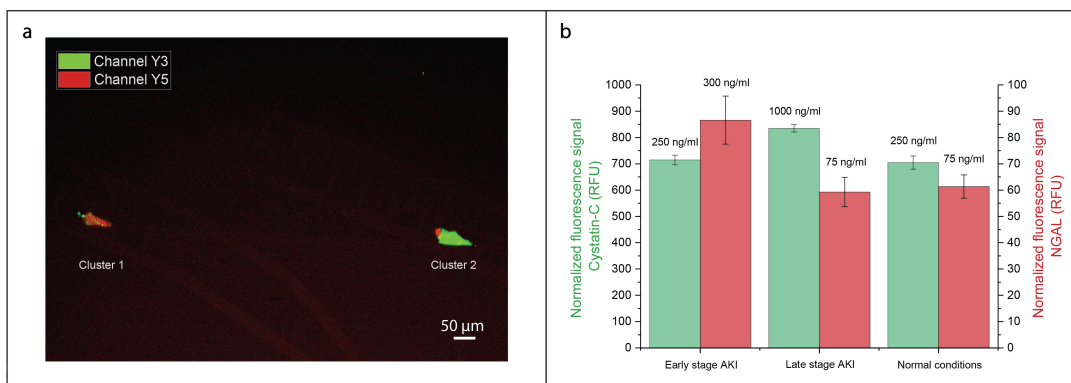


Figure 3.11: Simultaneous detection of NGAL and Cystatin C for acute kidney injury (AKI) diagnosis (a) Superposition of two clusters acquired, respectively, in CY5 fluorescent channel (NGAL label) and CY3 channel (Cystatin C label). This picture was taken in the case of an “early” patient (NGAL: 300 ng/mL, Cystatin C: 250 ng/mL). (b) Fluorescent signal acquired for CY3 channel (Cystatin C detection) and CY5 channel (NGAL detection), respectively, in cluster 2 (downstream, accumulating 2- μm beads capturing Cystatin C) and cluster 1 (upstream, accumulating 6- μm beads capturing NGAL). Three cases were investigated, corresponding to the clinically relevant situations: an “early-stage” patient with high NGAL and normal Cystatin C concentrations, a “late-stage” patient with high Cystatin C and normal NGAL concentrations, and a “healthy” patient with normal NGAL and Cystatin C concentrations. Error bars were calculated over three measurements.

For the CY5 channel (Figure 3.11b, red), corresponding to the fluorescence of 6- μm beads capturing NGAL collected in cluster 1, the detection of the NGAL spike in the “early” case scenario appears to be clearly resolved. The presence of some signal in cluster 2, shown in

Figure 3.12, for all scenarios suggests that some 6- μm beads could cross the first electrical barrier and get trapped at the downstream location. This contamination, evaluated at 20% of the signal obtained in the 6- μm beads' clusters, was due to defects in the electrical contact between some of the vertical pillars and the planar electrodes, leading to the leaking of beads through the lines and unwanted gathering in the downstream region, which could be reduced by an optimization of the microfabrication process. The signal produced by NGAL beads appears lower than the one observed with a similar concentration in the previous section, which was due to the smaller flow rate used in this experiment for incubation, 0.4 $\mu\text{L}/\text{min}$ vs. 2 $\mu\text{L}/\text{min}$.

Regarding the CY3 channel (Figure 3.11b, green), corresponding to the fluorescence of 2- μm beads capturing Cystatin C accumulated downstream in cluster 2, the detection of the Cystatin C spike in the "late" case scenario can be resolved vs. normal conditions. Contamination can also be noticed (Figure 3.12) in cluster 1 for all scenarios. We estimated that contamination were equivalent to 25% of the signal obtained in the 2- μm beads' clusters and arose from a tendency of small beads to stick together and with large beads, therefore, forming clusters while incubating on horizontal lines. Those clustered beads then behaved as larger beads and, thus, accumulated in cluster 1. Such effect could be mitigated through the introduction of a surfactant in the reaction solution. Moreover, assuming that the assay will be calibrated to result in comparable fluorescence signals corresponding to physiological basal levels of NGAL and Cystatin C (healthy patient), a 20% variability due to contamination would not prevent us from detecting a 100% increase in one of the marker concentrations, as an effect of an AKI condition.

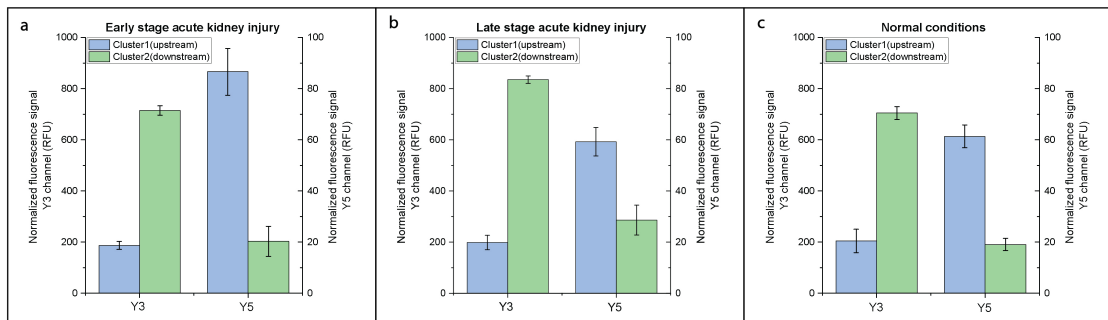


Figure 3.12: Cross-contamination analysis in the multianalyte experiment Fluorescence signal acquired for both CY5 channel (NGAL detection) and CY3 channel (Cystatin C detection) in cluster 1 (upstream, red cluster in Figure 6a, accumulating 6 μm beads capturing NGAL) and cluster 2 (downstream, green cluster in Figure 6a accumulating 2 μm beads capturing Cystatin C). The three cases presented here are the same as those described in Figure 6. In order to calculate the error bars, three acquisition were performed.

Our technology permitted the efficient discrimination of healthy, "early AKI" and "late AKI" patient through the quantification of NGAL and Cystatin C levels. Despite this achievement we still observed a non negligible level of contamination that could be partially mitigated

thanks to the solutions proposed above. We came up with a different layout that maintain the level of performance in the assessment of NGAL and Cystatin C concentrations while greatly reducing the noise due to contamination.

Channel-based sorting of beads

The main difference between this novel layout and the one presented in the previous section stands in the method employed to differentiate beads labelled with different antibodies. In the previous design beads were sorted by DEP forces based on their size; conversely, in this second version, two sets of beads are injected in two separated channels. A common inlet is used to inject the analyte concomitantly in both chambers (figure 3.13). Assuming that the flow at the three inlets are carefully balanced we expect to have little to no contamination from one channel to another, thus we can use beads of same diameter, here 6- μm , as they are more suitable for manipulation by DEP forces.

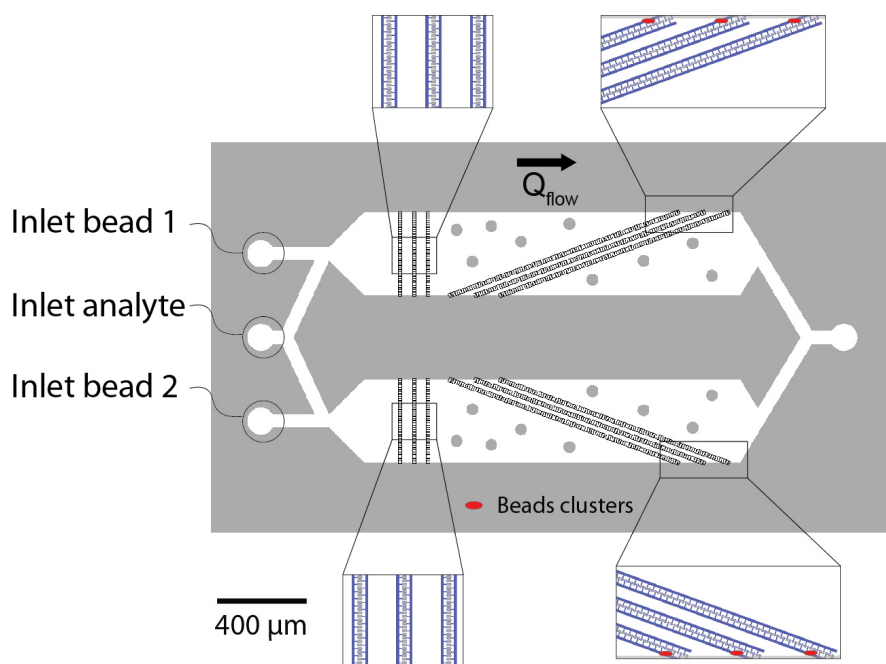


Figure 3.13: Layout of the platform for beads injection and incubation in two separate channels Beads are injected through dedicated inlets and reagent are injected through the central inlet. The device consists of two channels, each composed of three incubation lines followed by three accumulation lines, for the formation of the beads clusters shown in red.

The experimental process we employed was very similar to the one previously implemented. Two sets of 6- μm -diameter beads were functionalized with Ab directed against NGAL and Cystatin C. Each set was injected through its dedicated inlets at 2 $\mu\text{L}/\text{min}$. The trapping and clustering of beads at the incubation lines occurred upon application of 20-Vpp, 1-MHz signal. Once the clusters reached a certain size we stopped the flow of beads and set a flow of 2 $\mu\text{L}/\text{min}$.

3.1 Point-of-care system or Acute Kidney Injury detection

of analyte–dAbs complexes of both Cystatin C and NGAL, with the dAbs labeled with CY3 and CY5 fluorophores, respectively. After 15 minutes, the sandwich-immunoassays formed on the two sets of beads trapped on the horizontal lines were released and accumulated at different locations on-chip by applying a 20-Vpp, 1-MHz signal. The two distinct clusters were imaged in CY3 and CY5 fluorescent channels with 5000-ms exposure times (Figure 3.14).

Figure 3.14 presents the results obtained in a typical experiment studying the detection of NGAL and Cystatin C in early and late stage scenario of AKI with the two channels platform. In both CY3 and CY5 channels the spikes of NGAL and Cystatin C, occurring in the early and late case scenario, respectively, could be reliably resolved. Figure 3.15 shows a considerable reduction of the cross-contamination between Cystatin-C and NGAL beads with this approach. Even though the unspecific binding was proven to be low in figure 3.9, it appeared to have a non-negligible contribution to the total fluorescent signal, that could be subtracted through the use of a control experiment exposing the functionalized beads to the flow of detection antibodies in the absence of analytes. However this approach suffers from two main drawbacks, namely the use of an additional inlet that makes the microfluidic set-up more complex and the addition of an additional channel that almost doubles the footprint of the device.

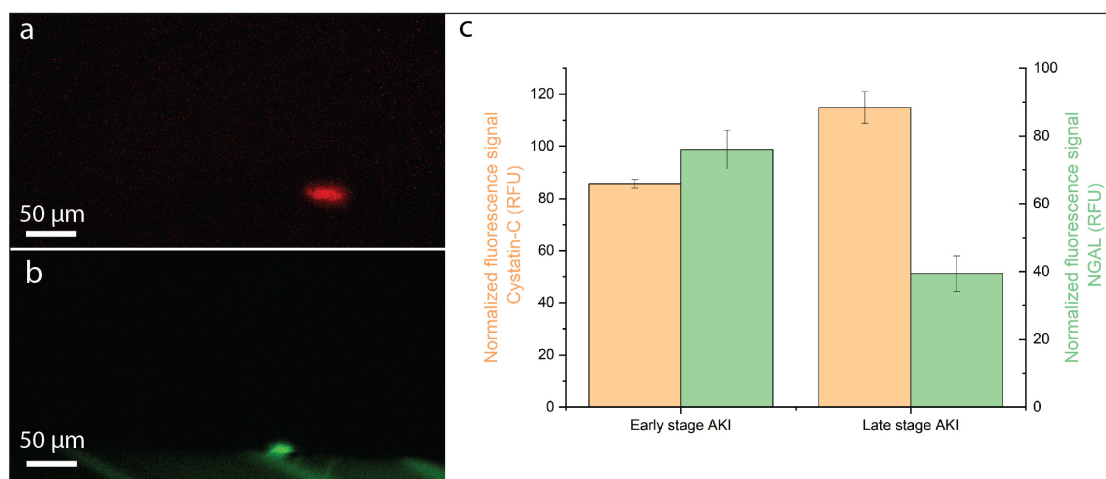


Figure 3.14: Simultaneous detection of NGAL and Cystatin C with a two channels device (a),(b) Superposition of two clusters acquired, respectively, in CY5 fluorescent channel (NGAL label) and CY3 channel (Cystatin C label). This picture was taken in the case of an “early” patient (NGAL: 300 ng/mL, Cystatin C: 250 ng/mL). (c) Fluorescent signal acquired for CY5 channel (NGAL detection) and CY3 channel (Cystatin C detection), respectively, in the red cluster (left side of the chip, accumulating 6-μm beads capturing NGAL) and green cluster (right side of the chip, accumulating 6-μm beads capturing Cystatin C).

Both layout presented above could identify “early AKI” stage and “late AKI” patient via a detection of both NGAL and Cystatin C in clinically relevant ranges [106, 108, 120, 121] within 15 min. As NGAL and Cystatin C spike in the serum at different stages of kidney failure [107], our approach combining detection of both these biomarkers within one test allows for kidney

injury detection within a large time window, from the very initial stage to after 48 h, reducing the risk of inaccurate diagnosis and improving survival rate in patients experiencing AKI. Our device could perform the detection of analytes within 15 min requiring a serum volume of only 50 μ L, which seems compatible with its integration into a point-of-care platform available at the intensive care unit and requiring a small amount of blood to perform the analysis [96].

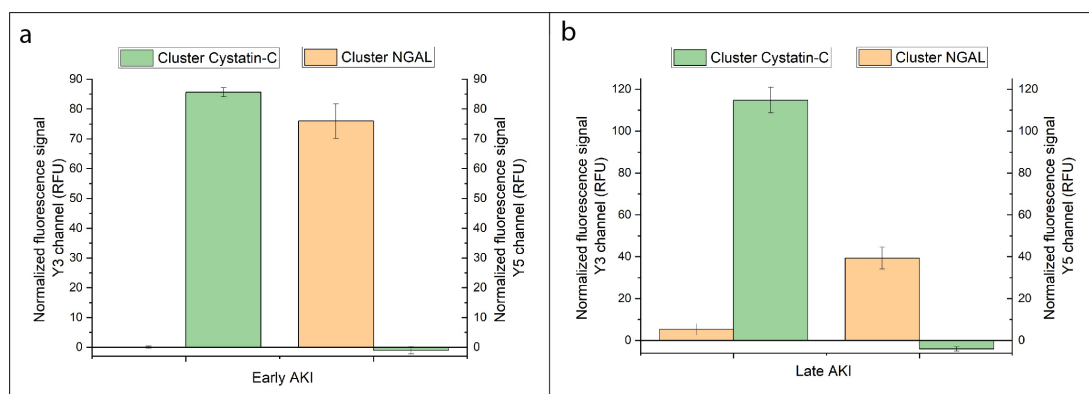


Figure 3.15: **Cross-contamination analysis in the multianalyte experiment with two channels.** Fluorescence signal acquired for both CY5 channel (NGAL detection) and CY3 channel (Cystatin C detection) in cluster 1 (red cluster in Figure 3.14a, accumulating 6- μ m beads capturing NGAL) and cluster 2 (green cluster in Figure 3.14b accumulating 6- μ m beads capturing Cystatin C). In order to calculate the error bars, three acquisition were performed.

Previous approaches aiming to simultaneously carry out multiple biomarkers' detection mainly relied on the use of fluorophores incorporated within the beads [122, 123]. A technology, developed by Luminex, associates a barcode defined as a ratio between two fluorophore dyes in the bead to each analyte of interest [124], thus allowing for efficient detection of distinct markers in a flow cytometry setup [125]. Despite its performance, the main limitation of this solution is the need to integrate at least two fluorescent filters within the readout platform for barcode reading. This requirement severely hinders a potential integration of this technique in portable devices. Nonetheless, as beads in our DEP-based platform are resolved spatially according to their sizes or spatial arrangement, the readout can be performed with a single fluorescent channel that can be easily integrated within a PoC device [96]. Another option to optically quantify multiple species circumventing the need for multiple fluorescence channels was proposed by Falconnet et al. [87], who introduced a digitally encoded silicon disk, on the top of which immunoassays would be performed. However, as each barcode has to be observed singularly, the silicon microparticles cannot be accumulated to increase the overall sensitivity of the system. Our method, instead, allows both multimarkers analysis and amplification of the outcome signal. Our platform is, thus, the first of its kind, featuring (i) optimized analyte collection, (ii) multiple biomarkers' detection, (iii) signal amplification, and (iv) optical readout by means of a single fluorescence channel.

3.2 Oligo-based platform for fast screening of multiple biomarkers

The aim of this section is to present and implement a platform for the rapid screening of multiple markers. As the presence of a single marker can be related to various disorders [126], a diagnosis based on multiple analytes could importantly contribute to better diagnosis performances [127]. Microfluidic offers numerous benefits in the context of multi-markers detection, such as limited reagent volume per test [128], efficient incubation [129] and the possibility to integrate many testing sites within a very small footprint [21]. For instance, Migliozi et al. [130] developed a microfluidic platform for rapid and sequential detection of 10 molecules in an immuno-fluorescence set-up. In a work relying on the powerful Quake valve approach presented in section 1.3, Volpetti et al. [131] could successfully detect five biomarkers in a proof-of-concept configuration and possibly up to 384 biomarkers with a single device. While the previous section investigated the rapid detection of biomarkers in a compact device, this section explores the use of oligonucleotide labels to perform the quantification of a large number of species in the same assay.

3.2.1 General concepts and state-of-the-art

The main concept of this section is to carry out a standard sandwich immunoassays on beads but the fluorophore on the detection antibody is replaced with a DNA strand barcode specific to this antibody. The injection of the complementary DNA strand associated with a fluorophore would permit a quantification of this biomarker level. Furthermore, provided that we can eliminate the fluorescent signal associated with this barcode, we can repeat this operation to quantify another marker with the same fluorescent channel. Figure 3.16 illustrates the concept in the case of two analytes, where a single bead is decorated with different antibodies. It is interesting to mention that the aim of this approach is not to perform incubation of analytes and antibodies on-chip but to carry out out a rapid and sequential readout of beads following incubation. We will discuss here the use of barcodes combined with immunoassays and possible methods for the removal of fluorescence signal following quantification.

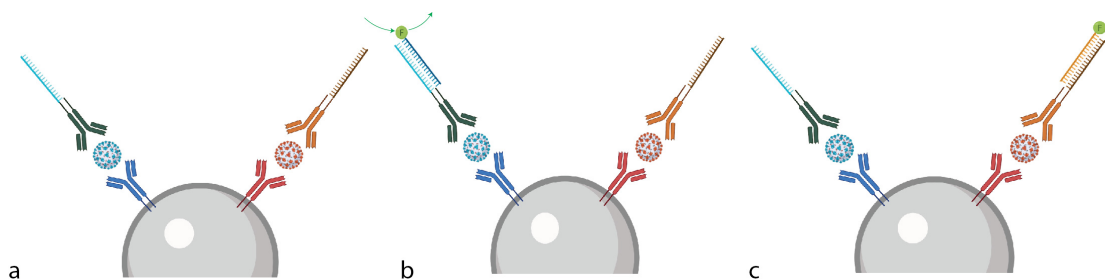


Figure 3.16: **On-beads analyte detection thanks to DNA barcoding** A sandwich immunoassay is performed on the surface of the beads (a), then fluorescently-labeled DNA strands are sequentially injected (b) and discarded (c).

DNA barcoding for immunoassay

The association of immunoassays with DNA barcoding has been introduced in the last years in an attempt to combine the best of both methods, namely the high specificity of immunoassays and the signal amplification permitted by molecular biology [132]. The most successful example of such approach is called immuno-PCR. Proposed in 1992 by Sano et al. [133], it consists in the replacement of the detection enzyme in a standard enzyme-linked immunosorbent assay (ELISA) by a biotinylated DNA strand coupled to the antigen/antibody complex through a streptavidin molecule. Such approach allowed a tremendous improvement of the detection performances of the assay, with 10^5 increase in the limit of detection of the system. Since its proposal immuno-PCR has been successfully employed for the detection of tumor markers such as carcinoembryonic antigen [134], viral infections [135] or bacterial infections [136]. Despite its clear advantages in terms of sensitivity and reproducibility immuno-PCR suffers from several limitations hindering its general adoption in the diagnosis field. Its main drawback resides in the presence of high background signals caused by assay contamination during washing steps or by the presence of unbound DNA strands after the DNA/Ab conjugations. The numerous steps required to perform an immuno-PCR makes it a cumbersome procedure, that necessitates many skilled operators and comes at a high cost [132].

A critical aspect of the combination of immunoassays with DNA barcode is the development of methods to perform the coupling of nucleic acid strands to antibodies [137]. While remaining cost effective, such methods should limit steric hindrance issues and maintain the reactivity of the antibody with the targeted epitope of the antigen. The coupling can be carried out through the implementation of non-covalent binding strategies, such as for instance streptavidin-biotin coupling [133] or covalent binding approaches such as thiol-maleimide chemistry [138]. While many coupling strategies require a modification of the antibodies to add chemical groups through enzymatic reaction [139] or chemical tagging [140], the use of the native amine groups already present in the antibodies via N-Hydroxysuccinimide ester (NHS) chemistry appears as a suitable solution [137].

Approaches to cancel out the fluorescent signal after its measurement

Once the sandwich immunoassays-complexes are formed and the first DNA strand binds its complementary sequence, its fluorescent label ensures the detection of the first analyte. Subsequently, the fluorescent signal related to this analyte has to be suppressed in order to perform the quantification of the remaining markers. The most immediate approach to separate the fluorescent DNA strand would be to increase the temperature, in order to perform the melting of the double DNA strands, a process frequently carried out for Polymerase Chain Reaction (PCR) [141]. Then, the next DNA strand can be injected in the microfluidic platform as presented in figure 3.17. However, this approach comes with severe limitations, namely the heating of the chip requires some heavy modifications of the experimental set-up and the high temperature experienced in the device may be detrimental to the antibodies and proteins already immobilized on the beads' surface [142], that prevented its integration to our system.

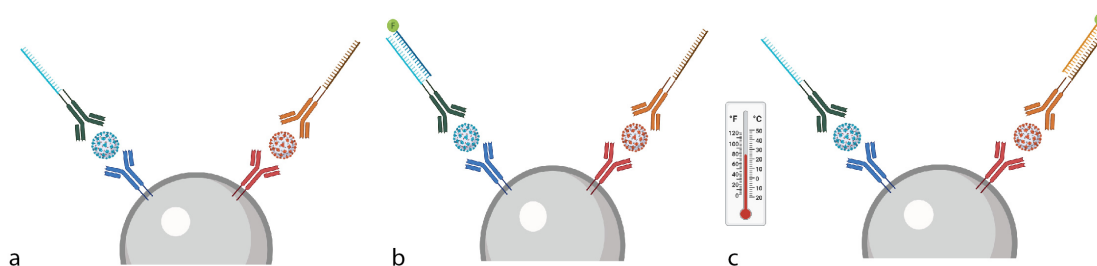


Figure 3.17: Use of heat as a possible solution for DNA double strands denaturation in the microfluidic channel In a first step the full immunoassays are performed on the beads surface (a), then the first fluorescently-labeled DNA strand is injected and the corresponding signal is acquired (b). Upon application of a high temperature the fluorescently labelled DNA strand detaches and is carried away by the flow while another DNA strand corresponding to another marker is flown in the chip (c).

Another option to suppress the fluorescent signal would be to take advantages of the photo-bleaching phenomenon. Photo-bleaching is a common yet non-suited irreversible degradation of a fluorophore performance [143]. This irreversible modification is caused by the degradation of covalent bonds within the molecule, that results in the transition of the fluorophore from a single-state to a triplet state [143].

Despite being considered as negative phenomenon that has to be mitigated in most cases, some researchers developed strategies to employ photo-bleaching as an ally, for instance Axelrod et al. [144] developed fluorescence recovery after photo-bleaching (FRAP), a method that allows to track cells or proteins over time. We propose here to also use the properties of photo-bleaching to serve our need for fluorescence suppression. Following its injection and quantification, the fluorophore attached to DNA is photo-bleached through the application of an intense light beam as illustrated in figure 3.18.

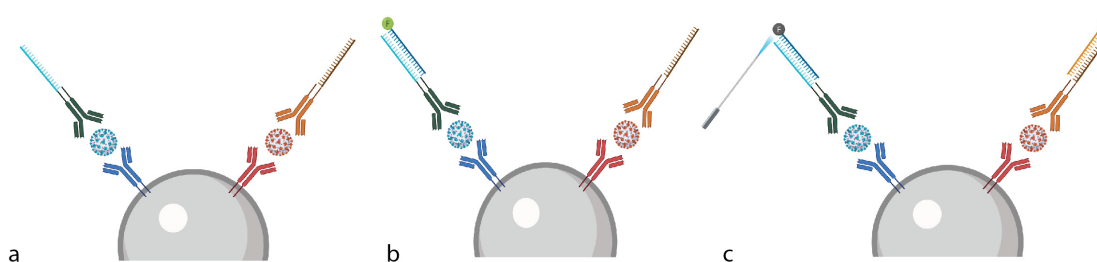


Figure 3.18: Use of photo-bleaching as a possible solution for fluorescence reduction in the microfluidic channel In a first step the full immunoassays are performed on the beads surface (a), then the first fluorescently-labeled DNA strand is injected and the corresponding signal is acquired (b). Upon application of an intense light beam the fluorophore photo-bleached and another DNA strand corresponding to another marker can be injected in the chip (c).

The last option we considered for the fluorescent signal elimination is the use of toeholds. First introduced as information mediator for DNA-based molecular computing [145, 146], toehold-mediated isothermal strand displacement relies on the use of a complementary domain shared by two DNA strands to promote their hybridization. It takes place in the presence of a double-stranded DNA structure presenting a short single-stranded overhang region, named 'toehold'. Upon exposure to an oligonucleotide complementary to the strand having the toehold the shorter strand in the duplex will be replaced by this longer complementary invader strand, requiring no enzymatic mediation [147]. The relationship between the thermodynamics of toehold hybridization and the kinetics of the toehold-mediated strand displacement was formalized by Zhang et al. [148]. The use of toeholds appear as a suitable solution for fluorescence reduction (figure 3.19). The fluorescent DNA strand is 7 bases longer than the one attached to the antibody and consequently does not bind entirely with it. Following fluorescence quantification the complete long complementary sequence (cleaning sequence) is injected, resulting in a thermodynamically favored equilibrium that leads to the cleaning of the beads surface from fluorophores.

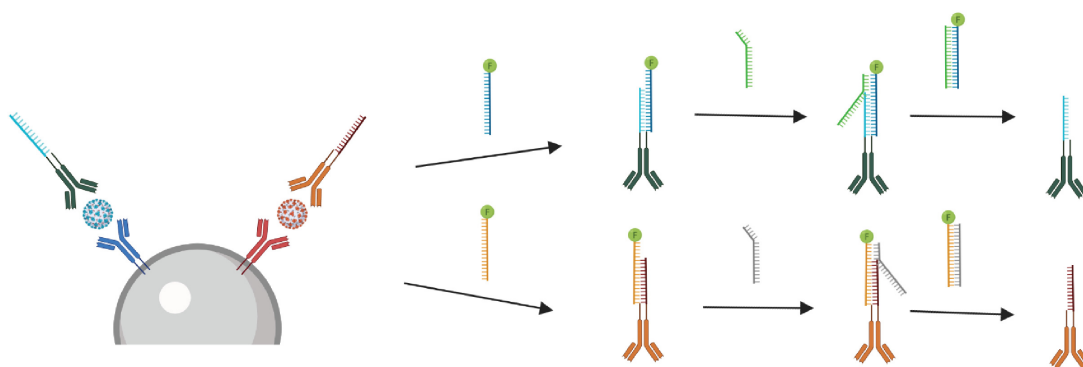


Figure 3.19: Toehold-mediated isothermal strand displacement as a possible solution for fluorescence reduction in the microfluidic channel. In a first step the full immunoassays are performed on the beads surface, then a fluorescently-labeled DNA strand is injected in the channel, hybridizes with its complementary sequence for signal quantification, and finally is removed upon injection of a longer complementary DNA strand.

3.2.2 System layout and operating principle

The design and performance of the structures implemented to maintain beads immobilized against the flow was presented in chapter 2 section 2.2.3. A reminder of the structure of a single trap is provided in figure 3.20b. The choice of a trapping method that differs from the DEP trapping presented above was motivated by the need to immobilize the beads against high flow rates, that will contribute to fast exchange of reagents and therefore a high throughput for biomarker quantification. The general layout of the microfluidic device is given in Figure 3.20a. It consists of a single channel with 3 inlets and 1 outlet. One inlet is dedicated to the injection of beads while the two others can be employed for the sequential injection of reagents. Both

3.2 Oligo-based platform for fast screening of multiple biomarkers

inlets and outlets features filters that prevent the introduction of excessive dust in the channel. The sequential injection of fluorescent DNA strands permits to perform the detection with only one fluorescent channel.

The injection of beads and reagents is performed thanks to three syringe pumps (Harvard Apparatus, USA). The degassing is carried out applying a high pressure (600 mbar) at the outlet with a peristaltic pump (Elveflow OB-1, France) with closing the inlets with syringes. Prior to each experiment, the microfluidic devices are primed with a PBS solution supplemented with 1% BSA to reduce unspecific binding.

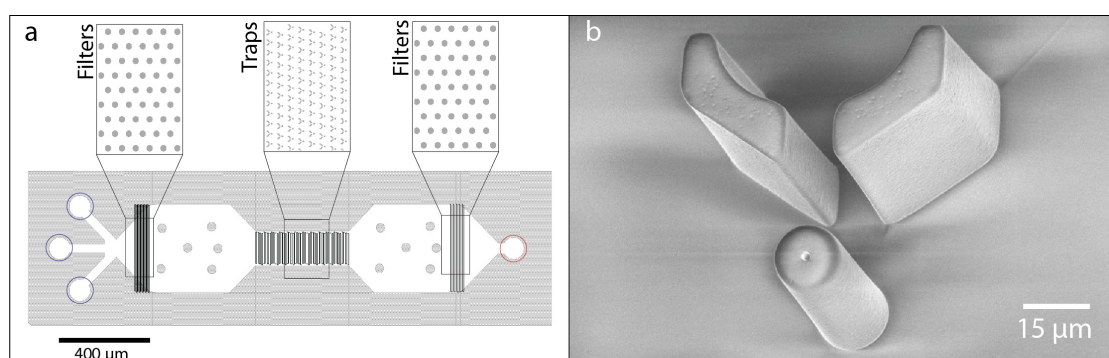


Figure 3.20: **Layout of the platform for on-chip incubation of beads** (a) Presentation of the chip layout. Beads and reagents can be successively injected through the three inlets circled in blue on the image and discarded through the outlet circled in red. (b) SEM picture of a PDMS trap that can immobilize a single bead against the flow.

3.2.3 On-chip coupling of DNA probes with DNA-decorated beads

The experiments described in this section aimed at getting a good comprehension of DNA strands hybridization within a microfluidic channel (figure 3.16) . To this end we directly attached DNA strands to the surface of the beads via a biotin-streptavidin link. The beads were injected and arranged in the microfluidic channel and the complementary DNA strand was injected at different flow rates. The sequence of the capture and detection DNA strands are provided in table 3.1.

	Capture	Detection
Sequence	Biotin-CACAACAAAAACAACAC	Alex647-GTGTGTGTTTTTTGTGTG

Table 3.1: **DNA sequences designed for the experiment described in Figure 3.21..**

Figure 3.21 illustrates the real time monitoring of fluorescence on-chip and overtime. From this plot we can deduce that the binding occurs very quickly, indeed, after 2 minutes the fluorescent signal reaches a steady value for both flow rates of 10 $\mu\text{L}/\text{min}$ and 20 $\mu\text{L}/\text{min}$.

Furthermore, as we are operating at high flow rates and with micron-size particles, the system is expected to present high Peclet numbers P_{eH} and P_{eS} . In this specific case we demonstrated in the introduction that an increase in the flow rate has a negligible impact on the flux of analyte at the bead surface, a theoretical finding that is corroborated by experimental results showed in figure 3.21b. Since the DNA strands are available in large amounts we can afford to lose a significant proportion during the on-chip incubation. The incubation duration is a more critical parameter, and maintaining it very short (e.g. below 2 minutes), would allow a rapid and highly multiplexed detection of many biomarkers.

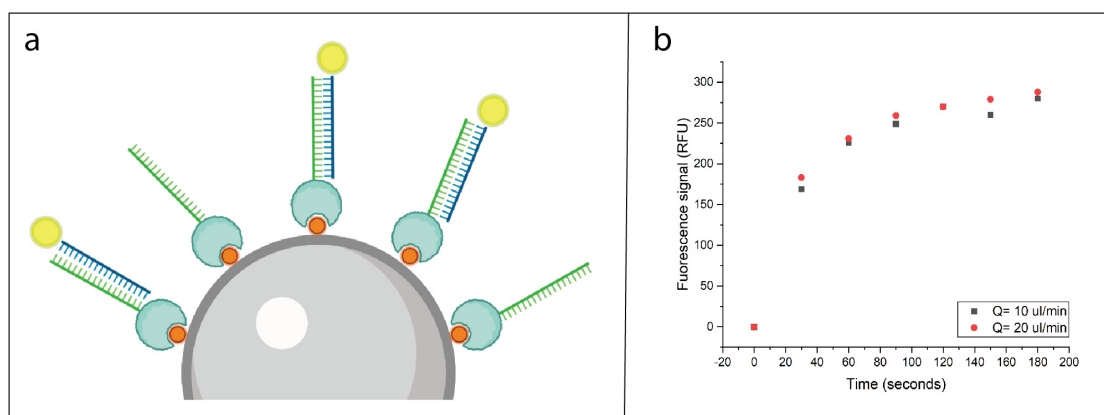


Figure 3.21: **Study of the on-chip hybridization of two complementary DNA strands** (a) Scheme of the beads used for this experiment. DNA strands were placed at the surface of the beads thanks to streptavidin-biotin biochemistry. The beads were immobilized in the chip and exposed to their complementary DNA sequence labelled with a fluorophore. (b) Fluorescent signal as function of the incubation time for two different flow rate of reagents. After 2 minutes the signal begins to saturate.

3.2.4 Study of fluorescent signal bleaching

Upon verification that the hybridization could be efficiently carried out on-chip we investigated different strategies to suppress the fluorescent signal, to allow for subsequent injection of fluorescently-labeled DNA strands. The heating strategy was not tested here due to its inherent limitations, as a reminder, the risk to damage proteins due to high temperatures and the complexity of the heating set-up. Consequently, we focused on the photo-bleaching strategy. Two fluorophores, Alexa Fluor 647 and Alexa Fluor 546, were selected for this study. Due to their high signal to noise ratio, they are widely adopted within the scientific community. We could have chosen early generation fluorophores, e.g. fluorescein, that are known to be more prone to photo-bleaching, but this would have been at the cost of reduced performances, contradicts our ambition to develop high performance diagnosis tools. In order to observe photo-bleaching beads were functionalized with DNA strands and incubated off-chip with their complementary sequences. The beads were placed on a glass slide and the fluorescence decay was monitored while the beads were exposed to the light beam of a 150 Watt UV lamp.

3.2 Oligo-based platform for fast screening of multiple biomarkers

The sequences of the capture and detection DNA strands for both fluorophores are provided in table 3.2.

	Capture	Detection
AF 546	Biotin-TGTGGTGGGTGGGTGGTGT	Alex546-ACACCACCCACCCACCACA
AF 647	Biotin-CACAACAAAAACAACAC	Alex647-GTGTGTGTTTTTGTGTGTG

Table 3.2: DNA sequences designed for the off-chip photo-bleaching study.

Figure 3.22 presents the results of the photo-bleaching monitoring. In the case of Alexa Fluor 546 (figure 3.22a), fluorescence intensity remained above 50% after 10 minutes of exposure to light. We could also notice an unexpected increase of the signal for the control experiment, indeed, as the solution containing the beads was drying, the fluid movement caused the bead to change their focal plane which resulted in a slight increase of fluorescence. Figure 3.22b shows a much stronger exponential decay in the fluorescence after 10 min, as the signal reached only 3% of its initial value. Interestingly, even with minimal application of light (only during exposure time) the signal in the control experiment the fluorophore is unstable and its fluorescence decreases of 40% over time. The stronger photo-bleaching observed with Alexa Fluor 647 matched previous results reported in literature [149]. To conclude we found out that while Alexa Fluor 546 is too stable for photo-bleaching applications Alexa Fluor 647 could be employed in the scope of our project for signal cancellation, even though the relative long time necessary (10 minutes) for the bleaching to occur will limit the throughput of the device.

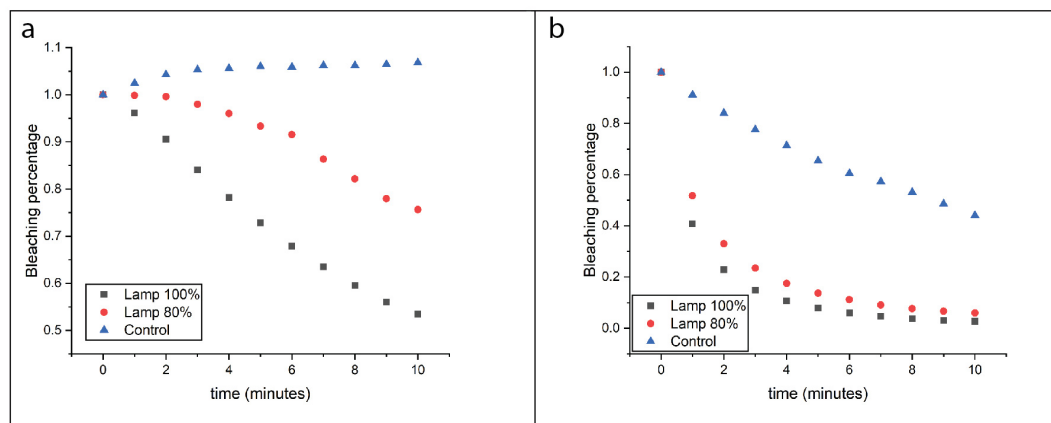


Figure 3.22: **Monitoring of the photo-bleaching of Alexa Fluor 546 and Alexa Fluor 647 fluorophores.** Functionalized beads were exposed to strong UV light and the decay of fluorescence was measured for both Alexa Fluor 546 (a) and Alexa Fluor 647 (b). The intensity of the light source varies from 100% to 80% of its maximal intensity, during the control experiments the sample is only exposed to the light when an image is acquired (100 ms every minute).

3.2.5 Toe-hold-based approach

Considering the throughput-related limitations of the aforementioned photo-bleaching approach, the toe-hold based displacement is a very promising solution for rapid signal cancellation. As the thermodynamic equilibrium favors the hybridization of long sequences, we expect an extremely low reminiscent signal after injection of the complementary DNA sequence. The validity of our approach was analyzed via a similar strategy as in previous section, namely DNA strands were directly attached on beads and the detection and cleaning sequences were sequentially added. The implemented procedure is illustrated in Figure 3.23.

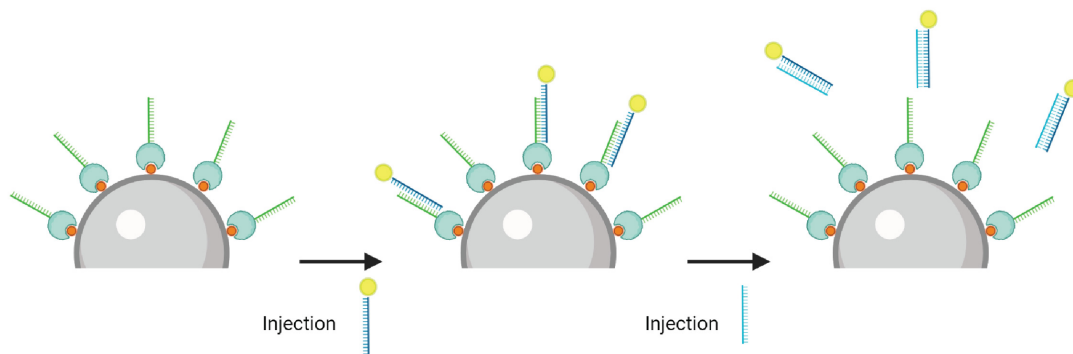


Figure 3.23: **Experimental validation procedure of the toehold approach** Beads are first decorated with capture DNA strands (a). Then as the detection DNA single strands are injected the fluorescence at the surface of the beads increases (b). Finally the toehold DNA single strand is injected, resulting in a decrease of the fluorescence signal (c).

The single stranded DNA sequences designed for the toe-hold approach validation are provided in table 3.3.

	Capture strand	Detection strand	Toehold strand
Toehold 1	Biotin- CACAACAAAAA- CAACAC	Alex647- TTGGTGTGTGTTG- TTTTTTGTTGTG	CACAACAAAAAACA- ACACACACCAA
Toehold 2	Biotin- TGTGGTGGGTGG- GTGGTGT	Alex647- AACCCAAACACCA- CCCACCCACCACA	TGTGGTGGGTGGG- TGGTGTTTGGGTT

Table 3.3: **DNA sequences designed for the investigation of the toehold approach.**

The beads were successively placed in contact with the detection and toehold DNA strands, with a washing steps to ensure the discard of unbound species. The plot results in figure 3.24 confirm that the cleaning of the beads surface from fluorescent molecules could be achieved with a high efficiency, with less than 2% signal remaining after exposure to the toehold DNA.

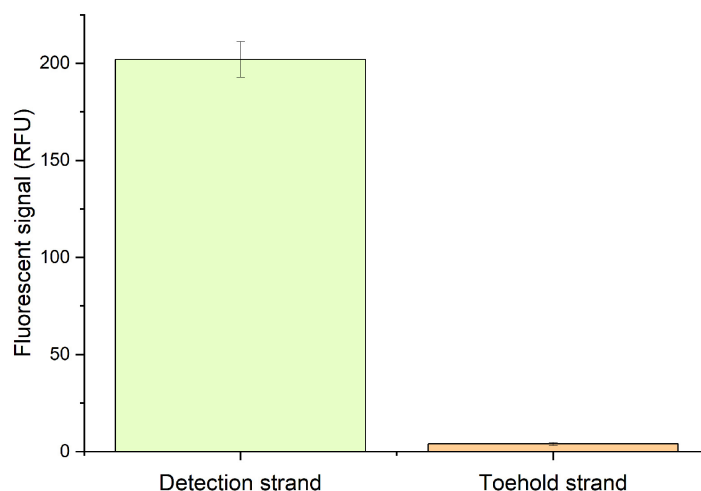


Figure 3.24: **Off-chip performance of the toehold signal reduction.** Upon injection of the detection single stranded DNA strand a high fluorescence signal is observed, such signal is significantly reduced after incubation with the toehold strand.

We attempted to reproduce these results in an on-chip configuration using beads functionalized with two different barcodes. The sequential injection of detection and toehold single stranded DNA was performed with a flow switcher (MUX, Elveflow). The real-time monitoring of fluorescence at the beads' surface is presented in figure 3.25. First beads were arranged in the mechanical restrictions, then the first fluorescent DNA strands were injected and bound to the beads exhibiting their complementary sequence leading to an increase in the corresponding fluorescence signal (figure 3.25a,c). Then the corresponding toehold DNA strand was flown on-chip, simultaneously with the second fluorescent DNA strands, resulting in a signal decrease signal for a set of beads while the other population experienced an increase in fluorescence (figure 3.25b,c). Finally the second toehold DNA strand was flushed over the beads leading to a complete elimination of fluorescent signals on the beads' surface. For the CAC sequence the binding between the detection strand to its complementary sequence occurred in about 1 minutes and provided a high outcome while the toehold mediated strand displacement took place within 3 minutes. Interestingly, the injection of the first toehold could be combined with the injection of the second detection DNA strand without any signal loss. The TGT sequence binding revealed a slower binding kinetic, suggesting that the system is reaction limited. The binding duration τ discussed in equation 4 associated with the TGT sequence is indeed higher than the one of the CAC sequence, resulting in a slower binding process. However, an improved design of the single stranded DNA sequence could allow for all the DNA strands to match the performance of the CAC sequence. Such results validate our approach to use the toehold-mediated strand displacement strategy for rapid cancellation of fluorescent signals and sequential detection of multiple biomarkers.

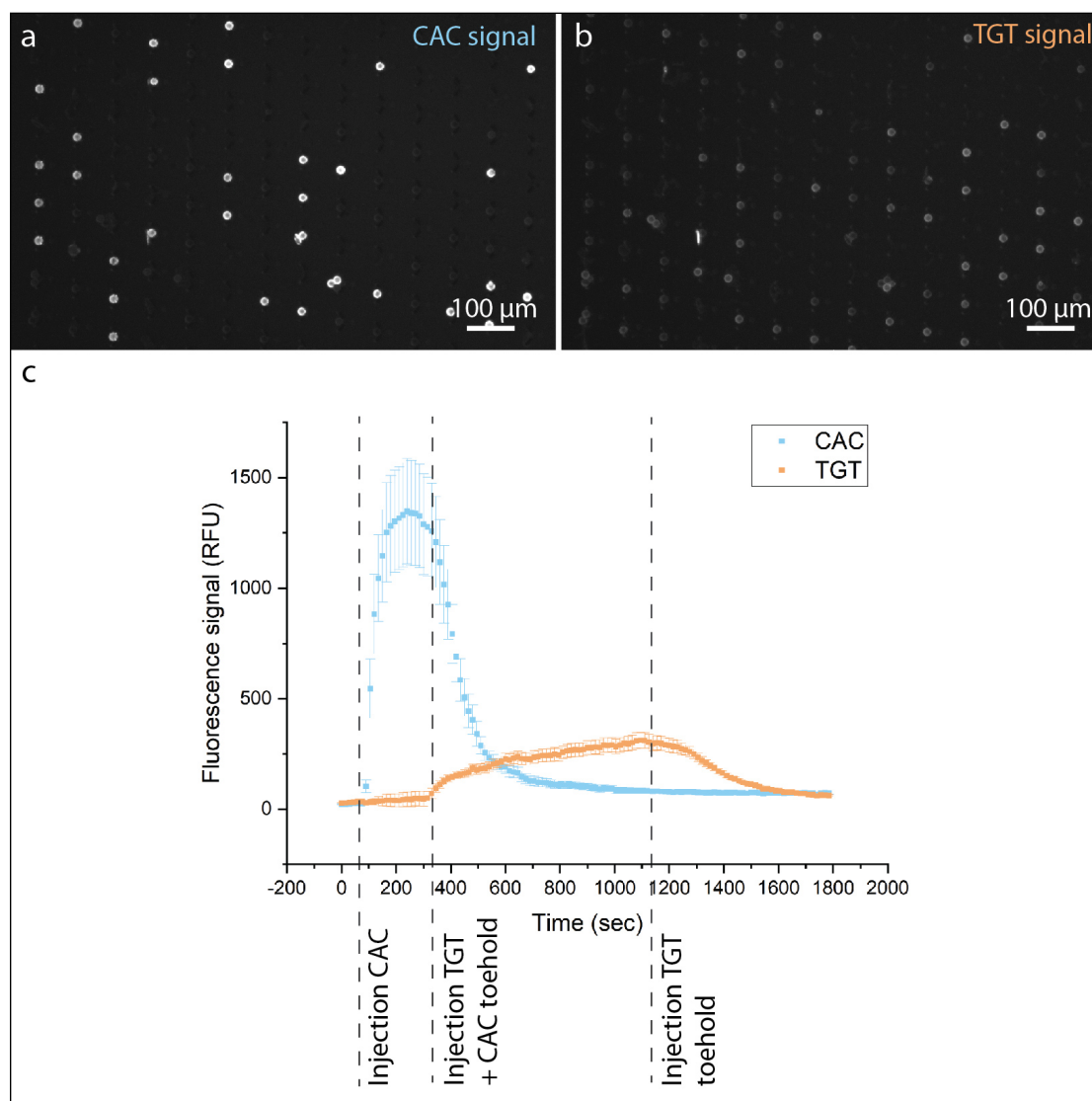


Figure 3.25: **On-chip sequential injection of detection and cleaning DNA sequences.** Functionalized beads were immobilized in the microfluidic restrictions and exposed to the CAC detection sequence, resulting in an increase of fluorescence at the surface of the corresponding beads (a,c). Then, following the simultaneous injection of the CAC toehold sequence and the TGT detection sequence, the fluorescence will increase for TGT-beads and decrease for CAC-beads (b,c). Finally, the injection of the TGT-toehold will bring the fluorescent signal of beads to their basal levels. Error bars were obtained by measuring the fluorescent signal from 6 beads.

After validation of the pertinence of the toehold assay in a simplified configuration we built the complete assay as illustrated in figure 3.16 and tested it on-chip. To do so we performed the conjugation of Cystatin C antibodies with the a single stranded DNA sequence given in table 3.4. Cystatin C is not a target marker for this system, nonetheless it was employed in

3.2 Oligo-based platform for fast screening of multiple biomarkers

this study for convenience reasons as it has been extensively studied in the scope of this PhD thesis and its behavior is well-understood. The conjugation was performed via an dedicated oligo conjugation kit (ab218260, Abcam) relying on click chemistry with a ratio 1:5 between antibodies and oligo.

ID	Sequence
Conjugation	CACAACAAAAACAACAC
Detection	TTGGTGTGTGTTGTTTTTGTGTG
Toehold	CACAACAAAAACAACACACACCAA

Table 3.4: DNA sequences designed for the conjugation of antibodies.

The sandwich immunoassay was performed off-chip with a Cystatin C concentration of 1000 $\mu\text{g/mL}$. After a 15 minutes incubation the beads were injected in the microfluidic platform and exposed to detection oligo, resulting in a rapid increase of the fluorescent signal that will disappear upon injection of the toehold single stranded DNA as shown in figure 3.26a. The binding kinetics matches the one observed in the previous paragraph in the absence of immunoassay (less than two minutes for DNA hybridization and separation), confirming that the presence of antibodies does not introduce steric hindrance issues. To assess the dynamic range of the assay a dose response study was performed off-chip (figure 3.26b) and validated the efficient detection of cystatin C over a wide range detection range, from 100 ng/mL to 10'000 ng/mL.

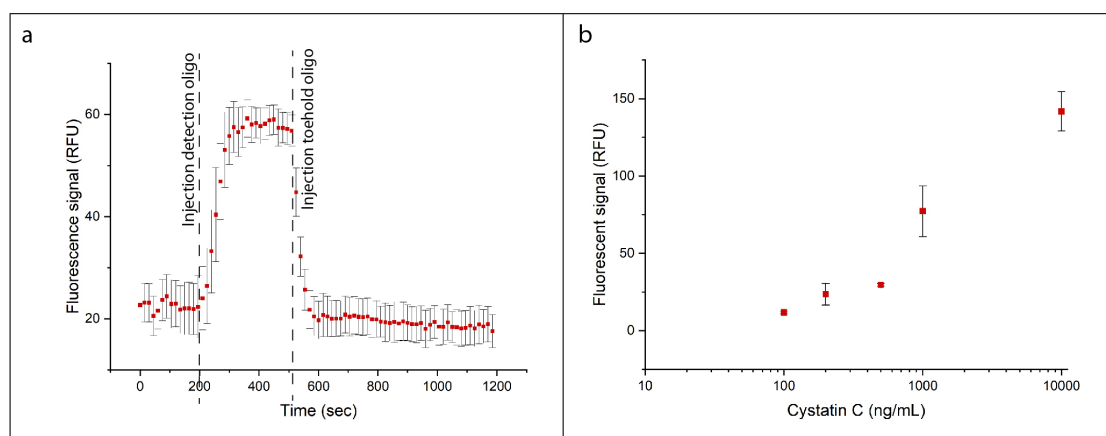


Figure 3.26: **On-chip and off-chip characterization of the full assay using single stranded DNA conjugated to antibodies for the detection of Cystatin C** (a) The sandwich immunoassay was performed off-chip with a Cystatin C concentration of 1000 $\mu\text{g/mL}$ and a 15 minutes incubation step. Then the beads were immobilized on-chip and sequentially exposed to the CAC detection sequence (increase of fluorescence) and the CAC toehold sequence (fluorescence drop). (b) In order to asses the dynamic range of the assay a dose response response was performed off-chip with a Cystatin C concentration ranging from 100 ng/mL to 10'000 ng/mL.

This demonstrates the pertinence of our platform for fast and multiplexed biomarker screening in a very low volume of patient sample. Indeed, beads targeting various analytes can be placed for off-chip incubation in a low volume of sample, less than 100 μL , and depletes the sample from target molecules. Subsequently, beads can be retrieved via centrifugation and injected in our microfluidic device for readout. We estimate that this approach could permit the detection of 10 analytes in less than an hour with a blood prick volume. Furthermore, the flexibility granted by the combination of beads-based immunoassays and DNA barcodes permits the implementation of highly personalized diagnosis. A practitioner could choose among a pool of available beads which marker to test and run a screening tailored to the specific patient symptoms. Our solution is thus more flexible than existing technologies relying on multiplexed lateral flow assays such as the Alere Triage [109], for which the targeted markers can not be modified after fabrication.

3.3 Summary and conclusion

In this chapter we present two bead-based approaches for the diagnosis of various disorders. The first platform presented in section 3.1 is focusing on the detection of acute conditions. The introduction of high aspect-ratio vertical electrodes within the microfluidic channel resulted in an accurate manipulation of antibodies-decorated beads through a novel method named “DEP surfing”. The incubation step was conducted in a dedicated area under a high flow rate, ensuring an effective collection of analytes on the surface of beads, an important feature for the detection of analytes at low concentration. We introduced the possibility to perform in the same microchamber, while in two successive steps, sample beads’ incubation and beads’ accumulation, controlled solely by electrical signals. We employed this approach to the concomitant detection of two analytes, thanks to a size-based and channel-based beads’ separation technique: NGAL and Cystatin C could be simultaneously detected within 15 min in a minimally diluted matrix, and the detection performance matched the one of a commercial ELISA kit. The combined detection of both biomarkers allows for the diagnosis of AKI conditions at different stages, which could be greatly beneficial to patients in intensive care units. The second device, introduced in section 3.2, targets a rapid and highly multiplexed detection of biomarkers in low sample volume, for instance in the context of clinical screening. We adapted the classical sandwich immunoassays with a new quantification procedure relying on the sequential injection of DNA strands decorated with fluorophores, the elimination of unwanted signal was successfully carried out thanks to an innovative use of toehold-mediated isothermal strand displacement. The future of this project lays in the implementation of the assays for the rapid detection of numerous markers.

4 Assessment of the phenotypic impact of microfluidics and DEP effects on single-cells

Disclaimer: The work presented in this chapter is partially adapted from the following article:

Thiriet, P.-E.; Pezoldt, J.; Gambardella, G.; Keim, K.; Deplancke, B.; Guiducci, C. Selective Retrieval of Individual Cells from Microfluidic Arrays Combining Dielectrophoretic Force and Directed Hydrodynamic Flow., *Micromachines*, 2020

My contribution: Conceptualization, Methodology, validation, investigation, writing and editing.

The cell biology community has very early on sensed the tremendous potential of microfluidic for cell-related applications. Indeed, most cell cultures have been carried out in petri dishes or flasks over the last decades, reducing cell-environment interactions to its simplest form and limiting cells functionalities and phenotypes. The introduction of microfluidic channels permits to mimic more accurately the dynamic condition experienced by the cells in living organisms. A good understanding of the relationship between cell culture parameters and the micro-environment created in the microfluidic channel can greatly contribute to the development of efficient platforms for cell culture [150]. The high versatility in the microfluidic systems design allow to sequentially expose cells to sets of reagents and to precisely tailor the dimensions and properties of the channel to manipulate cells with sizes ranging from small lymphocytes [43] to large oocytes [151]. Among many other applications Vedel et al. could study single-cell mobility behavior by means of a microfluidic device. The impact of microfluidics on cell biology went far beyond the cell culture studies solely, as the technology was also extensively employed for cell sorting and analysis. In such configuration microfluidic channels were associated with various sensing approaches such as optical [152] or electrical

Chapter 4. Assessment of the phenotypic impact of microfluidics and DEP effects on single-cells

readout [14]. The isolation of rare cells such as circulating tumor cells (CTCs) also greatly benefited from microfluidic technologies with the development of several platform sorting CTCs with a high efficiency [60, 153]. Gosset et al. [154] introduced a platform that could distinguish native populations of leukocytes and malignant cells through single-cell hydrodynamic stretching. Kimmerling et al. [64] compared intra- and inter-lineage transcriptomes within a cell population by capturing multiple generations of a single starting cell in subsequent traps.

DEP is one of the tools that can help unveil biological mechanisms in a label free manner. As it relies on interaction between charges present in the cells and external electric fields it provides information about the cells' dielectric properties. Flanagan et al. [155] successfully implemented a DEP-based system that could sort neural stem cells from their differentiated progeny. Yang et al. [156] combined DEP actuation and immunoassays to perform accurate capture of listeria bacteria. DEP could also be implemented in the scope of electro-rotation to differentiate cell populations [29].

The on-chip analysis of single-cells has recently raised significant interest upon the appearance of personalized therapies such as adoptive cell transfer [157]. Such approach relies on the administration to the patient of its own immune cells selected for their anti cancer activity [158]. The selection of immune cells in microfluidic devices via exposure to activation mediator bears a high potential in the context of adoptive cell transfer therapies [43]. The possible re-injection in a patient of cells following their selection in a microfluidic system reveals the urge to understand the impact of such devices on the cells phenotype. Our platform for single-cell handling relies on both fluidic restrictions and DEP actuation, consequently we will focus in this chapter on their impact on cellular phenotypes. Lu et al. [159] studied the functional impact of DEP on neural stem cells, suggesting short exposure of cells to DEP was harmless to neural cells. Nerguizian et al. [53] on the other hand noticed that long exposure to DEP forces would change the cell metabolism and RNA regulation. In this chapter, we propose to investigate through mRNA sequencing the phenotypic impact of our DEP-based platform on a T-lymphocyte population, a study that takes place in the context of the development of new tools for immunotherapy.

4.1 Single cell sequencing

RNA sequencing analysis is commonly carried out to measure transcripts of a cell population. However, it lacks the ability to discriminate different types of cells when analysing a bulk population [160]. In order to get a more accurate picture of the cell phenotype with a cellular resolution single-cell sequencing was introduced in the early 2010 [161], it has the power to grasp cell heterogeneities within cell populations [162]. In the scope of this chapter, single-cell sequencing tools were employed to assess the impact of our DEP-actuated microfluidic platform for single-cell trapping and recovery. The sequencing was performed using the Drop-seq method introduced by Macosko et al. [163] in 2015. The implementation of Drop-seq relies on four main steps, here presented in figure 4.1. First, the tissue has to be dissociated

into a viable single-cell suspension (i), then, each cell is encapsulated in a droplet containing a bead carrying a unique DNA barcode (ii). In this droplet, the cell is lysed and its mRNA binds to the primers of its associated bead (iii). Upon droplet breaking mRNA is reverse-transcribed into cDNA to create a set of “single-cell transcriptomes attached to microparticles” (STAMPs) (iv). The obtained STAMPs can then be amplified through PCR and sequenced to quantify the transcriptome of the cells singularly thanks to the presence of the DNA barcode associating each DNA strand with its origin cell (v).

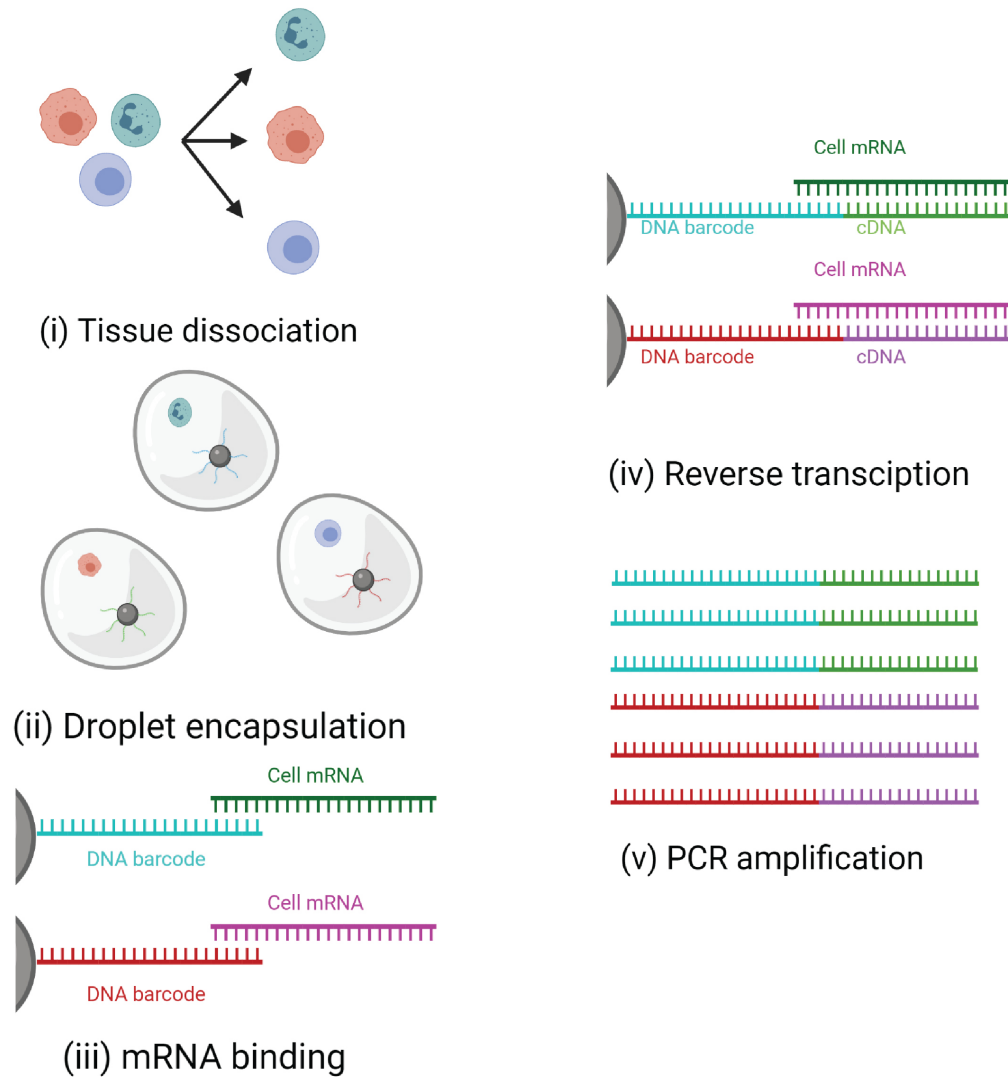


Figure 4.1: Schematic description of the Drop-seq methodology The complex tissue is dissociated into single-cell suspension (i). Each cell is encapsulated in a droplet with a DNA barcoded bead (ii). After lysis of the cell the mRNA strands are captured by the microparticles (iii). The emulsion is then broken and the mRNA is reverse-transcribed into cDNA (iv). The obtained DNA strands are amplified through PCR and sequenced (v).

4.2 Experimental design and methodology

4.2.1 Experimental design

Our approach of a system for single cell trapping and selective recovery has been described in chapter 2. The aim of this section is to investigate the impact of our system on the cell transcriptome. Indeed, as the cells recovered from the platform should be amenable to be further analyzed or potentially expanded for adoptive transfer, the impact of the microfluidics operation and the applied electric field on cell function needs to be assessed. To globally inspect the molecular changes to the cell, we analyzed their transcriptome using RNA-sequencing in the framework of DEP manipulation. The experimental plan we implemented is presented in figure 4.2. In order to determine whether the microfluidics setup or the applied DEP impact their molecular properties, Jurkat T-cells were injected and either passed through the microfluidics setup for an average duration of three minutes in absence or in the presence of DEP forces. After retrieval, cells were collected and cultured off chip for three hours to permit potential alterations by the DEP field or the fluidic forces to be represented transcriptionally. Input cells that were solely cultured served as negative control (Input), while cells cultured for three hours under Phorbol-12-myristate 13-acetate and Ionomycin activation (PMA/Iono), globally activating transcription based on protein kinase C (PKC) activation and calcium ion influx [164], served as positive control for global T-cell. Due to the low number of maximally 400 cells per sample and the high volume, 100 μ l, of cell culture medium, we employed mRNA capture beads to obtain the mRNA of the lysed cells and detected over 7600 genes across the experimental conditions. The sequencing of the cells and analysis of transcriptomic was carried out in collaboration with Joern Pezoldt from the Laboratory of Systems Biology and Genetics in EPFL, the methodology of the sequencing is described in the following section.

4.2.2 Sequencing methodology

Library preparation

Recovered cells (approximately 400) were centrifuged at 600 g for 5 min and the supernatant was replaced with 25 μ l of PBS containing 0.01% bovine serum albumin (Sigma, Kanagawa, Japan). Subsequently, 25 μ L of lysis buffer was added, containing 0.1% Sarkosyl (Sigma), 5 mM EDTA (Life Technologies, Carlsbad, CA, USA), 0.1 M Tris (pH 7.5, Sigma) and 25 mM 1,4-Dithiothreitol (DTT, Sigma), 800 units/mL RNase inhibitor (NEB, Ipswich, MA, USA) and 500 Drop-seq beads (Beads, Lot 120817, ChemGenes, Wilmington, MA, USA). All bead pelleting steps were carried out at 1000 g for 1 min in 1.5 mL microtubes (Axygen, Union City, CA, USA). Reverse transcription (RT), exonuclease I (ExoI) treatment and PCR were performed as described by Macosko et al. with minor adaptations [163]. Lysed cells were incubated at 1400 rpm for 5 min at room temperature and subsequently washed twice with 1 mL of 6x SSC buffer (Sigma). Reverse transcription was performed for 90 min at 42 °C in 50 μ l of 1 mM dNTPs (Clontech, Mountain View, CA, USA), 2.5 μ M template switch oligo (see Table 4.1), 1250

units/mL RNase inhibitor, 1x Maxima RT buffer and 10,000 units/mL Maxima H minus reverse transcriptase (Thermo Fisher Scientific, Waltham, MA, USA). Drop-seq beads were washed twice with 0.5% SDS (Applichem, Omaha, NE, USA) in 10 mM Tris (TE-SDS), twice with 0.01% Tween-20 (Sigma) in 10 mM Tris (TE-TW) and once with 10 mM Tris pH 7.5. The Drop-seq bead pellet was then incubated with 50 μ L of exonuclease mix containing 1x Exonuclease I Buffer and 1000 units/mL Exonuclease I (NEB) and incubated at 37 °C for 45 min at 1400 rpm). Drop-seq beads were washed twice with TE-SDS, twice with TE-TW and once with double-distilled H₂O. Beads were amplified by PCR in 25 μ L of 1x Hifi HotStart Readymix (Kapa Biosystems, Wilmington, MA, USA) and 0.8 μ M TSO-PCR primer (Table 4.1) at 95 °C for 3 min; 4 cycles of: 98 °C for 20 sec, 65 °C for 45 sec, 72 °C for 3 min; then, 16 cycles of: 98 °C for 20 sec, 67 °C for 20 sec, 72 °C for 3 min and an extension step of 5 min. Libraries were purified using Ampure XP beads (at a ratio of 0.6x to remove small fragments), cDNA was quantified using a Qubit HS kit (Thermo Fisher Scientific) and integrity was analyzed on a Fragment Analyzer (Agilent). Libraries were prepared using in house-produced Tn5 loaded with adapters, as described [165]. Size selected and purified libraries were sequenced paired-end on a NextSeq 500 system (Illumina, San Diego, CA, USA) in High Output mode following recommendations from the original protocol (read 1—20 bp and read 2—50 bp) [163].

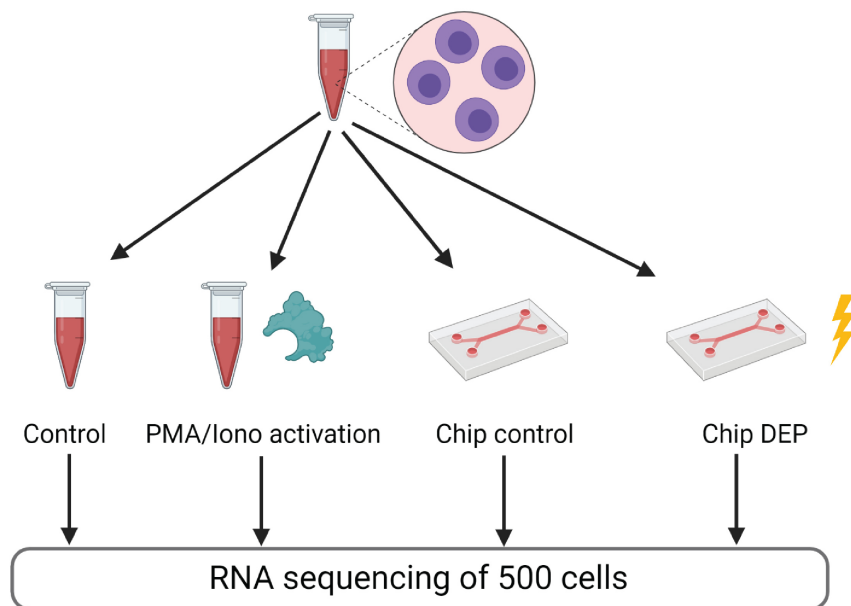


Figure 4.2: Experimental plan implemented to assess the impact of our microfluidic system on cell phenotype Jurkat cells were either injected into the microfluidics chip (Chip-Ctrl) or additionally subjected to the electric field used for accurate capture and retrieval of cells (Chip-DEP). Controls were either the input cells (Input) or cells activated for three hours under Phorbol-12-myristate 13-acetate and Ionomycin activation (PMA/Iono). Cells from all conditions were cultured for three hours to permit transcriptional changes to take place subsequent to treatment.

Chapter 4. Assessment of the phenotypic impact of microfluidics and DEP effects on single-cells

ref ID	Sequence
TSO	AAGCAGTGGTATCAACGCAGAGTGAATrGrGrG
TSO-PCR	AAGCAGTGGTATCAACGCAGAGT

Table 4.1: **Primers used for reverse transcription and library preparation.**

Data analysis

The data analysis was performed using the Drop-seq tools package on the EPFL SCITAS HPC platform. After trimming and sequence tagging, reads were aligned to the human reference genome (hg38) using STAR (version 2.7.0.e) [166]. Following the alignment, the gene annotation was added, bead synthesis errors were corrected, and cell barcodes extracted. Subsequently, the BAM files containing the processed data were used to obtain digital gene expression matrices. Only cell barcodes with at least 50 UMI (Unique Molecular Identifier) were retained. Downstream data analysis was carried out using R (version 3.5.0), with DESeq2 (version 1.22.2) [167] for identifying differentially expressed genes in pair-wise comparison. Plots were generated using the R package ggplot2 (version 3.0.0). The Gene Expression Omnibus (GEO) accession number for the RNA-seq data reported in this thesis is GSE143190.

4.3 Viability assessment

The viability of cells upon injection in the microfluidic system is a critical parameter that requires investigation prior to sequencing results analysis. To this end, we performed a viability assessment of the lymphocytes through analysis of cDNA quality and mitochondrial gene analysis, whose results are presented in figure 4.3. Figure 4.3a describes the amount of cDNA that has been obtained after cell lysis and reverse transcription highlights. It is important to notice that cDNA quality was similar across the conditions with marginally higher yield for “PMA/Iono”-activated cells. Additionally, the hierarchical clustering of the detected mitochondrial genes described in figure 4.3 revealed that cells processed with our platform showed similar expression intensities as compared to unprocessed cells. Such outcome confirms previous results on cell viability and dielectrophoresis, suggesting a minor impact of DEP on cell viability under one minute of exposure to electrical fields [168–170]. However, such studies apply DEP force on cells suspended in low conductivity medium. Performing experiments in high conductivity medium suggested a stronger impact on cells with a decrease of the survival rate [171] that could be attributed to the formation of peroxide within the cell culture medium [172]. In our case, despite the use of high conductivity medium, the cells were exposed to DEP for a much shorter duration, explaining the relative low impact observed on viability.

4.4 Transcriptional profiling of cells injected in our microfluidic platform

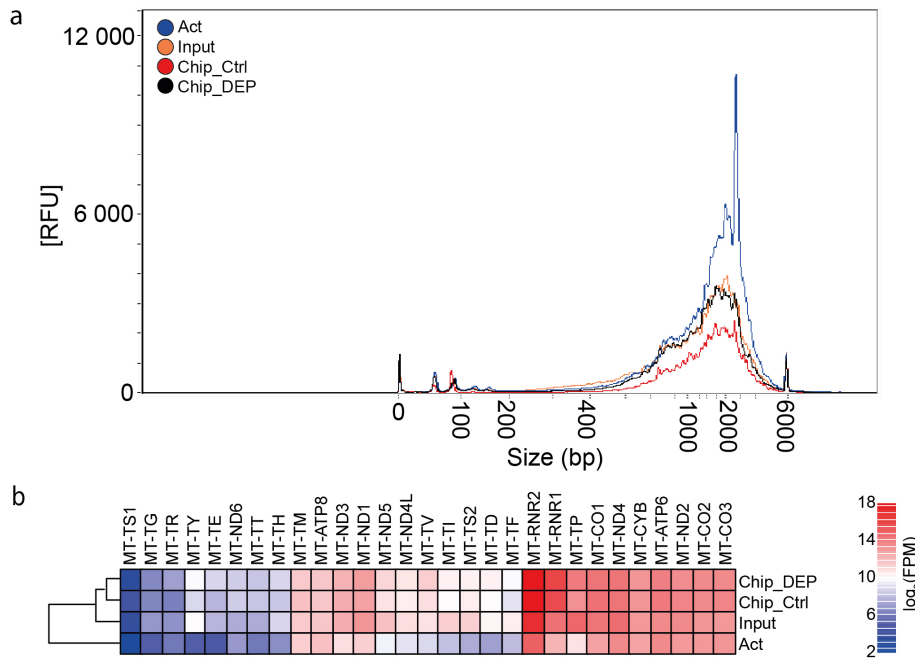


Figure 4.3: **Viability study of the lymphocytes exposed to the DEP-based microfluidic system** Jurkat cells were either injected into the microfluidics chip (Chip-Ctrl) or additionally subjected to the electric field used for accurate capture and retrieval of cells (Chip-DEP). Controls were either the input cells (Input) or cells activated for three hours under Phorbol-12-myristate 13-acetate and Ionomycin activation (PMA/Iono). Cells from all conditions were cultured for three hours to permit transcriptional changes to take place subsequent to treatment. a) Fragment analyzer profile of cDNA libraries. b) Hierarchical clustering of expression of mitochondrial genes.

4.4 Transcriptional profiling of cells injected in our microfluidic platform

The sequencing protocol described section 4.2.1 was carried out in the Laboratory of Systems Biology and Genetics at EPFL. Outcomes graphs are depicted in figure 4.4. Principal component (PC) analysis on all differentially expressed genes (DEGs) presented in 4.4a revealed that the first PC1 segregated “PMA/Iono”-activated cells from all other experimental conditions, whereas PC2 separated untreated cells from those subjected to the microfluidics chip. Importantly, there was no defined separation between cells subjected to DEP (Chip-DEP) or solely injected in the chip (Chip-Ctrl), suggesting minor transcriptional changes induced by the application of DEP forces. Figure 4.4b shows the difference in gene expression in various experimental conditions. The high concordance between “Chip-DEP” and “Chip-Ctrl” was underscored by the observation that no DEG could be detected, whereas 75 or 61 DEGs

Chapter 4. Assessment of the phenotypic impact of microfluidics and DEP effects on single-cells

were identified when comparing “PMA/Iono” cells to “Chip-Ctrl” or “Chip-DEP”, respectively. Importantly, the number of DEGs when comparing “Chip-Ctrl” or “Chip-DEP” to the “Input” conditions was substantially lower with 14 or 24, respectively.

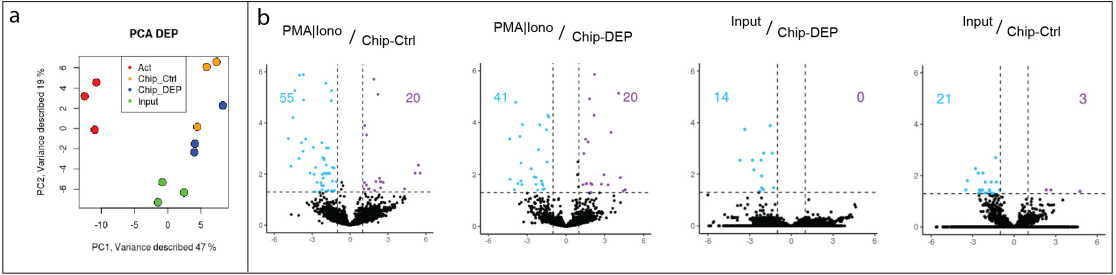


Figure 4.4: Transcriptional profiling of cells injected in the microfluidic device (a) Principal component analysis on all differentially expressed genes (number of DEGs: 117). PC1 segregates “PMA/Iono”-activated cells from other experimental conditions, while PC2 separates untreated control cells from those subjected to the microfluidics chip (b) Volcano plots of mean RNA-seq FPM (Fragment Per Million) comparing indicated samples. The number of DEGs is indicated.

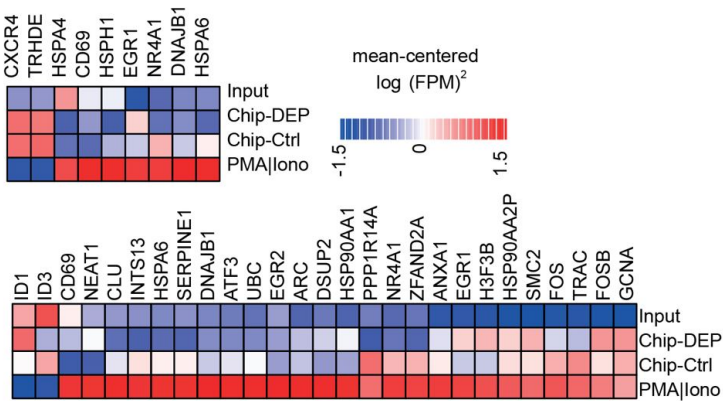


Figure 4.5: Investigation of gene expression upon application of DEP forces Heatmaps represent expression of selected DEGs. Left: DEGs between PMA/Iono-stimulated and Input cells. Right: DEGs common on comparing Chip-Ctrl and Chip-DEP to PMA/Iono-stimulated cells. Experiments were performed in three independent biological replicates. DEG, differentially expressed gene (absolute(log2[foldchange]) ≥ 1 and padj. ≤ 0.05).

Figure 4.5 presents the singular gene expression profile for each of the above-mentioned cell population. From this study it appears that genes associated with stress responses such as heat-shock proteins, HSPA6 and HSP90AA1, chaperons like CLU and genes involved in stress recovery responses including DNAJB1 and Ubiquitin (UBC) were significantly upregulated only under “PMA/Iono” conditions (Figure 4.5, down). Interestingly, a minor proportion of genes was upregulated for “PMA/Iono” and both Chip conditions, encompassing predominantly genes involved in cell proliferation including EGR1, SMC2, FOS and FOSB or activation

TRAC and H3F3B (Figure 4.5, down). When comparing the genes consistently differentially expressed between PMA/Iono-activated cells and cells injected into the chip, the vast majority of activation and stress response genes was upregulated solely under “PMA/Iono” condition, whereas CXCR4 expression was only upregulated in cells that were flown through the chip (Figure 4.5, up).

4.5 Summary and conclusion

Based on these transcriptional profiling results, we conclude that the impact of injection into and extraction from the microfluidics chip outweighs the changes wrought by the electric field onto the transcriptional landscape of the cell under the implemented culture conditions. This could be in part due to the very confined DEP, permitting the utilization of a low voltage of 8 Vpp at frequencies of 20 MHz, thereby limiting the extent of transcriptional changes observed in a previous study [53]. Furthermore, it was previously shown that the application of negative DEP, as utilized in our system, does not alter the viability or differentiation capacity of neuronal embryonic stem cells, even at long DEP exposure times of up to 30 min [159], which exceeds by far the pulsed approach we implemented. Although the transcriptional alterations instigated within our platform are minor, as compared to global activation of the cell, and unavoidable when implementing microfluidic cell handling, special care should be taken to minimize stressors such as high pressure or long retention times within the microfluidic devices. Regardless, application of short-term DEP for accurate retrieval of cells does only minimally impinge on the transcriptome at the obtained resolution. It is also worth to notice that this is the first time phenotypical effects induced by microfluidics and DEP were characterized separately, showing that the changes triggered by handling the cell in the microfluidic device outweigh the changes caused by the electrical field.

5 Perspectives

The work presented in the scope of this thesis highlighted various contributions in the development of new tools for biologists and clinicians. The aim of this chapter is to describe and discuss the future directions of the project we worked on and what might be the new challenges to overcome.

5.1 DEP-based manipulation of beads

5.1.1 Towards a Point-Of-Care platform

The device presented in chapter 3 for AKI diagnosis is able to detect two biomarkers within a short time. We aim to adapt the current system to make it fully autonomous and point-of-care. The implementation of DEP-based actuation avoids the use of magnets, a good asset to miniaturize the system in a compact case. However, our platform still relies on active pumping to perform sequential injections of beads and reagents. In our path to automatize the tool and limit operator-based handling of reagents we plan to implement two novel features to our platform, namely capillary pumping and storage of dried beads in the chamber prior to analysis.

Capillary-based immunoassays have proven their value to carry reagent in microfluidic channels [173–176]. They simplify the incorporation of reagents in the microfluidic channel and allow for the development of compact and affordable point-of-care systems. In the scope of our project, capillary pumping will be implemented as shown in figure 5.1. The sample would be first delivered on a loading pad connected to the main channel, that is crowded with micro-structured features to drive the flow at a desired speed, and will then migrate through the channel. However, since the volume of the microfluidic chamber (around $5\mu\text{L}$) is not sufficient to run the entire assay, an absorbent pad will be integrated at the exit of the chip to drag the liquid in the channel, a solution inspired by standard lateral flow assays. The flow in the main channel depends on the pore size of the paper mesh, therefore, it has to be tailored to enable the efficient retention of microbeads in the incubation areas.

One of the main challenge in the integration of capillary pumping will be to maintain a steady fluid velocity in the microfluidic channel during the entire duration of the assay. Indeed, fluid

velocities in a capillary-driven microfluidic channel typically exhibit an exponential decay [177].

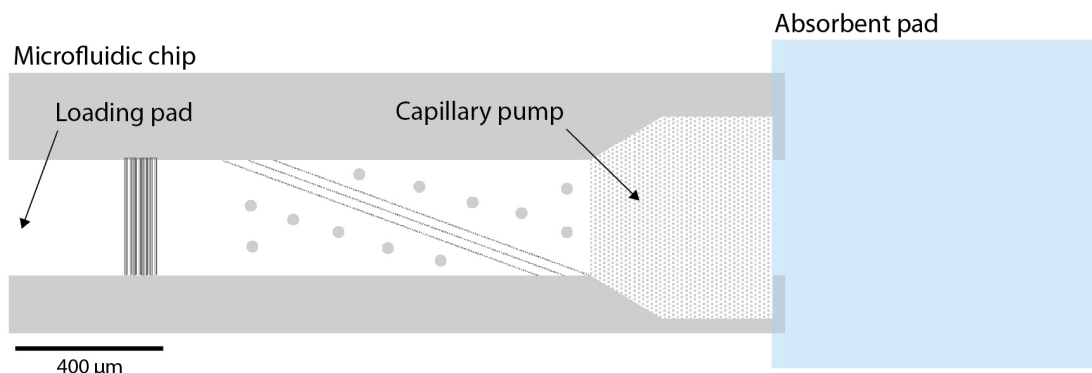


Figure 5.1: **New layout for capillary pumping in our AKI detection platform** The sample is injected through a loading pad, then fills the main channel and the capillary pump at a high flow rate, and finally is dragged out of the system by the absorbent pad setting the flow rate in the channel for most of the assay duration. Credit to Gloria Porro for the picture.

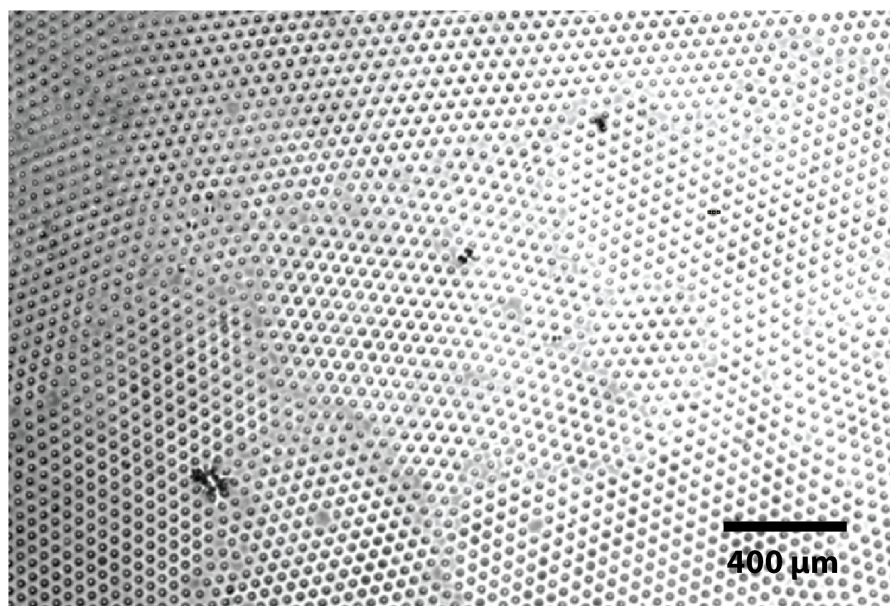


Figure 5.2: **Microbeads dried in a trehalose solution** The dried beads self-arranged themselves regularly and appear to be homogeneously distributed on the surface of the glass slide . Credit to Gloria Porro for the picture

Another relevant strategy in the context of automatizing our device is the pre-loading of beads in the microfluidic channel. Drying reagents can be a pertinent strategy in the context of point-of-care testing, since refrigeration might not be available in all settings [178]. Moreover, drying prevents the degradation of proteins , ensures better performance of the device and is

commonly encountered in the manufacturing of lateral flow assays to integrate the antibody-coated microbeads in the conjugate pad [83]. It mainly relies on the use on hydrophilic components, such as surfactants, proteins and/or saccharides, that act as releasing agents and prevent the microbeads from sticking together. Figure 5.2 depicts microbeads dried in a solution containing 60% of a sugar named trehalose, upon drying the microbeads formed self-assembled structure evenly dispersed and could be resuspended without significant decrease of their biological activity.

5.1.2 Low-volume sample detection

The ability to detect analytes with a low volume of sample is a critical asset of PoC devices [179]. Indeed, non-invasive sample collection methods such as finger pricking are often more suitable for testing in emergency settings as they require less skilled operators and little to none infrastructures [178]. Low volume analysis is also a concern for scientists working with small lab animals, such as mice, especially in their early development stages [180]. The average volume collected in adult patients with a finger prick ranges from 50 to 100 μL [181]. After the 5-times dilution performed to ensure efficient manipulation of microbeads by DEP forces, the obtained volume to be injected in our device would range from 250 to 500 μL . Assuming that the average flow for beads incubation and accumulation in the chip is set at 3 $\mu\text{L}/\text{min}$ and that the total analysis time is 20 minutes we can deduce that we need around 60 μL of diluted sample to carry out the assay. The current dead volume of the set-up is estimated at 100 μL , mainly due to long tubing and large microfluidic connectors. It adds up to a total analysis volume of near 160 μL per assay, which fits the volume provided by a blood prick. Nonetheless, the total analysis volume could be reduced through optimization of the tubing length and the microchannel design to enable the blood prick testing of younger patients, who are known to provide significantly lower amount of blood sample, from 5 to 15 μL [182].

5.1.3 Generation of microparticles' streams

The analysis of microparticles in-flow allows for high throughput data collection at the single-particle level and can contribute to unveil the heterogeneities of cell populations [183]. The performance of such systems is guaranteed by the accurate positioning of particles in the microfluidic channels. For instance, the well-established Fluorescence Activated Cell Sorting (FACS) technique relies on sheath flows to confine the cells on a specific path for laser interrogation [184]. Despite its efficacy and accuracy, this hydrodynamic focusing approach is complex and leads to bulky and expensive set-ups. The DEP-surfing concept introduced in this thesis for the accumulation of microbeads for signal amplification appears as a potential candidate for an easy focusing of microparticles. The DEP-based actuation permits indeed the focusing of particles in a specific path in the microfluidic channel. This eliminates the need of hydrodynamic-dedicated inlets and therefore simplify the microfluidic layout of the device. We varied the size of the particles, their types, namely cells or polystyrene, and the angle of the electrodes lines to validate that DEP surfing could be successfully implemented

in numerous different settings to deflect particles toward a specific path. Among the fields that could benefit from this innovation cell flow cytometry or droplet microfluidic raise as promising candidates.

5.2 Oligo-based platform for multiple markers screening

5.2.1 Highly multiplexed detection of markers

The work presented in chapter 3 paved the road for the development of a highly multiplexed diagnosis platform. The toehold approach permits the rapid exchange of reagents in the microfluidic channel and thus to perform several tests in a short duration. Also, the number of injections steps can be reduced by mixing the toehold, that removes the previously bound fluorescent barcode, with the new one. We can estimate a total analysis time of 3 minutes per marker, which translates in 10 markers in less than 30 minutes. In our protocol, the sandwich immunoassay is performed off-chip prior to the injection of beads in the microfluidic channel. All the immuno-complexes are thus formed simultaneously, and the injection of the beads in the microfluidic device only serves the readout purpose. The incubation done in a single mixture allows to perform the assay with a low volume of patient sample and for a time long enough, about 20 minutes, to maximize the output signal. One can then forecast the analysis of 10 markers with a patient sample as small as 100 μ L and in less than 2 hours, that will appear as a competitive solution compared to actual commercial systems.

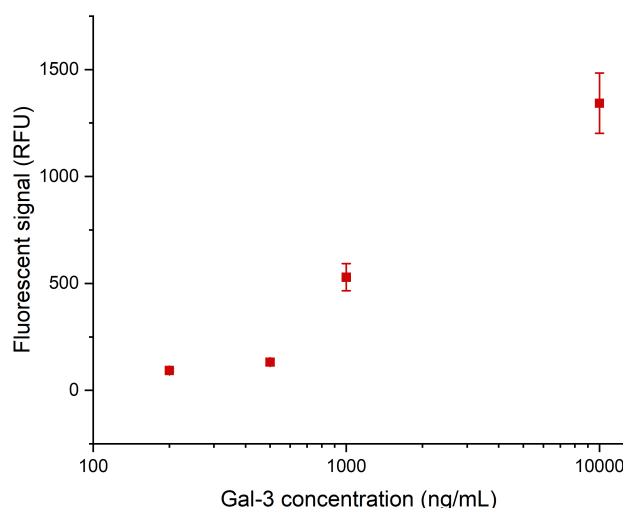


Figure 5.3: **Dose response curve for the off-chip detection of Galectin-3** The detection of Galectin-3 is performed in a standard sandwich immunoassay configuration in PBS supplement with 1% BSA, the limit of detection of the assay is about 500 ng/mL.

One of the applications of this system could be the screening of cancer biomarkers for early stage cancer diagnosis [185]. To this end we investigated the use of Galectin-3 (Gal-3) as a potential first marker for our platform. Gal-3 acts as a galactoside-binding protein involved in many biological processes such as cell adhesion, apoptosis, immunity and inflammation [186, 187]. It was also associated with gastrointestinal cancer [188]. Figure 5.3 presents the dose response curve obtained in a standard immunoassay configuration off-chip. The concentration that we could quantify matches the ranges observed in clinics with patients suffering from gastrointestinal cancer [189]. The combination of this marker with other established gastrointestinal cancer markers such as carcinoembryonic antigen (CEA) or cancer-related antigen 72-4 (CA 72-4) [190] would help improving the detection of these cancers in their early stages.

5.2.2 A new approach employing aptamers

Aptamers are single-strand DNA molecules that can bind to target proteins with high affinity and specificity [191]. Their nature as nucleic acids grants them a higher stability when compared to antibodies that are prone to denaturation. Despite an expensive selection process to determine the most suitable DNA sequence to bind the target, aptamers are cost-effective compared to antibodies since they can be synthesized with high reproducibility and at very low cost [192, 193]. On top of those benefits aptamers would be particularly suited for our platform as the DNA barcode used to identify each marker could be directly added to the DNA sequence of the aptamer prior to synthesis, upon ensuring that such sequence will not affect the conformation of the aptamer and its potency to bind the target epitope of the protein. Such approach would eliminate the step of conjugation between the DNA barcode and the detection antibody, and therefore substantially simplify the design of the immunoassays. However it is currently limited by the few available aptamers that have been tested in a sandwich configuration and by the reluctance of the scientific community to abandon the very successful antibodies [194]. The introduction of novel sequencing methods might simplify and decrease the cost of the selection, paving the road for a broader use of aptamers in the diagnosis field [195, 196].

5.3 Single cell handling platform

5.3.1 Reducing the footprint of a trapping unit to increase throughput

The single-cell immobilization and recovery device presented in chapter 2 section 2.2.2 can only process up to 16 single-cells simultaneously. While this is sufficient to validate the method of DEP-based actuation, it can not meet the requirement of most of single-cell screening applications that requires simultaneous analysis of hundreds of cells [61]. To achieve a higher throughput we propose to modify the trapping unit in order to reduce its footprint. The layout of the novel chip is presented in figure 5.4. The miniaturization of the traps consists in the

replacement of the long bypass channel by a U-shaped restriction as used in section 2.2.3 for single beads immobilization. 3D electrodes are added asymmetrically up- and down- stream to ensure an efficient release of cells. The asymmetry in the electrodes setting grants the application of a diagonal DEP force on the cell to be released (figure 5.4b) and allows to change its position with respect to the laminar flow lines. The reduced footprint of each trap allows to integrate around 2000 traps within the same area of the previous generation of the device. In order to actuate such a high number of traps electrodes interconnects have to be modified. We propose to integrate a row-column register in a two-dimensional matrix as frequently encountered in electronic circuits [197]. This methodology would allow to singularly address each trap and would limit the number of connecting pads for the chip.

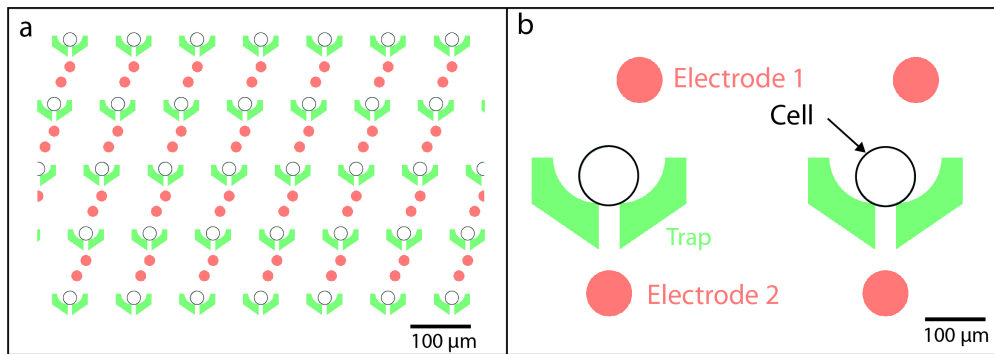


Figure 5.4: New layout for simultaneous trapping and selective release of multiple cells The implementation of U-shaped traps permits the integration of multiple traps with a limited footprint (a). Each trap is surrounded by 2 electrodes than are singularly addressable for a selective release, the asymmetry in the electrodes locations with regards to the trap ensure the creation of a diagonal DEP force to efficiently push the cell out of the trap.

5.3.2 Exposure to active components for in-situ single-cell analysis

The system presented in the section above could contribute to a better understanding of single-cell biology. mRNA sequencing could thus be employed for single-cell analysis to identify the activation state of single immune cells and thus have a better understanding of patients immune response [198]. Another possible application of such device would be the study of cell-cell interactions. Indeed, the ability to isolate cells in a controlled environment to analyze their interactions is a key asset for immunotherapies that rely on the selection on lymphocytes exhibiting specific properties against the tumor [199]. The U-shaped trapping structure can be easily adapted for the trapping of cell pairs according to the methodology proposed by Skelley et al. in 2009 [200].

Conclusion

Many biosensors rely on the interaction between two biological species to produce a measurable signal. The optimization of such interaction is thus crucial for the performance of analytic systems. From the introductory chapter of this thesis it appears clearly that the analyte collection at a probe surface strongly depend on incubation conditions. This thesis introduces new methods to perform incubation of single-cells and microbeads in an in-flow configuration inside a microfluidic channel.

The development of such platforms requires the improvement of existing microfabrication techniques. As the fabrication of devices combining microfluidic channels and electrically active components is long and tedious, we introduced several solutions for fast prototyping of microfluidic channels to validate the device's functionalities prior to fabrication of complex chips. The standing 3-D electrodes previously established by our team were embedded for the first time within the walls of microfluidic channel, allowing the introduction of extremely versatile systems combining electro-kinetic and fluidic approaches. Finally, we placed significant efforts to ensure the compatibility of our SU-8 microfluidic with standard PDMS valving system. To this end, we presented for the first time PDMS-based valves on top of SU-8 microfluidics, a solution that can be adapted to combine PDMS valves with any hard material microfluidic channels.

A prerequisite for on-chip incubation of microparticles such as cells or microbeads in a microfluidic channel is the ability to immobilize particles against the flow of reagents. We proposed several strategies to perform this retention. In the case of cells immobilization was carried out in hydrodynamic traps, guaranteeing minimal stress for the cells, while the release could be selectively achieved through DEP actuation for the first time in a standard culture buffer. Two distinct approaches were investigated for the trapping of polystyrene microbeads against a flow of reagents: the first relies on the use of DEP only for microbeads handling and exhibits a high versatility in the obtained trajectories with the possibility to implement size-based discrimination of particles. The introduction of high-aspect-ratio vertical electrodes within the microfluidic channel permitted an accurate manipulation of beads through a novel method named "DEP surfing". The second approach is based purely on hydrodynamic restriction and, while losing some of the flexibility offered by DEP actuation, it can withstand higher flow rates and benefits from a simple microfabrication procedure.

Conclusion

While studying on-chip incubation of particles the most immediate application appears to be the diagnostics field, for which more binding events directly translates into an increase of output signal. We explored this path with two microfluidic platforms, one DEP-based and another hydrodynamic-oriented. The first system could be successfully implemented to perform the simultaneous detection of NGAL and Cystatin C, two acute kidney injury biomarkers, within 15 minutes and in a minimally diluted buffer. In this platform the incubation was carried out in a dedicated area and matched the performance of a standard incubation in a turbulent regime. The combined detection of these two biomarkers allows for the diagnosis of AKI conditions at different stages, which could be greatly beneficial to patients in intensive care units. Furthermore, the technology we established could be easily readjusted for the detection of more analytes through the use of beads of different sizes. Since our system relies on the largely established biochemistry of antibody–beads' conjugation and on-sandwich assays, it can be easily translated to the analysis of other acute conditions or infectious diseases. The second device aims at providing a new solution for the rapid screening of multiple biomarkers. It replaces fluorescently labelled antibodies by DNA-barcoded antibodies that can be read sequentially upon injection of their complementary DNA strands. Various options have been explored for signal elimination following each readout, among which the use of toehold mediated strand displacement appeared the most suitable. It indeed grants an almost perfect elimination of unwanted signals in very short periods and permits a theoretical throughput of 20 markers per hour.

Cell studies can also massively benefit from efficient incubation protocols, especially if combined with retrieval protocols such as the one we introduced in chapter 2. However, prior to any assay implementation of assays on-chip we needed to investigate the impact of cells manipulation in a microfluidic set-up on their viability and phenotype to ensure that we were not harming them. To do so we started a collaboration with the laboratory of Systems Biology and Genetics at EPFL in order to assess the phenotypical impact of DEP actuation and microfluidic channels on T-lymphocytes. Transcriptional analysis of recovered cells revealed only marginal alteration of their molecular profile upon DEP application, underscored by minor transcriptional changes induced upon injection into the microfluidic device. Therefore, the established microfluidic system combining targeted DEP manipulation with downstream hydrodynamic coordination of single cells provides a powerful means to handle and expose individual cells to reagents within one device, and could be scaled-up to screen larger cell populations.

Bibliography

- [1] I. A. Darwish. "Immunoassay Methods and their Applications in Pharmaceutical Analysis: Basic Methodology and Recent Advances". In: *International Journal of Biomedical Science : IJBS* 2.3 (Sept. 2006), pp. 217–235. ISSN: 1550-9702.
- [2] R. E. Suri et al. "A neural network model with dopamine-like reinforcement signal that learns a spatial delayed response task". In: *Neuroscience* 91.3 (1999), pp. 871–890. ISSN: 0306-4522. DOI: 10.1016/s0306-4522(98)00697-6.
- [3] R. Shen et al. "High-throughput SNP genotyping on universal bead arrays". In: *Mutation Research* 573.1 (June 3, 2005), pp. 70–82. ISSN: 0027-5107. DOI: 10.1016/j.mrfmmm.2004.07.022.
- [4] E. Engvall et al. "Enzyme-linked immunosorbent assay (ELISA). Quantitative assay of immunoglobulin G". In: *Immunochemistry* 8.9 (Sept. 1971), pp. 871–874. ISSN: 0019-2791. DOI: 10.1016/0019-2791(71)90454-x.
- [5] S. Sakamoto et al. "Enzyme-linked immunosorbent assay for the quantitative/qualitative analysis of plant secondary metabolites". In: *Journal of Natural Medicines* 72.1 (2018), pp. 32–42. ISSN: 1340-3443. DOI: 10.1007/s11418-017-1144-z.
- [6] P. Risch et al. "Analytical Solution of the Time-Dependent Microfluidic Poiseuille Flow in Rectangular Channel Cross-Sections and Its Numerical Implementation in Microsoft Excel". In: *Biosensors* 9.2 (May 24, 2019), p. 67. ISSN: 2079-6374. DOI: 10.3390/bios9020067.
- [7] T. M. Squires et al. "Making it stick: convection, reaction and diffusion in surface-based biosensors". In: *Nature Biotechnology* 26.4 (Apr. 2008), pp. 417–426. ISSN: 1546-1696. DOI: 10.1038/nbt1388.
- [8] T. M. Squires et al. "Microfluidics: Fluid physics at the nanoliter scale". In: *Reviews of Modern Physics* 77.3 (Oct. 6, 2005). Publisher: American Physical Society, pp. 977–1026. DOI: 10.1103/RevModPhys.77.977.
- [9] H. C. Berg. *Random Walks in Biology*. Google-Books-ID: DjdgXGLoJY8C. Princeton University Press, Sept. 27, 1993. 168 pp. ISBN: 978-0-691-00064-0.
- [10] L. G. Leal. *Advanced Transport Phenomena: Fluid Mechanics and Convective Transport Processes*. Cambridge Series in Chemical Engineering. Cambridge: Cambridge University Press, 2007. ISBN: 978-0-521-84910-4. DOI: 10.1017/CBO9780511800245.

Bibliography

- [11] L. Armbrrecht et al. "Self-assembled magnetic bead chains for sensitivity enhancement of microfluidic electrochemical biosensor platforms". In: *Lab on a Chip* 15.22 (Oct. 2015), pp. 4314–4321. ISSN: 1473-0189. DOI: 10.1039/C5LC00796H.
- [12] X. Xu et al. "Optimization of microfluidic microsphere-trap arrays." In: 7.1 (2013), p. 14112. DOI: 10.1063/1.4793713.
- [13] J. B. Lee et al. "Innovative SU-8 Lithography Techniques and Their Applications". In: *Micromachines* 6.1 (Jan. 2015), pp. 1–18. DOI: 10.3390/mi6010001.
- [14] Z. Zhu et al. "Real-time monitoring of immobilized single yeast cells through multi-frequency electrical impedance spectroscopy". In: *Anal Bioanal Chem* 406.27 (2014), pp. 7015–7025. ISSN: 1618-2642. DOI: 10.1007/s00216-014-7955-9.
- [15] Y. Zhou et al. "Single cell studies of mouse embryonic stem cell (mESC) differentiation by electrical impedance measurements in a microfluidic device". In: *Biosens Bioelectron* 81 (2016), pp. 249–258. ISSN: 0956-5663. DOI: 10.1016/j.bios.2016.02.069.
- [16] E. Rollo et al. "Label-free identification of activated T lymphocytes through tridimensional microsensors on chip". In: *Biosens Bioelectron* 94 (Int. J. Mol. Sci. 16 2015 2017), pp. 193–199. ISSN: 0956-5663. DOI: 10.1016/j.bios.2017.02.047.
- [17] L. Amato et al. "Fabrication of high-aspect ratio SU-8 micropillar arrays". In: *Microelectronic Engineering*. Special issue MNE 2011 - Part II 98 (Oct. 1, 2012), pp. 483–487. ISSN: 0167-9317. DOI: 10.1016/j.mee.2012.07.092.
- [18] B. Gale et al. "A Review of Current Methods in Microfluidic Device Fabrication and Future Commercialization Prospects". In: (2018), p. 60. DOI: 10.3390/inventions3030060.
- [19] M. A. Unger et al. "Monolithic Microfabricated Valves and Pumps by Multilayer Soft Lithography". In: *Science* 288.5463 (Apr. 2000), pp. 113–116. ISSN: 0036-8075, 1095-9203. DOI: 10.1126/science.288.5463.113.
- [20] N. Shembekar et al. "Droplet-based microfluidics in drug discovery, transcriptomics and high-throughput molecular genetics". In: *Lab on a Chip* 16.8 (2016), pp. 1314–1331. DOI: 10.1039/C6LC00249H.
- [21] Z. Swank et al. "A high-throughput microfluidic nanoimmunoassay for detecting anti-SARS-CoV-2 antibodies in serum or ultralow-volume blood samples". In: *Proceedings of the National Academy of Sciences* 118.18 (May 2021). ISSN: 0027-8424, 1091-6490. DOI: 10.1073/pnas.2025289118.
- [22] D. Carlo et al. "Dynamic Single-Cell Analysis for Quantitative Biology". In: *Anal Chem* 78.23 (2006), pp. 7918–7925. ISSN: 0003-2700. DOI: 10.1021/ac069490p.
- [23] S. Einav et al. "Discovery of a hepatitis C target and its pharmacological inhibitors by microfluidic affinity analysis". In: *Nature Biotechnology* 26.9 (Sept. 2008), pp. 1019–1027. ISSN: 1087-0156, 1546-1696. DOI: 10.1038/nbt.1490.

- [24] M. Ionescu et al. "Enhanced biocompatibility of PDMS (polydimethylsiloxane) polymer films by ion irradiation". In: *Nuclear Instruments and Methods in Physics Research Section B: Beam Interactions with Materials and Atoms*. 20th International Conference on Ion Beam Analysis 273 (Feb. 2012), pp. 161–163. ISSN: 0168-583X. DOI: 10.1016/j.nimb.2011.07.065.
- [25] J. M. Buriak. "Functionalization of Silicon Surfaces for Device Applications". In: *JALA: Journal of the Association for Laboratory Automation* 4.3 (June 1, 1999). Publisher: SAGE Publications Inc, pp. 36–39. ISSN: 1535-5535. DOI: 10.1016/S1535-5535-04-80009-1.
- [26] V. Faustino et al. "Biomedical microfluidic devices by using low-cost fabrication techniques: A review". In: *Journal of Biomechanics*. Selected Articles from the International Conference on CFD in Medicine and Biology (Albufeira, Portugal – August 30th - September 4th, 2015) 49.11 (July 2016), pp. 2280–2292. ISSN: 0021-9290. DOI: 10.1016/j.jbiomech.2015.11.031.
- [27] Y. Chen et al. "Conformal coating of parylene for surface anti-adhesion in polydimethylsiloxane (PDMS) double casting technique". In: *Sensors and Actuators A: Physical* 189 (Jan. 15, 2013), pp. 143–150. ISSN: 0924-4247. DOI: 10.1016/j.sna.2012.09.024.
- [28] P. Moni et al. "Vapor deposition routes to conformal polymer thin films". In: *Beilstein Journal of Nanotechnology* 8 (Mar. 28, 2017), pp. 723–735. ISSN: 2190-4286. DOI: 10.3762/bjnano.8.76.
- [29] K. Keim et al. "On-chip technology for single-cell arraying, electrorotation-based analysis and selective release." In: *Electrophoresis* 40.14 (2019), pp. 1830–1838. ISSN: 0173-0835. DOI: 10.1002/elps.201900097.
- [30] M. Xavier et al. "Size and dielectric properties of skeletal stem cells change critically after enrichment and expansion from human bone marrow: consequences for microfluidic cell sorting". In: *Journal of The Royal Society Interface* 14.133 (Aug. 31, 2017). Publisher: Royal Society, p. 20170233. DOI: 10.1098/rsif.2017.0233.
- [31] C. M. Yousuff et al. "Microfluidic Platform for Cell Isolation and Manipulation Based on Cell Properties". In: *Micromachines* 8.1 (Jan. 4, 2017), p. 15. ISSN: 2072-666X. DOI: 10.3390/mi8010015.
- [32] D. Wu et al. "Electrophoretic separations on microfluidic chips". In: *Journal of Chromatography. a* 1184.1 (Mar. 14, 2008), pp. 542–559. ISSN: 0021-9673. DOI: 10.1016/j.chroma.2007.11.119.
- [33] H. Zhang et al. "DEP-on-a-Chip: Dielectrophoresis Applied to Microfluidic Platforms". In: *Micromachines* 10.6 (June 2019). Number: 6 Publisher: Multidisciplinary Digital Publishing Institute, p. 423. DOI: 10.3390/mi10060423.
- [34] S. C. Kilchenmann et al. "Metal-coated silicon micropillars for freestanding 3D-electrode arrays in microchannels". In: (2013), pp. 713–719. ISSN: 0925-4005. DOI: 10.1016/j.snb.2013.05.037.

Bibliography

- [35] M. Islam et al. "Enrichment of diluted cell populations from large sample volumes using 3D carbon-electrode dielectrophoresis". In: *Biomicrofluidics* 10.3 (May 1, 2016). Publisher: American Institute of Physics, p. 033107. DOI: 10.1063/1.4954310.
- [36] J.-W. Choi et al. "3-dimensional electrode patterning within a microfluidic channel using metal ion implantation". In: *Lab Chip* 10.6 (2010), p. 783. ISSN: 1473-0197. DOI: 10.1039/B917719A.
- [37] S. C. Kilchenmann et al. "Metal-Coated SU-8 Structures for High-Density 3-D Micro-electrode Arrays". In: *J Microelectromech S* 25.3 (2016), pp. 425–431. ISSN: 1057-7157. DOI: 10.1109/JMEMS.2016.2539000.
- [38] M. Seifert et al. "Capability Study of Ti, Cr, W, Ta and Pt as Seed Layers for Electrodeposited Platinum Films on -Al₂O₃ for High Temperature and Harsh Environment Applications". In: *Materials* 10.1 (Jan. 11, 2017), p. 54. ISSN: 1996-1944. DOI: 10.3390/ma10010054.
- [39] I. D. Raistrick. "Application of Impedance Spectroscopy to Materials Science". In: *IMPEDANCE SPECTROSCOPY* (), p. 30.
- [40] Y. Zhou et al. "Dynamic monitoring of single cell lysis in an impedance-based microfluidic device". In: *Biomed Microdevices* 18.4 (2016), p. 56. ISSN: 1387-2176. DOI: 10.1007/s10544-016-0081-z.
- [41] C. Iwakura et al. "Hydrogen–Metal Systems: Electrochemical Reactions (Fundamentals and Applications)". In: *Encyclopedia of Materials: Science and Technology*. Ed. by K. H. J. Buschow et al. Oxford: Elsevier, Jan. 2001, pp. 3923–3941. ISBN: 978-0-08-043152-9. DOI: 10.1016/B0-08-043152-6/00695-1.
- [42] M. Carminati et al. "Impedance Spectroscopy for Biosensing: Circuits and Applications". In: *Handbook of Biochips*. Ed. by M. Sawan. New York, NY: Springer New York, 2015, pp. 1–24. ISBN: 978-1-4614-6623-9. DOI: 10.1007/978-1-4614-6623-9_30-1.
- [43] E. Jammes et al. "High-throughput single-cell TCR - pMHC dissociation rate measurements performed by an autonomous microfluidic cellular processing unit". In: *bioRxiv* (July 2021), p. 2021.06.30.450499. DOI: 10.1101/2021.06.30.450499.
- [44] S. Huang et al. "Fabrication of micro pneumatic valves with double-layer elastic poly(dimethylsiloxane) membranes in rigid poly(methyl methacrylate) microfluidic chips". In: *J Micromech Microeng* 22.8 (2012), p. 085008. ISSN: 0960-1317. DOI: 10.1088/0960-1317/22/8/085008.
- [45] K. S. Lee et al. "Plastic–PDMS bonding for high pressure hydrolytically stable active microfluidics". In: *Lab Chip* 9.11 (2009), pp. 1618–1624. ISSN: 1473-0197. DOI: 10.1039/b820924c.
- [46] L. Armbrecht et al. "Recent Advances in the Analysis of Single Cells". In: *Anal Chem* 89.1 (2016), pp. 2–21. ISSN: 0003-2700. DOI: 10.1021/acs.analchem.6b04255.

-
- [47] C.-H. Lin et al. "A microfluidic dual-well device for high-throughput single-cell capture and culture". In: *Lab on a Chip* 15.14 (June 2015), pp. 2928–2938. ISSN: 1473-0189. DOI: 10.1039/C5LC00541H.
 - [48] M Sauzade et al. "Deterministic trapping, encapsulation and retrieval of single-cells". In: *Lab Chip* 17.13 (2017), pp. 2186–2192. ISSN: 1473-0197. DOI: 10.1039/C7LC00283A.
 - [49] A. Ozcelik et al. "Acoustic tweezers for the life sciences". In: *Nature Methods* 15.12 (Dec. 2018), pp. 1021–1028. ISSN: 1548-7105. DOI: 10.1038/s41592-018-0222-9.
 - [50] A. Keloth et al. "Single Cell Isolation Using Optical Tweezers". In: *Micromachines* 9.9 (Aug. 29, 2018), p. 434. ISSN: 2072-666X. DOI: 10.3390/mi9090434.
 - [51] M. Castellarnau et al. "Dielectrophoresis as a Tool to Characterize and Differentiate Isogenic Mutants of *Escherichia coli*". In: *Biophysical Journal* 91.10 (Nov. 15, 2006), pp. 3937–3945. ISSN: 0006-3495. DOI: 10.1529/biophysj.106.088534.
 - [52] J. P. Beech et al. "Active Posts in Deterministic Lateral Displacement Devices". In: *Advanced Materials Technologies* 4.9 (2019), p. 1900339. ISSN: 2365-709X. DOI: 10.1002/admt.201900339.
 - [53] V. Nerguizian et al. "The effect of dielectrophoresis on living cells: crossover frequencies and deregulation in gene expression". In: *Analyst* 144.12 (2019), pp. 3853–3860. ISSN: 0003-2654. DOI: 10.1039/C9AN00320G.
 - [54] D. Lee et al. "The potential of a dielectrophoresis activated cell sorter (DACS) as a next generation cell sorter". In: *Micro and Nano Systems Letters* 4.1 (May 20, 2016), p. 2. ISSN: 2213-9621. DOI: 10.1186/s40486-016-0028-4.
 - [55] A. Y. L. Jiang et al. "High-throughput continuous dielectrophoretic separation of neural stem cells". In: *Biomicrofluidics* 13.6 (Nov. 1, 2019). Publisher: American Institute of Physics, p. 064111. DOI: 10.1063/1.5128797.
 - [56] B. J. Sanghavi et al. "Ultrafast immunoassays by coupling dielectrophoretic biomarker enrichment in nanoslit channel with electrochemical detection on graphene". In: *Lab on a Chip* 15.24 (Nov. 2015), pp. 4563–4570. ISSN: 1473-0189. DOI: 10.1039/C5LC00840A.
 - [57] D. Holmes et al. "Bead-based immunoassays using a micro-chip flow cytometer". In: *Lab on a Chip* 7.8 (2007), pp. 1048–1056. DOI: 10.1039/B707507N.
 - [58] E. Iswardy et al. "A bead-based immunofluorescence-assay on a microfluidic dielectrophoresis platform for rapid dengue virus detection". In: *Biosens Bioelectron* 95 (BioMed. Res. Int. 2014 2017), pp. 174–180. ISSN: 0956-5663. DOI: 10.1016/j.bios.2017.04.011.
 - [59] H. Kim et al. "Hydrodynamic trap-and-release of single particles using dual-function elastomeric valves: design, fabrication, and characterization". In: *Microfluid Nanofluid* 13.5 (2012), pp. 835–844. ISSN: 1613-4982. DOI: 10.1007/s10404-012-1006-7.
 - [60] T. Yeo et al. "Microfluidic enrichment for the single cell analysis of circulating tumor cells". In: *Sci Reports* 6.1 (2016), srep22076. ISSN: 2045-2322. DOI: 10.1038/srep22076.

Bibliography

- [61] B. Dura et al. “Profiling lymphocyte interactions at the single-cell level by microfluidic cell pairing”. In: *Nat Commun* 6.1 (2015), p. 5940. ISSN: 2041-1723. DOI: 10.1038/ncomms6940.
- [62] X. Xu et al. “Finite element simulations of hydrodynamic trapping in microfluidic particle-trap array systems”. In: *Biomicrofluidics* 7.5 (Sept. 2013), p. 054108. ISSN: 1932-1058. DOI: 10.1063/1.4822030.
- [63] O. Français et al. “Electrical analogies applied on a volumetric micropump “highlighting of its fluidic resonant frequency””. In: (), p. 7.
- [64] R. J. Kimmerling et al. “A microfluidic platform enabling single-cell RNA-seq of multi-generational lineages.” In: *Nat Commun* 7.1 (2016), p. 10220. ISSN: 2041-1723. DOI: 10.1038/ncomms10220.
- [65] W.-H. Tan et al. “Dynamic microarray system with gentle retrieval mechanism for cell-encapsulating hydrogel beads.” In: *Lab Chip* 8.2 (2007), pp. 259–66. ISSN: 1473-0197. DOI: 10.1039/B714573J.
- [66] H. Kim et al. “Integration of a microfluidic chip with a size-based cell bandpass filter for reliable isolation of single cells.” In: *Lab Chip* 15.21 (2015), pp. 4128–32. ISSN: 1473-0197. DOI: 10.1039/C5LC00904A.
- [67] M.-H. Héctor et al. “Simultaneous concentration and separation of microorganisms: insulator-based dielectrophoretic approach”. In: *Anal Bioanal Chem* 396.5 (2010), pp. 1805–1816. ISSN: 1618-2642. DOI: 10.1007/s00216-009-3422-4.
- [68] Z. Zhu et al. “Microfluidic single-cell cultivation chip with controllable immobilization and selective release of yeast cells”. In: *Lab Chip* 12.5 (2011), pp. 906–915. ISSN: 1473-0197. DOI: 10.1039/C2LC20911J.
- [69] Q. Luan et al. “Microfluidic systems for hydrodynamic trapping of cells and clusters”. In: *Biomicrofluidics* 14.3 (May 1, 2020). Publisher: American Institute of Physics, p. 031502. DOI: 10.1063/5.0002866.
- [70] T. R. Mercer et al. “Testing at scale during the COVID-19 pandemic”. In: *Nature Reviews Genetics* 22.7 (July 2021), pp. 415–426. ISSN: 1471-0064. DOI: 10.1038/s41576-021-00360-w.
- [71] O. Vandenberg et al. “Considerations for diagnostic COVID-19 tests”. In: *Nature Reviews Microbiology* 19.3 (Mar. 2021), pp. 171–183. ISSN: 1740-1534. DOI: 10.1038/s41579-020-00461-z.
- [72] T. Nguyen et al. “2019 Novel Coronavirus Disease (COVID-19): Paving the Road for Rapid Detection and Point-of-Care Diagnostics”. In: *Micromachines* 11.3 (Mar. 2020). Number: 3 Publisher: Multidisciplinary Digital Publishing Institute, p. 306. DOI: 10.3390/mi11030306.
- [73] T. Xu et al. “Flexible combination of multiple diagnostic biomarkers to improve diagnostic accuracy”. In: *BMC Medical Research Methodology* 15.1 (Oct. 31, 2015), p. 94. ISSN: 1471-2288. DOI: 10.1186/s12874-015-0085-z.

- [74] R. Mayeux. "Biomarkers: Potential Uses and Limitations". In: *NeuroRx* 1.2 (Apr. 2004), pp. 182–188. ISSN: 1545-5343.
- [75] F. Eduati et al. "A microfluidics platform for combinatorial drug screening on cancer biopsies". In: *Nature Communications* 9.1 (June 22, 2018), p. 2434. ISSN: 2041-1723. DOI: 10.1038/s41467-018-04919-w.
- [76] D. Liu et al. "Applications and advances of metabolite biosensors for metabolic engineering". In: *Metabolic Engineering* 31 (Sept. 1, 2015), pp. 35–43. ISSN: 1096-7176. DOI: 10.1016/j.ymben.2015.06.008.
- [77] L. J. Blecka et al. "Immunoassays in therapeutic drug monitoring". In: *Clinics in Laboratory Medicine* 7.2 (June 1987), pp. 357–370. ISSN: 0272-2712.
- [78] R. Karlsson. "SPR for molecular interaction analysis: a review of emerging application areas". In: *Journal of molecular recognition: JMR* 17.3 (June 2004), pp. 151–161. ISSN: 0952-3499. DOI: 10.1002/jmr.660.
- [79] M. L. Y. Sin et al. "Advances and challenges in biosensor-based diagnosis of infectious diseases". In: *Expert Review of Molecular Diagnostics* 14.2 (Mar. 2014), pp. 225–244. ISSN: 1744-8352. DOI: 10.1586/14737159.2014.888313.
- [80] J. Burstein et al. "Urine pregnancy tests from antiquity to the present". In: *Early Pregnancy: Biology and Medicine: The Official Journal of the Society for the Investigation of Early Pregnancy* 1.4 (Dec. 1995), pp. 288–296. ISSN: 1354-4195.
- [81] B. D. Grant et al. "A SARS-CoV-2 Coronavirus Nucleocapsid Protein Antigen-Detecting Lateral Flow Assay". In: (Aug. 13, 2020). DOI: 10.26434/chemrxiv.12794825.v1.
- [82] K. L. Cox et al. "Immunoassay Methods". In: *Assay Guidance Manual*. Ed. by S. Markosian et al. Bethesda (MD): Eli Lilly & Company and the National Center for Advancing Translational Sciences, 2004.
- [83] E. G. Rey et al. "Mitigating the Hook Effect in Lateral Flow Sandwich Immunoassays Using Real-Time Reaction Kinetics." In: (2017), pp. 5095–5100. ISSN: 0003-2700. DOI: 10.1021/acs.analchem.7b00638.
- [84] M. A. MacMullan et al. "ELISA detection of SARS-CoV-2 antibodies in saliva". In: *Scientific Reports* 10.1 (Nov. 30, 2020), p. 20818. ISSN: 2045-2322. DOI: 10.1038/s41598-020-77555-4.
- [85] C. Lim et al. "Bead-based microfluidic immunoassays: The next generation". In: *Biosens Bioelectron* 22.7 (2007), pp. 1197–1204. ISSN: 0956-5663. DOI: 10.1016/j.bios.2006.06.005.
- [86] E. Verpoorte. "Beads and chips: new recipes for analysis". In: *Lab on a Chip* 3.4 (Nov. 2003), 60N–68N. ISSN: 1473-0197. DOI: 10.1039/b313217j.
- [87] D. Falconnet et al. "Rapid, Sensitive and Real-Time Multiplexing Platform for the Analysis of Protein and Nucleic-Acid Biomarkers". In: *Analytical Chemistry* 87.3 (Feb. 2015), pp. 1582–1589. ISSN: 0003-2700. DOI: 10.1021/ac502741c.

Bibliography

- [88] J. Ramón-Azcón et al. "Detection of pesticide residues using an immunodevice based on negative dielectrophoresis". In: *Biosensors and Bioelectronics* 24.6 (Feb. 2009), pp. 1592–1597. ISSN: 0956-5663. DOI: 10.1016/j.bios.2008.08.035.
- [89] C. Ruffert. "Magnetic Bead—Magic Bullet". In: *Micromachines* 7.2 (Jan. 28, 2016), p. 21. ISSN: 2072-666X. DOI: 10.3390/mi7020021.
- [90] X. Cui et al. "A fluorescent microbead-based microfluidic immunoassay chip for immune cell cytokine secretion quantification". In: *Lab on a Chip* 18.3 (Jan. 30, 2018). Publisher: The Royal Society of Chemistry, pp. 522–531. ISSN: 1473-0189. DOI: 10.1039/C7LC01183K.
- [91] X. Yu et al. "µFBI: A Microfluidic Bead-Based Immunoassay for Multiplexed Detection of Proteins from a µL Sample Volume". In: *PLOS ONE* 5.10 (Oct. 1, 2010). Publisher: Public Library of Science, e13125. ISSN: 1932-6203. DOI: 10.1371/journal.pone.0013125.
- [92] S. Nayak et al. "Point-of-Care Diagnostics: Recent Developments in a Connected Age". In: *Analytical chemistry* 89.1 (Jan. 3, 2017), pp. 102–123. ISSN: 0003-2700. DOI: 10.1021/acs.analchem.6b04630.
- [93] S. K. Vashist. "Point-of-Care Diagnostics: Recent Advances and Trends". In: *Biosensors* 7.4 (Dec. 18, 2017), p. 62. ISSN: 2079-6374. DOI: 10.3390/bios7040062.
- [94] V. Stadlbauer et al. "Comparison of 3 different multianalyte point-of-care devices during clinical routine on a medical intensive care unit". In: *Journal of Critical Care* 26.4 (Aug. 2011), 433.e1–11. ISSN: 1557-8615. DOI: 10.1016/j.jcrc.2010.09.003.
- [95] D. Harpaz et al. "Point-of-Care-Testing in Acute Stroke Management: An Unmet Need Ripe for Technological Harvest". In: *Biosensors* 7.3 (Aug. 3, 2017), p. 30. ISSN: 2079-6374. DOI: 10.3390/bios7030030.
- [96] L. Putallaz et al. "Nanofluidics Drives Point-of-care Technology for on the Spot Protein Marker Analysis with Rapid Actionable Results". In: *J Nanomed Nanotechnol* 10.5 (2019). DOI: 10.35248/2157-7439.19.10.536.
- [97] M. L. Everitt et al. "A critical review of point-of-care diagnostic technologies to combat viral pandemics". In: *Analytica Chimica Acta* 1146 (Feb. 15, 2021), pp. 184–199. ISSN: 0003-2670. DOI: 10.1016/j.aca.2020.10.009.
- [98] K. Makris et al. "Acute Kidney Injury: Definition, Pathophysiology and Clinical Phenotypes". In: *The Clinical Biochemist Reviews* 37.2 (May 2016), pp. 85–98. ISSN: 0159-8090.
- [99] E. A. J. Hoste et al. "Global epidemiology and outcomes of acute kidney injury". In: *Nature Reviews Nephrology* 14.10 (Oct. 2018), pp. 607–625. ISSN: 1759-507X. DOI: 10.1038/s41581-018-0052-0.
- [100] M. K. Nadim et al. "COVID-19-associated acute kidney injury: consensus report of the 25th Acute Disease Quality Initiative (ADQI) Workgroup". In: *Nature Reviews Nephrology* 16.12 (Dec. 2020), pp. 747–764. ISSN: 1759-507X. DOI: 10.1038/s41581-020-00356-5.
- [101] M. Rahman et al. "Acute kidney injury: a guide to diagnosis and management". In: *American Family Physician* 86.7 (Oct. 2012), pp. 631–639. ISSN: 1532-0650.

- [102] P. Maggi et al. "Novel antiretroviral drugs and renal function monitoring of HIV patients". In: *AIDS reviews* 16.3 (Sept. 2014), pp. 144–151. ISSN: 1698-6997.
- [103] F. P. Wilson et al. "Acute Kidney Injury in Real Time: Prediction, Alerts, and Clinical Decision Support". In: *Nephron* 140.2 (2018), pp. 116–119. ISSN: 2235-3186. DOI: 10.1159/000492064.
- [104] M. Ostermann et al. "Acute kidney injury 2016: diagnosis and diagnostic workup". In: *Critical Care* 20.1 (Sept. 2016), p. 299. ISSN: 1364-8535. DOI: 10.1186/s13054-016-1478-z.
- [105] M. S. N. Murty et al. "Serum cystatin C as a marker of renal function in detection of early acute kidney injury". In: *Indian Journal of Nephrology* 23.3 (May 2013), pp. 180–183. ISSN: 0971-4065. DOI: 10.4103/0971-4065.111840.
- [106] Z Yong et al. "Predictive value of serum cystatin C for acute kidney injury in adults: a meta-analysis of prospective cohort trials". In: *Scientific reports* (2017).
- [107] M. Padhy et al. "Serum neutrophil gelatinase associated lipocalin (NGAL) and cystatin C as early predictors of contrast-induced acute kidney injury in patients undergoing percutaneous coronary intervention". In: *Clinica Chimica Acta; International Journal of Clinical Chemistry* 435 (Aug. 2014), pp. 48–52. ISSN: 1873-3492. DOI: 10.1016/j.cca.2014.04.016.
- [108] S. Khawaja et al. "The utility of neutrophil gelatinase-associated Lipocalin (NGAL) as a marker of acute kidney injury (AKI) in critically ill patients". In: (2019), p. 4. ISSN: 2050-7771. DOI: 10.1186/s40364-019-0155-1.
- [109] P. Devarajan. "Neutrophil gelatinase-associated lipocalin (NGAL)". In: *Scandinavian journal of clinical and laboratory investigation. Supplementum* 241 (2008), pp. 89–94. ISSN: 0085-591X. DOI: 10.1080/00365510802150158.
- [110] S. Park et al. "Combining dielectrophoresis and concentration polarization-based preconcentration to enhance bead-based immunoassay sensitivity". In: *Nanoscale* (2019). ISSN: 2040-3364. DOI: 10.1039/C9NR02506E.
- [111] T. P. Taylor et al. "Overcoming the Effects of Matrix Interference in the Measurement of Urine Protein Analytes". In: *Biomarker Insights* 7 (Feb. 2012), pp. 1–8. ISSN: 1177-2719. DOI: 10.4137/BMI.S8703.
- [112] C. P. Price. "Point of care testing". In: *BMJ : British Medical Journal* 322.7297 (May 2001), pp. 1285–1288. ISSN: 0959-8138.
- [113] K. İçöz et al. "Detection of Proteins Using Nano Magnetic Particle Accumulation-Based Signal Amplification". In: *Applied Sciences* 6.12 (Dec. 2016), p. 394. DOI: 10.3390/app6120394.
- [114] U. M. Jalal et al. "On-chip signal amplification of magnetic bead-based immunoassay by aviating magnetic bead chains". In: *Bioelectrochemistry* 122 (Aug. 2018), pp. 221–226. ISSN: 1567-5394. DOI: 10.1016/j.bioelechem.2017.11.001.

Bibliography

- [115] H. Yoo et al. “Magnetically-focusing biochip structures for high-speed active biosensing with improved selectivity”. In: *Nanotechnology* 29.26 (May 2018), p. 265501. ISSN: 0957-4484. DOI: 10.1088/1361-6528/aabc4d.
- [116] W. U. Dittmer et al. “Sensitive and rapid immunoassay for parathyroid hormone using magnetic particle labels and magnetic actuation”. In: *Journal of Immunological Methods* 338.1 (Sept. 2008), pp. 40–46. ISSN: 0022-1759. DOI: 10.1016/j.jim.2008.07.001.
- [117] K. R. Sreenivasan. “Turbulent mixing: A perspective”. In: *Proceedings of the National Academy of Sciences* 116.37 (Sept. 2019), pp. 18175–18183. ISSN: 0027-8424, 1091-6490. DOI: 10.1073/pnas.1800463115.
- [118] M. Zimmermann et al. “Modeling and Optimization of High-Sensitivity, Low-Volume Microfluidic-Based Surface Immunoassays”. In: *Biomedical Microdevices* 7.2 (June 2005), pp. 99–110. ISSN: 1572-8781. DOI: 10.1007/s10544-005-1587-y.
- [119] J. Min et al. “Integrated Biosensor for Rapid and Point-Of-Care Sepsis Diagnosis”. In: *ACS nano* 12.4 (Apr. 2018), pp. 3378–3384. ISSN: 1936-0851. DOI: 10.1021/acsnano.7b08965.
- [120] C.-C. Hang et al. “Evaluation of serum neutrophil gelatinase-associated lipocalin in predicting acute kidney injury in critically ill patients”. In: *The Journal of International Medical Research* 45.3 (June 2017), pp. 1231–1244. ISSN: 0300-0605. DOI: 10.1177/0300060517709199.
- [121] P. Villa et al. “Serum cystatin C concentration as a marker of acute renal dysfunction in critically ill patients.” In: *Critical Care Lond Engl* 9.2 (2005), R139–43. ISSN: 1364-8535. DOI: 10.1186/cc3044.
- [122] A. A. Ellington et al. “Antibody-Based Protein Multiplex Platforms: Technical and Operational Challenges”. In: *Clinical chemistry* 56.2 (Feb. 2010), pp. 186–193. ISSN: 0009-9147. DOI: 10.1373/clinchem.2009.127514.
- [123] S. F. Kingsmore. “Multiplexed protein measurement: technologies and applications of protein and antibody arrays”. In: *Nature reviews. Drug discovery* 5.4 (Apr. 2006), pp. 310–320. ISSN: 1474-1776. DOI: 10.1038/nrd2006.
- [124] B. Harink et al. “An open-source software analysis package for Microspheres with Ratio-metric Barcode Lanthanide Encoding (MRBLEs)”. In: *PloS One* 14.3 (2019), e0203725. ISSN: 1932-6203. DOI: 10.1371/journal.pone.0203725.
- [125] C. Aira et al. “Bead-Based Multiplex Assay for the Simultaneous Detection of Antibodies to African Swine Fever Virus and Classical Swine Fever Virus”. In: *Frontiers in Veterinary Science* 6 (2019). ISSN: 2297-1769. DOI: 10.3389/fvets.2019.00306.
- [126] E. Savvateeva et al. “Multiple biomarker approach for the diagnosis and therapy of rheumatoid arthritis”. In: *Critical Reviews in Clinical Laboratory Sciences* 58.1 (Jan. 2021), pp. 17–28. ISSN: 1549-781X. DOI: 10.1080/10408363.2020.1775545.

- [127] T. Muinao et al. "Multi-biomarker panel signature as the key to diagnosis of ovarian cancer". In: *Heliyon* 5.12 (Dec. 1, 2019), e02826. ISSN: 2405-8440. DOI: 10.1016/j.heliyon.2019.e02826.
- [128] P. Yager et al. "Microfluidic diagnostic technologies for global public health". In: *Nature* 442.7101 (July 2006), pp. 412–418. ISSN: 1476-4687. DOI: 10.1038/nature05064.
- [129] N. Moore et al. "A Microfluidic Device to Enhance Viral Transduction Efficiency During Manufacture of Engineered Cellular Therapies". In: *Scientific Reports* 9.1 (Oct. 22, 2019), p. 15101. ISSN: 2045-2322. DOI: 10.1038/s41598-019-50981-9.
- [130] D. Migliozi et al. "Microfluidics-assisted multiplexed biomarker detection for in situ mapping of immune cells in tumor sections". In: *Microsystems & Nanoengineering* 5.1 (Nov. 6, 2019), pp. 1–12. ISSN: 2055-7434. DOI: 10.1038/s41378-019-0104-z.
- [131] F. Volpetti et al. "A Microfluidic Platform for High-Throughput Multiplexed Protein Quantitation". In: *PLOS ONE* 10.2 (Feb. 13, 2015). Publisher: Public Library of Science, e0117744. ISSN: 1932-6203. DOI: 10.1371/journal.pone.0117744.
- [132] L. Chang et al. "Immuno-PCR: An ultrasensitive immunoassay for biomolecular detection". In: *Analytica Chimica Acta* 910 (Mar. 3, 2016), pp. 12–24. ISSN: 0003-2670. DOI: 10.1016/j.aca.2015.12.039.
- [133] T. Sano et al. "Immuno-PCR: very sensitive antigen detection by means of specific antibody-DNA conjugates". In: *Science (New York, N.Y.)* 258.5079 (Oct. 2, 1992), pp. 120–122. ISSN: 0036-8075. DOI: 10.1126/science.1439758.
- [134] C. M. Niemeyer et al. "Combination of DNA-directed immobilization and immuno-PCR: very sensitive antigen detection by means of self-assembled DNA–protein conjugates". In: *Nucleic Acids Research* 31.16 (Aug. 15, 2003), e90. ISSN: 0305-1048.
- [135] J. M. Barletta et al. "Lowering the detection limits of HIV-1 viral load using real-time immuno-PCR for HIV-1 p24 antigen". In: *American Journal of Clinical Pathology* 122.1 (July 2004), pp. 20–27. ISSN: 0002-9173. DOI: 10.1309/529T-2WDN-EB6X-8VUN.
- [136] S.-H. Huang et al. "Detection of Staphylococcus aureus by a Sensitive Immuno-PCR Assay". In: *Clinical Chemistry* 50.9 (Sept. 1, 2004), pp. 1673–1674. ISSN: 0009-9147. DOI: 10.1373/clinchem.2004.033548.
- [137] J. A. G. L. van Buggenum et al. "A covalent and cleavable antibody-DNA conjugation strategy for sensitive protein detection via immuno-PCR". In: *Scientific Reports* 6.1 (Mar. 7, 2016), p. 22675. ISSN: 2045-2322. DOI: 10.1038/srep22675.
- [138] S. S. Agasti et al. "Photocleavable DNA Barcode–Antibody Conjugates Allow Sensitive and Multiplexed Protein Analysis in Single Cells". In: *Journal of the American Chemical Society* 134.45 (Nov. 14, 2012). Publisher: American Chemical Society, pp. 18499–18502. ISSN: 0002-7863. DOI: 10.1021/ja307689w.

Bibliography

- [139] B. M. Zeglis et al. "Enzyme-Mediated Methodology for the Site-Specific Radiolabeling of Antibodies Based on Catalyst-Free Click Chemistry". In: *Bioconjugate Chemistry* 24.6 (June 19, 2013). Publisher: American Chemical Society, pp. 1057–1067. ISSN: 1043-1802. DOI: 10.1021/bc400122c.
- [140] H. T. Le et al. "Antibody functionalization with a dual reactive hydrazide/click crosslinker". In: *Analytical Biochemistry* 435.1 (Apr. 1, 2013), pp. 68–73. ISSN: 1096-0309. DOI: 10.1016/j.ab.2012.12.018.
- [141] L. Garibyan et al. "Research Techniques Made Simple: Polymerase Chain Reaction (PCR)". In: *The Journal of investigative dermatology* 133.3 (Mar. 2013), e6. ISSN: 0022-202X. DOI: 10.1038/jid.2013.1.
- [142] F. S. Jones. "THE EFFECT OF HEAT ON ANTIBODIES". In: *The Journal of Experimental Medicine* 46.2 (July 31, 1927), pp. 291–301. ISSN: 0022-1007.
- [143] A. P. Demchenko. "Photobleaching of organic fluorophores: quantitative characterization, mechanisms, protection". In: *Methods and Applications in Fluorescence* 8.2 (Feb. 20, 2020), p. 022001. ISSN: 2050-6120. DOI: 10.1088/2050-6120/ab7365.
- [144] D. Axelrod et al. "Mobility measurement by analysis of fluorescence photobleaching recovery kinetics". In: *Biophysical Journal* 16.9 (Sept. 1976), pp. 1055–1069. ISSN: 0006-3495. DOI: 10.1016/S0006-3495(76)85755-4.
- [145] W. Engelen et al. "DNA-based control of protein activity". In: *Chemical Communications (Cambridge, England)* 52.18 (Mar. 4, 2016), pp. 3598–3610. ISSN: 1364-548X. DOI: 10.1039/c5cc09853j.
- [146] Y. Krishnan et al. "Nucleic acid based molecular devices". In: *Angewandte Chemie (International Ed. in English)* 50.14 (Mar. 28, 2011), pp. 3124–3156. ISSN: 1521-3773. DOI: 10.1002/anie.200907223.
- [147] J. Zhu et al. "Four-way junction-driven DNA strand displacement and its application in building majority logic circuit". In: *ACS nano* 7.11 (Nov. 26, 2013), pp. 10211–10217. ISSN: 1936-086X. DOI: 10.1021/nn4044854.
- [148] D. Y. Zhang et al. "Control of DNA Strand Displacement Kinetics Using Toehold Exchange". In: *Journal of the American Chemical Society* 131.47 (Dec. 2, 2009). Publisher: American Chemical Society, pp. 17303–17314. ISSN: 0002-7863. DOI: 10.1021/ja906987s.
- [149] G. P. Anderson et al. "Improved fluoroimmunoassays using the dye Alexa Fluor 647 with the RAPTOR, a fiber optic biosensor". In: *Journal of Immunological Methods* 271.1 (Dec. 20, 2002), pp. 17–24. ISSN: 0022-1759. DOI: 10.1016/S0022-1759(02)00327-7.
- [150] S. Halldorsson et al. "Advantages and challenges of microfluidic cell culture in polydimethylsiloxane devices". In: *Biosensors and Bioelectronics* 63 (Jan. 15, 2015), pp. 218–231. ISSN: 0956-5663. DOI: 10.1016/j.bios.2014.07.029.

- [151] B. Oskouei et al. "Evaluation of Mouse Oocyte In Vitro Maturation Developmental Competency in Dynamic Culture Systems by Design and Construction of A Lab on A Chip Device and Its Comparison with Conventional Culture System." In: 18.2 (2016), pp. 205–13. ISSN: 2228-5806.
- [152] C. Ma et al. "A clinical microchip for evaluation of single immune cells reveals high functional heterogeneity in phenotypically similar T cells." In: *Nat Med* 17.6 (2011), pp. 738–43. ISSN: 1078-8956. DOI: 10.1038/nm.2375.
- [153] S. Nagrath et al. "Isolation of rare circulating tumour cells in cancer patients by microchip technology". In: 450.7173 (2007), pp. 1235–1239. ISSN: 0028-0836. DOI: 10.1038/nature06385.
- [154] D. R. Gossett et al. "Hydrodynamic stretching of single cells for large population mechanical phenotyping". In: *Proc National Acad Sci* 109.20 (2012), pp. 7630–7635. ISSN: 0027-8424. DOI: 10.1073/pnas.1200107109.
- [155] L. A. Flanagan et al. "Unique Dielectric Properties Distinguish Stem Cells and Their Differentiated Progeny". In: *STEM CELLS* 26.3 (2008), pp. 656–665. ISSN: 1549-4918. DOI: 10.1634/stemcells.2007-0810.
- [156] L. Yang et al. "A multifunctional micro-fluidic system for dielectrophoretic concentration coupled with immuno-capture of low numbers of *Listeria monocytogenes*". In: *Lab on a Chip* 6.7 (June 27, 2006). Publisher: The Royal Society of Chemistry, pp. 896–905. ISSN: 1473-0189. DOI: 10.1039/B607061M.
- [157] S. A. Rosenberg et al. "Adoptive cell transfer as personalized immunotherapy for human cancer". In: *Science* 348.6230 (2015), pp. 62–68. ISSN: 0036-8075. DOI: 10.1126/science.aaa4967.
- [158] N. P. Restifo et al. "Adoptive immunotherapy for cancer: harnessing the T cell response". In: *Nat Rev Immunol* 12.4 (2012), p. 269. ISSN: 1474-1741. DOI: 10.1038/nri3191.
- [159] J. Lu et al. "Advancing practical usage of microtechnology: a study of the functional consequences of dielectrophoresis on neural stem cells." In: *Integr Biology Quantitative Biosci Nano Macro* 4.10 (2012), pp. 1223–36. ISSN: 1757-9694. DOI: 10.1039/C2IB20171B.
- [160] Y. Kashima et al. "Single-cell sequencing techniques from individual to multiomics analyses". In: *Experimental & Molecular Medicine* 52.9 (Sept. 2020), pp. 1419–1427. ISSN: 2092-6413. DOI: 10.1038/s12276-020-00499-2.
- [161] F. Tang et al. "mRNA-Seq whole-transcriptome analysis of a single cell". In: *Nature Methods* 6.5 (May 2009), pp. 377–382. ISSN: 1548-7105. DOI: 10.1038/nmeth.1315.
- [162] T. Stuart et al. "Integrative single-cell analysis". In: *Nature Reviews Genetics* 20.5 (May 2019), pp. 257–272. ISSN: 1471-0064. DOI: 10.1038/s41576-019-0093-7.
- [163] E. Z. Macosko et al. "Highly Parallel Genome-wide Expression Profiling of Individual Cells Using Nanoliter Droplets." In: *Cell* 161.5 (2015), pp. 1202–14. ISSN: 0092-8674. DOI: 10.1016/j.cell.2015.05.002.

Bibliography

- [164] R. Brignall et al. "Integration of Kinase and Calcium Signaling at the Level of Chromatin Underlies Inducible Gene Activation in T Cells". In: *J Immunol* 199.8 (2017), pp. 2652–2667. ISSN: 0022-1767. DOI: 10.4049/jimmunol.1602033.
- [165] S. Picelli et al. "Tn5 transposase and tagmentation procedures for massively scaled sequencing projects." In: *Genome Res* 24.12 (2014), pp. 2033–40. ISSN: 1088-9051. DOI: 10.1101/gr.177881.114.
- [166] M. Biočanin et al. "Simplified Drop-seq workflow with minimized bead loss using a bead capture and processing microfluidic chip". In: *Lab Chip* 19.9 (2019), pp. 1610–1620. ISSN: 1473-0197. DOI: 10.1039/C9LC00014C.
- [167] M. I. Love et al. "Moderated estimation of fold change and dispersion for RNA-seq data with DESeq2". In: *Genome Biol* 15.12 (2014), p. 550. DOI: 10.1186/s13059-014-0550-8.
- [168] M. Stephens et al. "The dielectrophoresis enrichment of CD34+ cells from peripheral blood stem cell harvests". In: *Bone Marrow Transplantation* 18.4 (Oct. 1996), pp. 777–782. ISSN: 0268-3369.
- [169] L. Altomare et al. "Levitation and movement of human tumor cells using a printed circuit board device based on software-controlled dielectrophoresis". In: *Biotechnology and Bioengineering* 82.4 (May 20, 2003), pp. 474–479. ISSN: 0006-3592. DOI: 10.1002/bit.10590.
- [170] F. F. Becker et al. "The removal of human leukaemia cells from blood using interdigitated microelectrodes". In: *Journal of Physics D Applied Physics* 27 (Dec. 1, 1994). ADS Bibcode: 1994JPhD...27.2659B, pp. 2659–2662. ISSN: 0022-3727. DOI: 10.1088/0022-3727/27/12/030.
- [171] A. Menachery et al. "Controlling cell destruction using dielectrophoretic forces". In: *IEEE Proceedings - Nanobiotechnology* 152.4 (Aug. 1, 2005). Publisher: IET Digital Library, pp. 145–149. ISSN: 1740-9748. DOI: 10.1049/ip-nbt:20050010.
- [172] X. Wang et al. "Role of peroxide in AC electrical field exposure effects on Friend murine erythroleukemia cells during dielectrophoretic manipulations". In: *Biochimica et biophysica acta* 1426.1 (Jan. 4, 1999), pp. 53–68. ISSN: 0006-3002.
- [173] L. Gervais et al. "Toward one-step point-of-care immunodiagnostics using capillary-driven microfluidics and PDMS substrates". In: *Lab Chip* 9.23 (2009), pp. 3330–3337. ISSN: 1473-0197. DOI: 10.1039/B906523G.
- [174] A. Olanrewaju et al. "Capillary microfluidics in microchannels: from microfluidic networks to capillare circuits". In: *Lab on a Chip* 18.16 (Aug. 7, 2018). Publisher: The Royal Society of Chemistry, pp. 2323–2347. ISSN: 1473-0189. DOI: 10.1039/C8LC00458G.
- [175] M. Zimmermann et al. "Capillary pumps for autonomous capillary systems". In: *Lab on a Chip* 7.1 (Dec. 19, 2006). Publisher: The Royal Society of Chemistry, pp. 119–125. ISSN: 1473-0189. DOI: 10.1039/B609813D.

- [176] A. K. Bivil et al. "A capillary flow-driven microfluidic system for microparticle-labeled immunoassays". In: *Analyst* 143.14 (July 9, 2018). Publisher: The Royal Society of Chemistry, pp. 3335–3342. ISSN: 1364-5528. DOI: 10.1039/C8AN00898A.
- [177] E. Eriksson et al. "Geometric Flow Control Lateral Flow Immunoassay Devices (GFC-LFIDs): A New Dimension to Enhance Analytical Performance". In: *Research* 2019 (June 17, 2019), p. 8079561. ISSN: 2639-5274. DOI: 10.34133/2019/8079561.
- [178] S. Sharma et al. "Point-of-Care Diagnostics in Low Resource Settings: Present Status and Future Role of Microfluidics". In: *Biosensors* 5.3 (Aug. 13, 2015), pp. 577–601. ISSN: 2079-6374. DOI: 10.3390/bios5030577.
- [179] N. R. Shanmugam et al. "Ultrasensitive and low-volume point-of-care diagnostics on flexible strips – a study with cardiac troponin biomarkers". In: *Scientific Reports* 6 (Sept. 16, 2016), p. 33423. ISSN: 2045-2322. DOI: 10.1038/srep33423.
- [180] D. E. McClure. "Clinical Pathology and Sample Collection in the Laboratory Rodent". In: *The Veterinary Clinics of North America. Exotic Animal Practice* 2.3 (Sept. 1999), pp. 565–590. ISSN: 1094-9194. DOI: 10.1016/S1094-9194(17)30111-1.
- [181] A. Serafin et al. "Blood volume and pain perception during finger prick capillary blood sampling: are all safety lancets equal?" In: *Postgraduate Medicine* 132.3 (Apr. 2020), pp. 288–295. ISSN: 1941-9260. DOI: 10.1080/00325481.2020.1717160.
- [182] D. Pacaud et al. "Assessment of Blood Volumes Obtained by Capillary Punctures in Older Children and Adolescents with Diabetes. † 558". In: *Pediatric Research* 39.4 (Apr. 1996), pp. 95–95. ISSN: 1530-0447. DOI: 10.1203/00006450-199604001-00579.
- [183] A. Adil et al. "Single-Cell Transcriptomics: Current Methods and Challenges in Data Acquisition and Analysis". In: *Frontiers in Neuroscience* 15 (2021), p. 398. ISSN: 1662-453X. DOI: 10.3389/fnins.2021.591122.
- [184] Z. Ma et al. "Fluorescence activated cell sorting via a focused traveling surface acoustic beam". In: *Lab on a Chip* 17.18 (Sept. 12, 2017). Publisher: The Royal Society of Chemistry, pp. 3176–3185. ISSN: 1473-0189. DOI: 10.1039/C7LC00678K.
- [185] M. J. Duffy. "Use of Biomarkers in Screening for Cancer". In: *Advances in Cancer Biomarkers: From biochemistry to clinic for a critical revision*. Ed. by R. Scatena. Advances in Experimental Medicine and Biology. Dordrecht: Springer Netherlands, 2015, pp. 27–39. ISBN: 978-94-017-7215-0. DOI: 10.1007/978-94-017-7215-0_3.
- [186] V. Blanda et al. "Galectin-3 in Cardiovascular Diseases". In: *International Journal of Molecular Sciences* 21.23 (Jan. 2020). Number: 23 Publisher: Multidisciplinary Digital Publishing Institute, p. 9232. DOI: 10.3390/ijms21239232.
- [187] S. Sciacchitano et al. "Galectin-3: One Molecule for an Alphabet of Diseases, from A to Z". In: *International Journal of Molecular Sciences* 19.2 (Feb. 2018). Number: 2 Publisher: Multidisciplinary Digital Publishing Institute, p. 379. DOI: 10.3390/ijms19020379.

Bibliography

- [188] S. P. Dudas et al. "Expression of human intestinal mucin is modulated by the -galactoside binding protein galectin-3 in colon cancer". In: *Gastroenterology* 123.3 (Sept. 1, 2002), pp. 817–826. ISSN: 0016-5085. DOI: 10.1053/gast.2002.35395.
- [189] I. Iurisci et al. "Concentrations of galectin-3 in the sera of normal controls and cancer patients". In: *Clinical Cancer Research: An Official Journal of the American Association for Cancer Research* 6.4 (Apr. 2000), pp. 1389–1393. ISSN: 1078-0432.
- [190] C. CĂINAP et al. "Classic tumor markers in gastric cancer. Current standards and limitations". In: *Clujul Medical* 88.2 (2015), pp. 111–115. ISSN: 1222-2119. DOI: 10.15386/cjmed-409.
- [191] L. Huang et al. "Aptamer-based lateral flow assay on-site biosensors". In: *Biosensors and Bioelectronics* 186 (Aug. 15, 2021), p. 113279. ISSN: 0956-5663. DOI: 10.1016/j.bios.2021.113279.
- [192] J. Chung et al. "Fast and continuous microorganism detection using aptamer-conjugated fluorescent nanoparticles on an optofluidic platform". In: *Biosensors and Bioelectronics*. Special Issue: BIOSENSORS 2014 67 (May 15, 2015), pp. 303–308. ISSN: 0956-5663. DOI: 10.1016/j.bios.2014.08.039.
- [193] S. Díaz-Amaya et al. "Aptamer-based SERS biosensor for whole cell analytical detection of E. coli O157:H7". In: *Analytica Chimica Acta* 1081 (Nov. 12, 2019), pp. 146–156. ISSN: 0003-2670. DOI: 10.1016/j.aca.2019.07.028.
- [194] H.-Y. Li et al. "Advances in detection of infectious agents by aptamer-based technologies". In: *Emerging Microbes & Infections* 9.1 (Dec. 2020), pp. 1671–1681. ISSN: 2222-1751. DOI: 10.1080/22221751.2020.1792352.
- [195] M. Jauset-Rubio et al. "Advances in aptamers-based lateral flow assays". In: *TrAC Trends in Analytical Chemistry* 97 (Dec. 1, 2017), pp. 385–398. ISSN: 0165-9936. DOI: 10.1016/j.trac.2017.10.010.
- [196] A. Chen et al. "Replacing antibodies with aptamers in lateral flow immunoassay". In: *Biosensors & Bioelectronics* 71 (Sept. 15, 2015), pp. 230–242. ISSN: 1873-4235. DOI: 10.1016/j.bios.2015.04.041.
- [197] J. M. Rothberg et al. "An integrated semiconductor device enabling non-optical genome sequencing". In: *Nature* 475.7356 (July 2011), pp. 348–352. ISSN: 1476-4687. DOI: 10.1038/nature10242.
- [198] Y. Gong et al. "Massively parallel detection of gene expression in single cells using sub-nanolitre wells". In: *Lab on a Chip* 10.18 (2010). Publisher: Royal Society of Chemistry, pp. 2334–2337. DOI: 10.1039/C004847J.
- [199] F. C. Jammes et al. "How single-cell immunology is benefiting from microfluidic technologies". In: *Microsystems & Nanoengineering* 6.1 (July 13, 2020), pp. 1–14. ISSN: 2055-7434. DOI: 10.1038/s41378-020-0140-8.
- [200] A. M. Skelley et al. "Microfluidic Control of Cell Pairing and Fusion". In: *Nature methods* 6.2 (Feb. 2009), pp. 147–152. ISSN: 1548-7091. DOI: 10.1038/nmeth.1290.

PIERRE-EMMANUEL THIRIET

Micro and Nanotechnologies Engineer, specialized in Life Sciences

@ pierre-emmanuel.thiriet@epfl.ch

Lausanne, Switzerland

in <https://www.linkedin.com/in/pierre-emmanuel-thiriet-55b569a6/>

EXPERIENCE

Doctoral assistant

CLSE lab, EPFL

June 2017 - Ongoing

Lausanne, Switzerland

Novel point of care diagnosis platform for acute kidney injury detection
Single cell analysis and retrieval for immunotherapy treatment
Master students supervision and teaching

Visiting researcher

Fordyce lab, University of Stanford

October 2021 - December 2021

Stanford, USA

Double-emulsion hydrogel microsphere for in-vitro protein production and interaction study

Master thesis

Maharbiz Group, University of California, Berkeley

September 2016 - March 2017

Berkeley, USA

Fast detection of patients experiencing sepsis through a novel lab-on-a-chip platform. Introduction of new tools for microfabrication to improve state of the art speed of detection

Engineering internship

Renault Group

June 2015 - August 2015

Guyancourt, France

Development of new pedestrian detection solutions for next generation of autonomous cars

EDUCATION

Master in Micro-engineering

EPFL

Sept 2015 - May 2017

Lausanne, Switzerland

Specialization in Micro- and Nano- Systems

Master of Science

Centrale-Supélec

Sept 2013 - Sept 2016

Gif-sur-Yvette, France

Specialization in Electrical Engineerings

French Classes Préparatoires

Lycée du Parc

Sept 2011 - Jun 2013

Lyon, France

2 year elite and intensive program in math, Physics and Chemistry

LANGUAGE SKILLS

English

French

German



TECHNICAL SKILLS

Programming languages

- Java
- Python
- Arduino
- LaTeX

CAD and Data processing software

- Comsol
- L-Edit
- Origin
- KiCad
- Matlab
- Excel

Microfabrication process

- Photolithography
- SU-8 process
- Metal deposition and lift-off
- Chromium mask fabrication
- Soft photolithography
- Scanning electron microscopy

Biology and diagnostics

- Cell culture
- Immunoassay design and characterization
- Lateral flow assay fabrication
- Clinical study design and implementation

PERSONAL SKILLS

Team work

Oral presentation

Written communication

Problem solving

INTERESTS

Hike

Tennis

Ski

Guitar

Mythology

Science-Fiction